Dielectric microcavities: Model systems for wave chaos and non-Hermitian physics

Hui Cao and Jan Wiersig

Rev. Mod. Phys. **87**, 61 — Published 22 January 2015

DOI: 10.1103/RevModPhys.87.61

Dielectric microcavities: model systems for wave chaos and non-Hermitian physics

Hui Cao

Department of Applied Physics,
Yale University,
New Haven,
CT 06520-8482,
USA

Jan Wiersig

Institut für Theoretische Physik,
Otto-von-Guericke-Universität Magdeburg,
Magdeburg,
Postfach 4120,
D-39016 Magdeburg,
Germany

(Dated: November 11, 2014)

Abstract

This is a review on theoretical and experimental studies on dielectric microcavities, which play a significant role in fundamental and applied research. The basic concepts and theories are introduced. Experimental techniques for fabrication of microcavities and optical characterization are described. Starting from undeformed cavities, the review moves on to weak deformation, intermediate deformation with mixed phase space, and then strong deformation with full ray chaos. Non-Hermitian physics such as avoided resonance crossings and exceptional points are covered along with various dynamical tunneling phenomena. Some specific topics like unidirectional output, beam shifts, wavelength scale microcavities, and rotating microcavities are discussed. The open microdisk and microsphere cavities are ideal model systems for the studies on wave chaos and non-Hermitian physics.

CONTENTS

I. INTRODUCTION

A. Motivation

Optical microcavities can greatly enhance light-matter interactions by storing optical energy in small volumes (Chang and Campillo, 1996; Vahala, 2004). The ability to concentrate light is important not only to fundamental physics studies, but also to practical device applications (Vahala, 2003). Instead of using metals which are usually lossy at optical frequencies, most microcavities are made of transparent dielectrics. In vertical cavities with distributed Bragg mirrors or photonic crystal defect cavities, optical confinement is achieved through constructive interference of multiply reflected or scattered light. An alternative scheme is total internal reflection from a dielectric interface, which occurs when light is incident from the higher refractive index (n_1) medium to the lower index (n_0) one with an angle $\chi \geq \arcsin(n_0/n_1)$. Consider a light beam propagating in a circular disk or a sphere via consecutive reflections from the boundary, the rotational symmetry of the cavity shape keeps the angle of incidence constant, and the condition for total internal reflection is maintained. The phase delay for light traveling one circle along the boundary must be equal to $2\pi m$ ($m = 1, 2, 3, ...$), so that the returning field has the same phase as the original field and a steady state is reached. Consequently, only light at certain frequencies can be confined in a cavity, and these frequencies are called cavity resonant frequencies ω_m. The corresponding electromagnetic modes are whispering gallery modes (WGMs), in analogy to the acoustic wave propagating along the smooth surface of a circular gallery (Rayleigh, 1945). They have also been referred to as "morphology-dependent resonances". The first observation of stimulated emission into optical WGMs was reported soon after the invention of laser in solid spheres of diameter 1-2 mm (Garrett *et al.*, 1961). Since then, WGMs have been studied in a range of micron-sized cavities, from liquid droplets and jets to solid spheres, cylinders, disks and rings. The optical confinement is, however, not perfect. Due to the curvature of the cavity boundary, light escapes out of the cavity via evanescent leakage, the optical analogue of quantum tunneling. In addition, the surface roughness introduces scattering loss, and there is residual absorption in the bulk material and at the surface. They all contribute to a finite lifetime τ of light in a WGM, which leads to a spectral width $\delta\omega = 1/\tau$. The quality factor is defined as $Q = \omega_m \tau$.

Compared to other microcavity resonances, the WGMs have extraordinarily high Q and small volume, which lead to diverse applications in linear and nonlinear optics as well as quantum optics. Ilchenko and Matsko (2006) reviewed the applications of dielectric whispering gallery resonators to optical devices such as filters, modulators, switches, sensors, lasers, frequency mixers as well as to microwave photonics. Next we will mention a few recent developments. The extremely long lifetime of light in a WGM makes it sensitive to the adsorption of a single molecule or virus onto the cavity surface (Vollmer and Arnold, 2008). Discrete changes in the resonance frequency have been observed due to the binding events of individual molecules or virons, allowing real-time label-free detection (Armani *et al.*, 2007; Vollmer *et al.*, 2008). A further enhancement of the sensitivity is realized using whispering-gallery microlasers (He *et al.*, 2011). The Purcell enhancement of optical density of states by the WGM dramatically increases light emission and scattering (Chang and Campillo, 1996; Vahala, 2004). Strong coupling of a single emitter (atom or quantum dot) to a WGM of a microdisk or a microtoroid has been achieved (Aoki *et al.*, 2006; Peter *et al.*, 2005; Srinivasan and Painter, 2006), facilitating the studies of cavity quantum electrodynamics. The strong buildup of intracavity optical field greatly enhances nonlinear coupling of light with matter (Chang and Campillo, 1996). For example, the Kerr-nonlinearity induced optical parametric oscillation in ultra-high-Q WGMs produces optical frequency combs with high repetition rate, permitting applications in astronomy, microwave photonics and telecommunications (see the review of Kippenberg *et al.* (2011) and refs therein). The whispering gallery resonators also play a crucial role in the emerging field of cavity optomechanics (Aspelmeyer *et al.*, 2013; Kippenberg and Vahala, 2008). As light is reflected from the cavity boundary, it exerts radiation pressure on the cavity wall, inducing a mechanical flex of the cavity structure. The intense circulating field of a WGM produces strong radiation pressure and excites vibrational resonances. An interesting example is the acoustic WGMs excited via stimulated Brillouin scattering of optical WGMs in a microsphere (Carmon and Vahala, 2007). The optomechanical coupling may lead to amplification or cooling of mechanical motion (Bahl *et al.*, 2012, 2011; Schliesser *et al.*, 2006).

Nearly perfect confinement of light also implies the difficulty of coupling light into or out of a WGM. Consequently whispering gallery microlasers do not provide adequate output power despite of low lasing threshold. Moreover, the rotational symmetry of a sphere or a circular disk leads to isotropic emission to free space, making it impossible to collect all the output. This is a serious problem for certain applications, e.g., single photon emitters. To increase the collection efficiency, a coupler such as a prism, a waveguide or a fiber is often placed in close proximity of the cavity to extract the evanescent field (Matsko and Ilchenko, 2006). High precision is required in positioning the coupler with respect to the cavity boundary in order to obtain sufficient output while avoiding a dramatic reduction of the quality factor (Q-spoiling). An alternative way of increasing the collection efficiency is to make the emission to free space directional by modifying the cavity boundary. Shortly after the first realization of semiconductor microdisk lasers, Levi *et al.* (1993) achieved directional output by introducing a tab or patterning a grating on the disk circumference. This kind of defects, however, also caused a serious Q-spoiling. To minimize this problem, Nöckel and Stone (1997) proposed smooth deformation of cavity shape to break the rotational symmetry and achieve anisotropic emission. They called such cavities "asymmetric resonant cavities". Even before their work, lasing in non-spherical liquid droplets was reported by Chang and coworkers (Qian *et al.*, 1986). The laser emission was confined to the liquid-air interface, confirming the surface nature of the lasing modes. Later, Gmachl *et al.* (1998) used semiconductor microcylinders with deformed cross section as laser resonators, and achieved high-power directional output. In the favorable directions of the far field, a power increase of up to three orders of magnitude over the conventional circularly symmetric lasers was obtained. Following these works, various shapes of deformed cavities were studied and fabricated (some examples are shown in Fig. 1), most of them either produce multi-directional output beams or have relatively low Q factor (Wiersig *et al.*, 2011b). The goal of combining unidirectional emission with high Q has been reached recently with a deformed microdisk whose boundary is described by the limaçon of Pascal (Shinohara *et al.*, 2009; Song *et al.*, 2009b; Wiersig and Hentschel, 2008; Yan *et al.*, 2009; Yi *et al.*, 2009). In addition, the reverse process, i.e., free space excitation of directional high Q modes in a deformed cavity, is made efficient with an appropriate choice of the pump beam direction and impact position. This has been utilized for nonresonant optical pumping of microcavity lasers (Lee *et al.*, 2007b; Yang *et al.*, 2008) and cryogenic cooling of optomechanical resonators (Park and Wang, 2009).

From the fundamental physics prospective, deformed microcavities have become a model system for the studies of nonlinear dynamics, quantum chaos, and non-Hermitian physics (Stone, 2001; Tureci *et al.*, 2005). For a classical chaotic system, the particle's trajectory depends with exponential sensitivity on the initial conditions. A common example is a two-dimensional (2D) billiard with reflecting walls and negligible friction, in which a point mass moves in a straight line until it hits the boundary and bounces back with the angle of reflection equal to the angle of incidence. Chaotic motion can be induced by proper shaping of the billiard, physicists and mathematicians have learned a great deal about chaotic motion and its onset by studying dynamical billiards with varied shape. If the billiard becomes very small and the point mass is a quantum particle, the dynamics is governed by quantum mechanics. The quantum billiard has been a focus of theoretical study on the quantum manifestation of classical chaos, but it is difficult to realize experimentally. For example, quantum dots were investigated as chaotic quantum systems, but the interactions of electrons complicate the dynamics. A breakthrough came in the 1990's when the microwave cavities were used as quantum billiards, with the recognition of the formal analogy between the wave properties of quantum particles and classical electromagnetism. The electromagnetic fields of the Maxwell's equations are the analog of the wavefunctions of the Schrödinger equation, thus quantum chaos can be studied in the context of wave chaos for electromagnetic fields. The "classical limit" corresponds to the limit of geometric optics where the wavelength is much smaller than the cavity size. Statistical analysis of the eigenfrequencies and eigenfunctions in 2D microwave cavities of varied shape illustrated the differences between classical chaotic and non-chaotic systems. Reviews on microwave billiards can be found in the book of H.-J. Stöckmann (Stöckmann, 2000) and the review of A. Richter (Richter, 1999). Interesting effects studied in quantum billiards are, for example, dynamical localization, and dynamical tunneling. Dynamical localization is the suppression of chaotic diffusion by destructive interference (Fishmann *et al.*, 1982; Frahm and Shepelyansky, 1997). Dynamical tunneling is a generalization of conventional tunneling which allows passage not only through an energy barrier but also through other kinds of dynamical barriers in phase space (Davis and Heller, 1981). While most microwave billiards are closed systems with reflecting boundaries, dielectric cavities have open boundaries through which waves may escape. The openness makes the effective Hamiltonian of the system non-Hermitian. This leads to various interesting phenomena such as an increase of the quality factor at avoided resonance crossings (Persson *et al.*, 2000), chirality of mode pairs (Wiersig *et al.*, 2008) and exceptional points (Heiss, 2000), which are branch point singularities of eigenvalues and eigenvectors of a non-Hermitian matrix. Therefore, deformed dielectric microcavities are ideal models for the fundamental studies of open chaotic systems (Nöckel and Stone, 1997) and non-Hermitian quantum physics (Lee *et al.*, 2009a).

B. Scope

We will review the experimental and theoretical studies of dielectric microcavities as open chaotic systems in the past two decades. There are previous short reviews on this topic (Harayama and Shinohara, 2011; Stone, 2001; Tureci *et al.*, 2005; Xiao *et al.*, 2010), which focus on either specific cavity shapes (e.g., quadrupolar deformation in (Stone, 2001; Tureci *et al.*, 2005)) or certain features (e.g., output directionality in (Xiao *et al.*, 2010)). Here we will cover a variety of cavity shapes, from smooth deformations of circle or sphere to polygons and cavities with boundary defects. We will explain how the shape of cavity boundary determines the intracavity ray dynamics and how light escapes out of the cavity. Depending on the type and degree of shape deformation, the intracavity ray dynamics can be regular, chaotic or partial chaotic. Correspondingly, there is a diversity of cavity modes with rich spatial structures, e.g., whispering gallery modes, chaotic modes, scar modes (localized on unstable periodic ray trajectories), etc. We will discuss how these modes are formed, and explore their characteristics such as quality factor and far-field pattern.

In this review we will not cover the nonlinear interactions of light with gain materials or the interactions of multiple lasing modes via the active media, which have been reviewed in (Harayama and Shinohara, 2011). Instead we will focus on linear wave optics and (nonlinear) ray optics in the following three regimes, (i) the "classical regime", $nkR > 10^3$ (n is the intracavity index of refraction, $k = 2\pi/\lambda$, λ is the vacuum wavelength), where the ray dynamics rules, (ii) the "semiclassical regime", $nkR \sim 10^2 - 10^3$, where wave corrections emerge, (ii) the "quantum regime", $nkR \sim 10 - 10^2$, where wave effects become dominant. We will explore the ray-wave correspondence, and emphasize the consequence of cavity openness, e.g., the nonorthogonality of cavity modes which leads to excess quantum noise. In addition to stationary cavities, we will review wave chaos in rotating microcavities, and explain how the rotation will affect the resonance frequency, quality factor and far-field pattern.

II. THEORETICAL MODEL AND EXPERIMENTAL TECHNIQUES

A. Mode equation and wave simulations

The aim of this subsection is to give the definition of electromagnetic (optical) modes in passive dielectric cavities, to introduce the corresponding mode equation with emphasis on the deformed disk and to review the numerical schemes to solve it.

The geometry of a dielectric cavity is determined by the spatial profile of the refractive index $n(\vec{r})$. For a given profile an electromagnetic mode is defined as a time-harmonic solution of Maxwell's equations with frequency ω, in the same way as a quantum mechanical energy eigenfunction is a solution of the Schrödinger equation with fixed eigenenergy. However, dielectric cavities are open systems as light leaks out of the cavity. Hence, a mode in a dielectric cavity is a quasi-bound state/quasi-normal mode (Gamow, 1928; Kapur and Peierls, 1938) decaying exponentially in time with lifetime τ. This can be conveniently expressed by a complex-valued frequency ω, where the imaginary part is related to the lifetime via $\tau = -1/2\mathrm{Im}(\omega)$ with $\mathrm{Im}(\omega) < 0$. The quality factor Q compares the lifetime τ with the oscillation period of the light $T = 2\pi/\mathrm{Re}(\omega)$,

$$Q = 2\pi\frac{\tau}{T} = -\frac{\mathrm{Re}(\omega)}{2\mathrm{Im}(\omega)} \ . \tag{1}$$

The quasi-bound states are connected to the peak structure in scattering spectra (see, e.g., (Landau, 1996)) as illustrated in Fig. 2.

To derive the mode equation one has to substitute the complex representation of time-harmonic electric field $\vec{E}(\vec{r},t) = \vec{E}(\vec{r})\exp(-i\omega t)$ and magnetic field $\vec{H}(\vec{r},t) = \vec{H}(\vec{r})\exp(-i\omega t)$ into Maxwell's equations for non-magnetic, dielectric materials in the absence of free charges and currents. As most dielectric cavities consists of one or several homogeneous regions the refractive index $n(\vec{r})$ is often a piece-wise constant function. In that case one arrives at

$$\left(\nabla^2 + n^2(\vec{r})\frac{\omega^2}{c^2}\right)\begin{pmatrix}\vec{E}(\vec{r})\\ \vec{H}(\vec{r})\end{pmatrix} = 0 \tag{2}$$

provided that $\vec{r}$ is not a boundary point. If $\vec{r}$ is on a boundary separating two regions 1 and

2 with constant refractive indices n_1 and n_2 the fields are subject to the continuity relations

$$\vec{\nu}(\vec{r}) \times [\vec{E}_1(\vec{r}) - \vec{E}_2(\vec{r})] = 0 \ , \tag{3}$$

$$\vec{\nu}(\vec{r}) \cdot [n_1^2\vec{E}_1(\vec{r}) - n_2^2\vec{E}_2(\vec{r})] = 0 \ , \tag{4}$$

$$\vec{\nu}(\vec{r}) \times [\vec{H}_1(\vec{r}) - \vec{H}_2(\vec{r})] = 0 \ , \tag{5}$$

$$\vec{\nu}(\vec{r}) \cdot [\vec{H}_1(\vec{r}) - \vec{H}_2(\vec{r})] = 0 \ , \tag{6}$$

where $\vec{\nu}(\vec{r})$ is the local normal vector. The appropriate boundary condition at infinity is the "outgoing wave" condition (Sommerfeld radiation condition). Together with this boundary condition, Eqs. (2)–(6) define the modes in a dielectric cavity.

In the case of a (deformed) disk cavity, the mode equation and the boundary conditions can be significantly simplified by replacing the disk by an infinite dielectric cylinder with an arbitrary cross-section. The translation symmetry along the z-axis of this idealized geometry allows the ansatz (Jackson, 1962; Tureci *et al.*, 2005)

$$\vec{E}(\vec{r}) = \vec{E}(x, y) \exp(ink_z z) \tag{7}$$

and analog for $\vec{H}$. The particular case of $k_z = 0$ corresponds to light propagation in the (x, y)-plane only. For this case the mode equation can be written as scalar Helmholtz equation

$$\left(\nabla^2 + n^2(x, y)\frac{\omega^2}{c^2}\right)\psi(x, y) = 0 \ , \tag{8}$$

with ∇ now restricted to the x and y coordinates. The complex-valued wave function ψ equals E_z in the case of transverse magnetic (TM) polarization ($H_z = 0$). For transverse electric (TE) polarization ($E_z = 0$) the wave function ψ equals H_z. The other electric and magnetic field components can be computed from E_z and H_z, respectively (Tureci *et al.*, 2005). Admissible solutions of the mode equation in Eq. (8) are those which remain finite everywhere inside the cavity. The continuity relations (3)-(6) in the (x, y)-plane simplify to

$$\psi_1 = \psi_2, \ \partial_\nu\psi_1 = \partial_\nu\psi_2 \quad \text{TM polarization} \tag{9}$$

$$\psi_1 = \psi_2, \ \frac{\partial_\nu\psi_1}{n_1^2} = \frac{\partial_\nu\psi_2}{n_2^2} \quad \text{TE polarization.} \tag{10}$$

∂_ν is the normal derivative defined as $\partial_\nu = \vec{\nu}(\vec{r}) \cdot \nabla$. Note the structural equivalence of mode equation (8) and the stationary Schrödinger equation of a quantum particle in a piece-wise constant potential. In polar coordinates (r, φ) the outgoing wave condition in two dimensions for large r can be written as

$$\psi \sim \psi_{\text{out}} = h(\varphi, k)\frac{\exp{(ikr)}}{\sqrt{r}} \ . \tag{11}$$

Due to this boundary condition the solution of the mode equation has to decay in time. It is therefore a quasi-bound state with complex-valued frequency ω; $\text{Im}(\omega) < 0$. Moreover, ψ diverges as $\exp{[-\text{Im}(k)r]}$ with $\text{Im}(k) = \text{Im}(\omega)/c < 0$ as the radial coordinate r tends to infinity. Hence, the quasi-bound state ψ is strictly speaking not normalizable. The divergence does not affect the angular distribution of the emitted light, $h(\varphi, k)$.

In practice a microdisk has a finite vertical extension which is usually taken into account within the *effective-index approximation*; see, e.g., (Smotrova *et al.*, 2005). The central assumption is that the separation ansatz (7) is still valid, ignoring a weak mixing of TM and TE polarizations. The resulting equation for the z-direction leads to a series of quantized values of k_z. Usually it is sufficient to consider the smallest one. Associated with this value of k_z is the mode equation (8) and the continuity relations (9) and (10) with n replaced by an effective index of refraction $n_{\text{eff}} = n\sqrt{1 - (k_z/k)^2}$ inside the cavity and $n_{\text{eff}} = 1$ outside the cavity.

The effective-index approximation cannot be justified rigorously and no error estimates can be given. However, many publications have confirmed that this approach works well in terms of eigenfrequencies for different kinds of planar geometries such as photonic crystals (Qiu, 2002), annular Bragg cavities (Scheuer *et al.*, 2005), and microdisks (Michael, 2009). Even microcavities supported by a pedestal are described in sufficient accuracy (Lozenko *et al.*, 2012). Moreover, the near-field pattern (Fang *et al.*, 2007; Redding *et al.*, 2012b) and far-field pattern (Schwefel *et al.*, 2004; Shinohara *et al.*, 2009) of deformed microdisks computed in the effective-index approximation agree with experimental data. The validity of the effective-index approximation for dielectric disks has been questioned recently by Bittner *et al.* (2009). However, the observed deviations of typically below 1 percent can be considered as being small having in mind that the bulk refractive index is often known with less accuracy.

As most problems in electrodynamics do not allow for an analytical treatment, much effort has been put in the development of numerical schemes. The most prominent one is the finite-difference time-domain (FDTD) method (Taflove and Hagness, 2000) which is perfectly suited to simulate the dynamics of light propagation in complex environments.

It can also be used to determine light confinement in dielectric cavities (Fang *et al.*, 2007, 2005b; Kim *et al.*, 2004; Srinivasan *et al.*, 2006), but for long-lived modes in the semiclassical regime (short-wavelength regime), i.e. when the wavelength is small compared to the characteristic length scales of the system, it requires immense computational power. In this case it is more convenient to work in the frequency domain. This is in particular advantageous if the frequency dependence of the refractive index has to be included. For the frequency domain several approaches can be applied to quasi-two-dimensional geometries, such as the finite-difference frequency-domain (FDFD) method (Shainline *et al.*, 2009), wave-matching method (Hentschel and Richter, 2002; Nöckel and Stone, 1995), internal scattering quantization approach (Tureci *et al.*, 2005), volume element methods (Martin *et al.*, 1999), boundary element methods (Wiersig, 2003a; Zou *et al.*, 2011) and related methods based on boundary integral equations (Boriskina *et al.*, 2004). The FDFD and the volume element methods are restricted to small structures because of the limited computational power that is available today. The wave-matching method based on the expansion of the wave function into a basis of Bessel and Hankel functions is more efficient and can be applied to large structures. However, usually the expansion is around a single point in position space (single pole method). In this case the method relies on the Rayleigh hypothesis which fails for strongly deformed disks (van den Berg and Fokkema, 1979). This same is true for the highly efficient internal scattering quantization approach. No such problem exists for the boundary element methods which are also efficient (Zou *et al.*, 2011), in particular in combination with the harmonic inversion technique (Wiersig and Main, 2008).

B. Ray model

The short-wavelength limit of wave optics is geometrical (ray) optics. In the semiclassical regime much understanding about the wave dynamics in dielectric cavities can be gained by studying the dynamics of rays inside the given structure. In the following we describe the basic ray model introduced by Mekis *et al.* (1995); Nöckel and Stone (1995, 1997); Nöckel *et al.* (1994, 1996) which is nowadays commonly used for dielectric cavities.

First, we address ray dynamics in a closed cavity with perfectly reflecting walls. This problem is mathematically equivalent to a classical particle moving freely along straight lines in a two-dimensional planar domain (billiard) with specular reflections at the boundary.

Figure 3(a) depicts the elementary aspects of the billiard dynamics. According to the law of reflection, the incident ray and the reflected ray make the same angle χ with respect to the inward normal vector $\vec{\nu}$ at the boundary point of the reflection. Clearly, only the shape of the boundary determines the dynamical properties of the billiard.

The real-space trajectories in a typical billiard can be very complicated, so it is more appropriate to study the trajectories in phase space. The phase space of a 2D billiard is four dimensional consisting of two spatial degrees of freedom and two conjugate momenta. However, due to conservation of the particle's energy, the motion actually takes place on a three-dimensional surface. A further reduction of dimensionality can be achieved by the Poincaré surface of section (SOS) (Lichtenberg and Lieberman, 1992). For billiards, it is a plot of the intersection points of a set of trajectories with the cavity's boundary. This is illustrated in Fig. 3. When a ray/particle is reflected at the cavity's boundary, its position in terms of the arclength coordinate along the boundary s and the quantity $p = \sin\chi$ are recorded. We follow here the convention that $\sin\chi > 0$ means counterclockwise rotation and $\sin\chi < 0$ means clockwise rotation; cf. Figs. 3(a) and (b). The quantity $p \in [-1, 1]$ can be interpreted as the tangential component of the normalized momentum with respect to the boundary curve at a given position $s \in [0, s_{\text{max}}]$. The coordinate s and its canonical conjugate momentum p are called Birkhoff coordinates. This pair is the natural set of coordinates since the mapping from bounce to bounce, $(s_i, p_i) \to (s_{i+1}, p_{i+1})$, is area-preserving (Birkhoff, 1927); see also (Berry, 1981).

In the special case of the circular billiard, the angle of incidence χ is not changed by the billiard mapping. Hence, rays are confined to two-dimensional surfaces of constant $\sin\chi$ and constant energy. The topology of such invariant surfaces is that of a two-dimensional torus (Arnol′d, 1978). In the SOS these tori are lines $\sin\chi = \text{constant}$. The dynamics on these lines can be periodic or quasi-periodic.

A more complicated example, the mushroom billiard, is shown in Fig. 4. This exotic class of geometries has attracted much attention because the phase space of such a system is sharply divided into regular and chaotic parts (Bunimovich, 2001). In a regular region, the dynamics is similar to the case of the circular billiard with χ being a constant of motion. In contrast, the dynamics in a chaotic region exhibit an exponential sensitivity on the initial conditions (Lichtenberg and Lieberman, 1992). Moreover, the dynamics is ergodic, i.e. a single trajectory eventually comes arbitrarily close to any point in the given chaotic region and as a result it covers a finite fraction of the SOS. The phase space of such a partially chaotic system is called “mixed phase space”. A mushroom-shaped optical microcavity has been studied in (Andreasen *et al.*, 2009).

In a generic billiard, the coexistence of regular and chaotic dynamics in the mixed phase space is much more involved. Regular regions (called “islands”) embedded in a chaotic region (which is usually referred to as “sea” to complete the analogy) are surrounded by a chain of smaller islands which in turn are surrounded by even smaller islands and so on, leading to an infinite hierarchy of islands. Figure 5 shows as an example for a generic case the SOS of a quadrupole billiard (Nöckel *et al.*, 1996; Tureci *et al.*, 2002) with boundary given in polar coordinates by

$$r(\varphi) = R(1 + \varepsilon \cos 2\varphi) \ . \tag{12}$$

The ray dynamics is solely determined by the deformation parameter $\varepsilon \geq 0$ and independent on the average radius R. Only trajectories with positive χ are shown in Fig. 5. The SOS is symmetric with respect to $\chi \to -\chi$ due to the time-reversal symmetry of the billiard system. It can be clearly seen that the ray dynamics can be regular or chaotic depending on the initial conditions. Figures 5(a)-(c) depict a quasi-periodic whispering-gallery ray, a periodic ray from the center of an island, and a chaotic ray.

A ray in a billiard system never leaves the interior of the domain enclosed by the boundary. In a dielectric cavity, however, a ray can leave the cavity via refractive escape. Figure 6 illustrates that the ray partially leaves the cavity when the angle of incidence χ is smaller than the critical angle χ_c for total internal reflection; $\sin \chi_c = 1/n$ assuming that air surrounds the cavity. Hence, a dielectric cavity can be considered as an “open billiard” (Nöckel and Stone, 1995, 1997).

In the SOS of such an open billiard the region between the “critical lines” $\sin \chi = \pm 1/n$ is called “leaky region”; see Fig. 7(a). The size of the leaky region increases with decreasing refractive index n. Chaotic systems with a leaky region in phase space have been given a lot of attention in recent years, for a review see (Altmann *et al.*, 2013). When a ray inside the dielectric cavity hits the leaky region then, in the crudest approximation, the ray is lost for the internal ray dynamics and the transmitted ray contributes to the far-field intensity pattern $f(\varphi)$ according to Snell’s law $n \sin \chi = \sin \eta$ (Jackson, 1962); cf. Fig. 6. A more sophisticated scheme is to account for the partial leakage in the leaky region by assigning an initial intensity I to a given ray. Whenever it hits the cavity's boundary the intensity is reduced according to

$$I_i \to I_{i+1} = R^{\mathrm{TM,TE}}(\sin\chi_i) I_i \tag{13}$$

where $R^{\mathrm{TM,TE}}(\sin\chi) \leq 1$ is the polarization-dependent reflection coefficient (Schwefel *et al.*, 2004). The simplest choice for $R^{\mathrm{TM,TE}}$ is according to Fresnel's laws for a planar dielectric interface (Jackson, 1962); see Fig. 7(b). Note that in the case of TE polarization the reflection coefficient goes down to zero at Brewster's angle.

Tracing a single ray is not sufficient for the computation of the far-field intensity pattern $f(\varphi)$. What is needed is a properly chosen ensemble of rays which establishes a link to the modes of the dielectric cavity. There is no general recipe for constructing these ensembles as it depends on the geometry of the cavity, so we postpone this issue to Sec. IV.

The reflection coefficient $R^{\mathrm{TM,TE}}$ can be used to incorporate tunneling into the ray model (Nöckel and Stone, 1997). Tunneling is the main decay channel of the (weakly deformed) circular cavity as refractive escape is forbidden due to conservation of the angle of incidence. In this case, the tunneling can be related to a modified reflection coefficient at curved dielectric interfaces (Hentschel and Schomerus, 2002). Other extensions of the ray model will be discussed in Sec. VIII.

Ray tracing has also been performed in deformed dielectric spheres. In the special case of an axisymmetric deformed sphere the conservation of angular momentum reduces this problem effectively to a two-dimensional billiard with centrifugal potential. Such a case has been studied by Nöckel and Stone (1995). Ray dynamics in a nonaxisymmetric deformed dielectric sphere has been analyzed in (Lacey and Wang, 2001). Here, the SOS is four-dimensional, therefore the ray trajectories have to be laboriously visualized and analyzed in a number of different projections.

C. Husimi functions

In this subsection we discuss a powerful tool for the comparison of ray and wave properties, the Husimi function for dielectric cavities. The Husimi function is one of the simplest quasi-probability distributions of a quantum state in phase space (Husimi, 1940). It is obtained from the overlap of the wave function with a coherent state that represents a minimal-uncertainty wave packet.

The Husimi function has been adapted to billiards by Crespi *et al.* (1993). It can be considered as a representation of the quantum state on the SOS at the boundary of the billiard. This approach has been applied also quite extensively to dielectric cavities even though the boundary conditions (9) and (10) are different. For TM boundary conditions (9) Hentschel *et al.* (2003) have derived Husimi functions by using a saddle point approximation valid in the semiclassical regime. In total four different Husimi functions have been obtained, two for incident and emerging waves inside the cavity and two for those outside the cavity. The Husimi functions for the internal waves have been widely used, so we focus on them in the following. The incident and the emerging Husimi functions are

$$H^{\mathrm{inc(em)}}(s,p) = \frac{nk}{2\pi}\left|\mathcal{F}h_{\psi}(s,p) - (+)\frac{i}{k\mathcal{F}}h_{\partial\psi}(s,p)\right|^2 \tag{14}$$

with weighting factor $\mathcal{F} = \sqrt{n\sqrt{1-p^2}}$. The function

$$h_g(s,p) = \int_0^{s_{\mathrm{max}}} ds'\, g(s')\xi(s';s,p) \tag{15}$$

is the overlap of the wave function ($g = \psi$) or its normal derivative ($g = \partial_\nu\psi$) on the cavity's boundary with the minimal-uncertainty wave packet

$$\xi(s';s,p) = (\sigma\pi)^{-\frac{1}{4}} \sum_{l=-\infty}^{\infty} \exp\Big[-\frac{(s'+s_{\mathrm{max}}l-s)^2}{2\sigma} \\ -inkp(s'+s_{\mathrm{max}}l)\Big]\,. \tag{16}$$

The wave packet $\xi(s';s,p)$ is centered around (s,p). The relative uncertainty in s and p can be controlled with the parameter σ.

Figure 8 shows as example the Husimi function of a mode in an annular cavity (a microdisk with an internal disk-shaped area of different refractive index; see, e.g., (Hentschel and Richter, 2002; Preu *et al.*, 2013; Schomerus *et al.*, 2004; Wiersig and Hentschel, 2006)) superimposed on the SOS of the outer boundary. It can be seen that the mode is localized in the chaotic region of phase space. The contribution in the leaky region determines the emission properties.

There is an independently developed approach to visualize the mode in the leaky region of the SOS, the so-called intensity flux distribution which is based on a coarse-grained Poynting vector (Shinohara and Harayama, 2007). It has been proven that the flux distribution coincides with the difference between the incident and the emerging Husimi function (Shinohara and Harayama, 2011).

D. Cavity fabrication

In this subsection, we introduce various types of dielectric microcavities, and describe briefly how they are fabricated. For more information, we refer the readers to several reviews (Chiasera *et al.*, 2010; He *et al.*, 2013; Ilchenko and Matsko, 2006; Righini *et al.*, 2011; Xiao *et al.*, 2010).

1. Liquid droplets and microjets

Liquid droplets are 3D microcavities formed by surface tension forces. In the early days they were generated by Berglund-Liu piezoelectric vibrating-orifice aerosol generators (Qian *et al.*, 1986). As shown in Fig. 9, right below the vibrating orifice is a periodically perturbed, continuously connected liquid cylinder, which develops to separate, highly distorted droplets that oscillate between prolate spheroids and oblate spheroids. Farther away, the stream transits to monodisperse, equally spaced spherical droplets. The radii of the droplets, which depend on the size of the orifice aperture, are typically a few tens of micron. Instead of flying in air, the droplets may also be suspended in liquids or placed on solid substrates (He *et al.*, 2013).

The total internal reflection of light at the liquid-air interface leads to the formation of WGMs in the droplet. Despite of low refractive index contrast (commonly used liquids have refractive index between 1.3 and 1.4), the droplet has very smooth surface, which minimizes the scattering loss. Light emitting or amplifying materials can be easily incorporated into the liquid droplets, e.g., by adding dye molecules or quantum dots to a solution before creating droplets. Lasing was realized in dye-doped liquid droplets with optical excitation of dye molecules (Tzeng *et al.*, 1984). Micro-sized liquid droplets were also used for cavity enhanced spectroscopy (Symes *et al.*, 2004). Liquid microjet can create a continuous and stationary column of liquid with a precise control of the hydrodynamics of the jet (see Fig. 1(b) in Sec. I). Light propagating perpendicular to the axis of the column may be trapped in one cross section by total internal reflection at the liquid-air interface. Thus the microjet was used in the study of 2D microcavities (Moon *et al.*, 1997). Moreover, the cavity size and shape can be varied continuously along the stream. By deforming the orifice aperture (Yang *et al.*, 2006) or applying a lateral gas flow (Moon *et al.*, 1997), the cross-section of the microjet column is distorted from circle. The exact surface profile may be deduced from the optical diffraction pattern (Moon *et al.*, 2008). The typical dimension of the cross section is a few tens of micron, and the surface roughness induced scattering is as weak as that in the droplets.

2. Solid microspheres and microtoroids

Solid microspheres have been produced from a large variety of materials, organic and inorganic, amorphous and crystalline. The widely used amorphous microspheres are fabricated with two techniques based on melting process and sol-gel chemistry. A detailed description of these techniques is given in the reviews of Chiasera *et al.* (2010) and Righini *et al.* (2011). As an example, we describe below a common and effective method of making a glass microsphere by melting the end of a glass fiber. The heating source can be an oxygen/butane torch, a high power CO_2 laser, or an electric arc as in a commercial fiber splicer. Upon heating the distal tip of a silica fiber, the glass reflows to form a spherical volume under the influence of surface tension. Due to high viscosity of silica, the reflowed structure becomes extremely uniform and highly spherical (eccentricities $< 3\%$). The sphere diameter varies from ten to a hundred micron, depending on the original diameter of the fiber tip. Smaller spheres are produced by first tapering the fiber to reduce the diameter of the tip. The silica microsphere remains attached to the fiber stem from which it was formed, making it easy to handle [Fig. 10(a)]. Typically one excites the WGMs that lie in the equatorial plane and have very small overlap with the stem, thus the effect of the stem on the WGMs is negligible. The surface roughness is extremely low, on the order of 1 nm, thus high quality factors can be reached for the WGMs.

Asymmetric microspheres [Fig. 1(c)] have also been fabricated by fusing two silica spheres together with a CO_2 laser beam (Lacey and Wang, 2001). Alternatively, a single spherical microsphere can be deformed by reheating with one or two laser beams incident on different sides (Xiao *et al.*, 2007, 2009). Microbottle resonators were made from optical fibers in a two-step heat-and-pull process by sequentially tapering the fiber in two adjacent locations to form the bottle (Poellinger *et al.*, 2009). To facilitate sensing applications, liquid core resonators were fabricated by blowing a silica microbubble (Sumetsky *et al.*, 2010). The process is similar to the traditional glass blowing, a gas pressure is applied while a glass capillary is heated.

To achieve on-chip integration, silica microtoroid cavities were fabricated on silicon wafers (Armani *et al.*, 2003). First, silica microdisks are made by photolithography and dry etching. Then the underneath silicon is selectively etched to form a post that supports the silica disk. Finally, a CO_2 laser beam irradiates a silica disk to melt the silica along the rim, and a toroid-like structure is formed by surface tension [Fig. 10(b)]. The reflow of silica produces a nearly atomic-scale surface finish, greatly enhancing the Q factor. The dimension of the toroid is determined by that of the initial disk and the reflow process. The toroid diameter is typically between 20 μm and 100 μm, and the toroid thickness is a few micron.

To make microspheres and microtoroids optically active, various approaches have been developed, such as fabricating the resonators from materials doped with active media, coating the resonators with light emitters, doping the resonators with gain material by ion implantation, etc. More detail about these approaches can be found in the review of He *et al.* (2013).

Single crystals have also been used to make spherical and toroidal cavities, and they are expected to have less loss and stronger nonlinear response than amorphous materials (Ilchenko and Matsko, 2006). The fabrication of crystalline spheres and toroids involves mechanical cutting, drilling and polishing. The typical diameter exceeds 1 mm. It is extremely difficult, if not impossible, to make microscale resonators with crystalline materials.

3. Microdisks and micropillars

Well-developed micro- and nano-fabrication technologies, such as photo-lithography, electron-beam lithography, chemical and physical etching, have been adopted to make microdisk and microcylinder resonators, allowing a precise control of the cavity shape and size. The commonly used materials are semiconductor and polymer. The latter can be either a passive polymer doped or coated with active material, e.g., dye-doped Poly(methyl methacrylate) (PMMA), or an active polymer such as poly(para-phenylene vinylene) (PPV) and poly(para-phenylene) (PPP). The polymer is first dissolved in a solvent and then spin-coated on a glass substrate. The layer thickness is a few hundred nanometer to one micron, depending on the spin speed and the concentration of the solution. To guide light in the polymer layer, its refractive index must be higher than that of the substrate. In the case the substrate has a large refractive index, a low-index material is deposited on the substrate first and then the polymer is spin-coated on top of it (Chern *et al.*, 2004; Lebental *et al.*, 2006). The disk patterns are written on a resist layer covering the polymer by photolithography or e-beam lithography, and then transferred to the polymer layer via wet or dry etching. Alternatively, microdisks may be made by direct photo-lithography or e-beam lithography with polymers or monomers that are active to UV light or electron beam (Djellali *et al.*, 2009; Fang and Cao, 2007). An additional bake may follow to reflow the polymer and smooth the disk edges. Figure 11(a) shows a DCM-doped PMMA disk of spiral shape.

Semiconductor microdisks/microcylinders have been made with GaAs/AlGaAs, InP/InGaAsP, Si, GaN/InGaN. They are single crystals grown by molecular beam epitaxy (MBE) or metal-organic chemical vapor deposition (MOCVD). The semiconductor disks have large refractive index contrast with the surrounding air, leading to strong light confinement even in small disks. It enables lasing in disks that are merely a few micron or even submicron in diameter (Song *et al.*, 2009a; Zhang *et al.*, 2007b). The disk thickness is typically a few hundred nanometer. Gain materials such as quantum wells (McCall *et al.*, 1992), quantum dots (Cao *et al.*, 2000), or nanocrystals (Liu *et al.*, 2004) are embedded in the disk layer or deposited on top of the disk. To isolate a disk from the high-index substrate, selective etching of the substrate forms a pedestal underneath the disk (Liu *et al.*, 2004). If this is not possible, e.g., the substrate is made of the same material as the disk, another semiconductor layer is grown between the disk and the substrate, and it is selectively etched to form a pedestal (McCall *et al.*, 1992), as shown in Fig. 11(b). The WGMs that locate near the edge of a disk are barely affected by the presence of the pedestal. Alternatively, a lower-index semiconductor layer is sandwiched between the higher-index disk layer and the substrate, enabling index-guiding of light in the disk layer (Fukushima and Harayama, 2004; Gmachl *et al.*, 1998).

In addition to the planar cavities, vertical cavities can be formed by stacking two Bragg mirrors. Standard lithography and etching have been used to make micropillars that are a few micron in height. Quantum wells or dots are embedded in the cavity. Figure 11(d) shows a micropillar with the limaçon-shaped cross-section. Since the spacing of the two Bragg mirrors is on the order of one wavelength, only one longitudinal mode of the cavity falls in the emission spectra. However, if the cross section of the cavity is large (a few tens of micron in diameter), multiple transverse modes exist, and they may produce complex field patterns (Gensty *et al.*, 2005; Huang *et al.*, 2002).

One advantage of the semiconductor microdisk/microcylinder lasers is that they can be pumped electrically with current injection [Fig. 11(c)], while previously discussed microcavities are optically pumped by another laser. However, their sidewall roughness, which is created during the fabrication process, is much larger than that of the surface-tension-formed microcavities. Since the melting temperature of GaAs/AlGaAs, InP/InGaAsP, or GaN/InGaN is very high, at which the quantum wells or quantum dots would be damaged, one cannot reflow the semiconductor to remove the sidewall roughness. Light scattering due to sidewall roughness reduce the quality factor, making the lasing threshold higher. One way of reducing the scattering loss is to make the sidewall wedge-shaped to push the optical modes away from the rough lithographic edge (Kippenberg *et al.*, 2006). Another solution is to replace the sidewall with the atomic-flat facets. This can be done with the bottom-up approach, e.g., which makes crystalline microdisks or microneedles (Gargas *et al.*, 2010; Zhu *et al.*, 2009). The cross sections of these cavities are polygons, so light may diffract from the sharp corners (Wiersig, 2003b).

E. Optical characterization

In this subsection, we describe the experimental techniques used to probe the microcavity resonances, e.g., their frequencies, quality factors, intracavity intensity distributions and far-field patterns. The characterization has been done on both passive cavities and active cavities that contain light emitting or amplifying media.

1. Passive cavities

To probe the resonances of a passive cavity, light must be efficiently coupled into the cavity. Several schemes have been developed. In terms of free-space coupling, a tightly focused Gaussian light beam passing outside but near a spherical cavity preferentially excite specific WGMs, depending on its distance from the cavity center (Lin *et al.*, 1998). For a deformed cavity, the modes with directional output can be efficiently excited by external beams in reversed directions. In addition to free-space coupling, cavity resonances may be excited with evanescent field couplers such as prisms, waveguides, tapered fibers. Typically, the input light is swept in frequency and a dip in the transmission spectrum gives the resonance frequency. The spectral width of the dip reflects the quality factor of the resonance. By varying the coupling position and/or direction, the intra-cavity mode profile may be inferred or confirmed (Gao *et al.*, 2007).

2. Active cavities

With light emitters embedded inside the microcavity or coated on its surface, the cavity resonances, especially the ones with high quality factors, appear as peaks in the spontaneous emission spectrum. The position and width of each peak tell the frequency and quality factor of the corresponding resonance. At high pump level, stimulated emission and lasing oscillation may occur.

Pumping can be either electrical or optical. The optical pumping is usually non-resonant, i.e., the frequency of the pump light differs from that of the emission. Thus the pump light and emitted light couple to different cavity modes. The pump beam may be incident onto the cavity from free space or coupled evanescently. To enhance the pump efficiency, ray and wave chaos were used to trap the pump light inside deformed microcavities (Lee *et al.*, 2007b).

A broad-band emission will couple to multiple cavity modes. The emission is collected either in free space or via an evanescent field coupler. Near-field imaging of light scattered at the cavity boundary reveals the locations where most emission escape from the cavity. The directions of the emission can be measured by placing a photodetector in the far-field zone and moving it around the cavity. A bandpass filter may be used to select one particular mode. To measure the spectra of emission into different directions, the detector is replaced by a fiber or fiber bundle connected to a spectrometer. The angle-resolved emission spectra give the far-field patterns of individual modes that appear in the spectra. Alternatively, a large ring may be fabricated around a microdisk, the in-plane emission from the disk reaches the ring and is scattered vertically. By imaging the intensity of scattered light along the ring from above the sample, one may infer the output directions (Song *et al.*, 2009b). A simultaneous measurement of the emission direction and location on the cavity boundary is possible by imaging the intensity profile from the sidewall of a micropillar as viewed from different angles (Schwefel *et al.*, 2004).

Finally we briefly discuss the microwave dielectric cavities. Most optical processes in passive microcavities can be studied in microwave cavities with higher precision (Bittner *et al.*, 2009; Kuhl *et al.*, 2011; Richter, 1999; Schäfer *et al.*, 2006). The much longer wavelength makes the microwave cavity much larger (see Fig. 1(d)) and thus much easier to fabricate. Moreover, both the amplitude and phase of the electromagnetic field can be readily measured at the microwave frequency by using antennas, which are difficult to realize in optics.

III. OVERVIEW OF NON-DEFORMED DIELECTRIC MICROCAVITIES

This section briefly reviews the properties of nondeformed WGM cavities.

A. Whispering gallery modes

For a circular microdisk with refractive index n and radius R the solution of the mode equation (8) with outgoing-wave condition (11) and with the requirement for a finite wave function inside the cavity is

$$\psi(r,\varphi) = \begin{cases} a_m J_m(nkr) e^{im\varphi} & \text{if } r \le R \\ b_m H_m^{(1)}(kr) e^{im\varphi} & \text{otherwise} \end{cases} , \tag{17}$$

where $m \in \mathbb{Z}$ is the azimuthal mode number, J_m and $H_m^{(1)}$ are the mth order Bessel function and first-kind Hankel function. The boundary conditions (9)-(10) lead to the "quantization condition"

$$S_m(kR) = 0 \tag{18}$$

with

$$S_m(kr) = \frac{n}{\mu}\frac{J_m'(nkr)}{J_m(nkr)} - \frac{H_m^{(1)'}(kr)}{H_m^{(1)}(kr)} , \tag{19}$$

where $\mu = 1$ $(= n^2)$ for TM (TE) polarization, and $'$ denotes the first derivative with respect to the argument. For given m Eq. (18) is to be solved numerically for the discrete values of $k = k_{ml} \in \mathbb{C}$ labeled by the radial mode number $l \in \mathbb{N}$.

Modes with azimuthal mode number $m \neq 0$ are two-fold degenerate due to the rotational symmetry. The mode with $m > 0$ $(m < 0)$ is a counterclockwise (clockwise) traveling wave in the azimuthal direction. Linear superpositions of these two modes are also modes of the cavity. A particular superposition are standing waves in the azimuthal direction with $\sin m\varphi$ and $\cos m\varphi$ dependence with m restricted to positive integers.

Figure 12 shows exemplarily two standing wave modes in the circular microdisk. Modes with small radial mode number l are called whispering-gallery modes. Beside the internal modes (Feshbach resonances) shown in Fig. 12 there are also external modes (shape resonances, above-barrier resonances) with much lower Q-factor which are located mostly outside the cavity (Bogomolny *et al.*, 2008; Dettmann *et al.*, 2009a; Dubertrand *et al.*, 2008; Nöckel, 1997). Only the internal modes become bound states in the small opening limit $n \to \infty$.

A straightforward calculation based on the stationary phase approximation shows that the Husimi function (14) of a mode in a circular microdisk (17) is strongly localized around

$$\sin\chi = \frac{m}{nkR} \;, \tag{20}$$

where kR is here understood as the real part of kR. This relation between ray and wave properties of the dielectric disk has been first derived by Nöckel and Stone (1995) using the eikonal approximation.

For microspheres analytical solutions of the mode equation are available in terms of vectorial spherical harmonics; see, e.g., in the review of Chiasera *et al.* (2010) on spherical WGM microresonators.

B. Optical losses and quality factors

In the ideal situation the quality factor (1) of an optical mode is determined solely by its radiation losses through the curved boundary of the cavity; $Q = Q_{\text{rad}}$. Asymptotic formulas for these losses are given in (Apalkov and Raikh, 2004; Dubertrand *et al.*, 2008; McCall *et al.*, 1992; Nöckel, 1997) for microdisks and in (Chiasera *et al.*, 2010) for microspheres. In practice, however, also absorption and Rayleigh scattering in the bulk material as well as scattering upon rough surfaces or contaminants contribute to the decay of light. According to Slusher *et al.* (1993) the total quality factor can be written as

$$\frac{1}{Q_{\text{total}}} = \frac{1}{Q_{\text{rad}}} + \frac{1}{Q_{\text{mat}}} + \frac{1}{Q_{\text{surf}}} \;. \tag{21}$$

The quantity Q_{mat} is related to the material absorption coefficient α by

$$Q_{\text{mat}} = \frac{2\pi n}{\lambda\alpha} \;, \tag{22}$$

where the dispersion of the refractive index n is ignored; λ is the vacuum wavelength. The coefficient α can also describe Rayleigh scattering in the bulk material which, however, can be significantly altered by the modified optical density of states in the presence of the microcavity (Gorodetsky *et al.*, 2000). These internal losses in the material can be alternatively taken into account by the mode equation using a complex-valued refractive index $\tilde{n} = n + i\lambda\alpha/4\pi$. Also the surface roughness $Q_{\rm surf}$ can be directly modeled by the mode equation provided that fluctuations in the boundary function $\rho = \rho(\varphi)$ are taken explicitly into account; see, e.g., (Rahachou and Zozoulenko, 2003).

The maximal total Q-factor achievable in microcavities depends on the size and refractive index (determining the radiation losses) and the quality of the material (determining the internal losses and surface scattering). For semiconductor microdisks the highest Q-factors can be achieved for "large" silicon cavities. Here, the Q ranges from $3 \cdot 10^6$ to $6 \cdot 10^7$ with disk radius of $20 - 60\,\mu$m (Borselli *et al.*, 2005; Kippenberg *et al.*, 2006; Soltani *et al.*, 2007). For AlGaAs disks with much smaller radius $2.25\,\mu$m the quality factor is lower but can be still high $Q \approx 3.5 \cdot 10^5$ (Srinivasan *et al.*, 2005). For a GaAs-disk with a tiny radius 361 nm the quality factor is still around 4000 (Song *et al.*, 2009a). For AlN/AlGaN microdisks of radii $2 - 5\,\mu$m the quality factor is ranging from 5000 to 7300 (Mexis *et al.*, 2011). For polymer-based microdisks a quality factor around 6000 has been reported (Lozenko *et al.*, 2012).

The Q-factors in microspheres are usually larger. For silica microspheres the record Q is around $8 \cdot 10^9$ (Gorodetsky *et al.*, 1996). For spherical droplets made of Rhodamine 6G in water solution a quality factor of about 10^8 has been measured (Lin, 1992). In microtoroid cavities the quality factors can be also very high, e.g., 10^8 for a toroid made of silica (Armani *et al.*, 2003).

Optical gain may be introduced to microcavities to compensate the optical losses mentioned above. Coherent amplification of light via stimulated emission effectively increases the photon lifetime, and reduces the mode linewidth. When optical amplification fully compensates the total loss, self-sustained oscillation occurs in the cavity, which corresponds to the onset of lasing action.

C. Lasing in whispering gallery cavities

Because of the high quality factors and the small mode volumes, WGM microcavities are excellent resonators for low threshold and narrow linewidth lasers. This subsection briefly reviews the pioneering works on WGM microlasers. More details can be found in a recent review on this topic by He *et al.* (2013).

Lasing in whispering-gallery cavities was first observed in spheres with diameter between 1 and 2 mm made of CaF_2 doped with Sm^{+2} (Garrett *et al.*, 1961). Later, stimulated emission in liquid ethanol droplets containing Rhodamine 6G dye as active medium was observed by Tzeng *et al.* (1984). Sandoghdar *et al.* (1996) have reported on the realization of a WGM laser based on neodymium-doped silica microspheres. A Raman laser with ultralow threshold based on a microsphere was fabricated by Spillane *et al.* (2002).

Lasing in microdisks has been first observed in semiconductor disks made of InP/InGaAsP with InGaAs quantum wells as active medium (McCall *et al.*, 1992). Stimulated emission from microdisks with InAs quantum dots as active medium has been reported by Cao *et al.* (2000). Liu *et al.* (2004) fabricated ultraviolet microdisk lasers on silicon substrates. The first room-temperature continuous-wave lasing in GaN/InGaN microdisks has been observed by Tamboli *et al.* (2007). Lasing in submicron disks has been achieved by Shainline *et al.* (2009); Song *et al.* (2009a); Zhang *et al.* (2007a). The first quantum cascade microdisk laser was demonstrated by Faist *et al.* (1996). Kuwata-Gonokami *et al.* (1995) achieved laser emission from polymer microdisk lasers.

Microlasers based on microtoroids covered by Erbium-doped sol-gel films have been fabricated by Yang *et al.* (2003). WGM Lasing in electrically driven quantum-dot micropillars has been achieved by Albert *et al.* (2010).

D. Evanescent field coupling

To couple light into and out of a WGM, an evanescent field coupler is often used. It provides efficient energy transfer through the evanescent field of a guided wave in a fiber/channel waveguide or the evanescent wave produced by total internal reflection of light at the surface of a dielectric prism/side-polished fiber (Chiasera *et al.*, 2010; Matsko and Ilchenko, 2006).

Let us consider a waveguide/fiber positioned parallel to the boundary of a microdisk/microsphere.

To couple light from the waveguide to a WGM in the cavity requires the phase synchronism, i.e. the tangential component of the wave vector of the guided wave matches that of the WGM. This can be achieved by adjusting the waveguide width or orientation. Complete energy exchange between the waveguide and the resonator is possible when the coupling strength matches the intrinsic loss of the resonator (Yariv, 2000). This is called critical coupling, a notion that was developed earlier in radio frequency (RF) engineering. By changing the distance from the waveguide to the cavity, the coupling strength is varied and the critical coupling may be reached for the lowest-order mode of the waveguide (Cai *et al.*, 2000). Parasitic coupling to higher-order waveguide modes and radiation modes is quantified by the "ideality" - the ratio of power coupled to a desired mode by power coupled or lost to all modes. An ideality of 99.97% was shown with the coupling of a tapered fiber to a silica microsphere (Spillane *et al.*, 2003).

Next we discuss the prism coupler by considering a microsphere placed on the surface of a dielectric prism (Gorodetsky and Ilchenko, 1994). A laser beam is directed into the prism and undergoes total internal reflection at the prism surface. The resulting evanescent optical field at the prism surface may be coupled to a WGM of the microsphere. The phase matching is obtained by adjusting the incident angle of the input light.

The evanescent field coupler has also been used as the output coupler for the WGMs. A detailed analysis of the coupling can be found in (Chiasera *et al.*, 2010; Gorodetsky and Ilchenko, 1999).

IV. SMOOTH DEFORMATION

In this section we discuss the properties of smoothly deformed microdisks cavities. The degree of deformation is here classified in terms of the chaoticity of the internal ray dynamics. To illustrate this concept, we consider a specific boundary curve, the limaçon of Pascal which reads in polar coordinates (r, φ)

$$r(\varphi) = R(1 + \varepsilon \cos\varphi) \ . \tag{23}$$

The limiting case of vanishing deformation parameter ε is the circle with radius R. An experimental realization is shown in Fig. 11(d).

For $\varepsilon < 0.5$ the limaçon shape is a smooth convex deformation of the circle. The ray dynamics in billiards with such a boundary obey the Kolmogorov-Arnol′d-Moser (KAM) theorem (Arnol′d, 1963; Kolmogorov, 1954; Moser, 1962). It states that for a sufficiently smooth perturbation of an integrable system some of the invariant tori survive, while others are destroyed giving rise to partially chaotic dynamics. Figure 13 illustrates this so-called KAM transition to chaos for the limaçon billiard by varying the deformation parameter ε from small to large values. For a small but nonzero value of ε most of the invariant curves survive with their shape sightly distorted. The others are replaced by chains of stable and unstable periodic orbits as dictated by the Poincaré-Birkhoff theorem (Lichtenberg and Lieberman, 1992; Ott, 1993). The stable periodic orbits are surrounded by new invariant curves which form small islands; see Fig. 13(a). The unstable periodic orbits are located in tiny chaotic layers not visible in Fig. 13(a). A boundary deformation which leads to such a nearly integrable ray dynamics is here classified as *weak deformation*.

Increasing the deformation parameter leads to the disappearance of more invariant curves and to an increase of the chaotic layers; cf. Fig. 13(b). The remaining invariant curves prevent rays from exploring the whole SOS. These curves act as barriers for the ray dynamics and divide the phase space into disjoint regions. This situation of a mixed phase space is classified here as *moderate deformation*. Note that as long as the billiard boundary is convex and sufficiently smooth, there is always an infinite family of invariant curves in the whispering-gallery region $|\sin\chi| \approx 1$. This fact is implied by Lazutkin's theorem (Lazutkin, 1973).

For *large deformation* these invariant curves and most of the others have been broken up and therefore the dynamics is predominately chaotic as shown in Fig. 13(c). A ray starting in the region well above the critical line can diffuse to the leaky region.

A. Weak deformation – nearly integrable ray dynamics

Considering the ray dynamics in smoothly deformed microcavities it seems that the case of weak deformation is not interesting. A ray starting well above the critical line for total internal reflection $|p| = |\sin\chi| > 1/n$ (see the invariant curve in the upper part of Fig. 13(a)) is not able to enter the leaky region and therefore no light is emitted. However, this reasoning is not the full picture for several reasons to be discussed in this subsection.

For systems with more than two degrees of freedom, e.g., deformed microspheres, the

KAM invariant curves no longer divide the phase space into disjoint regions, leading to the possibility of diffusion over large distances in phase space. This phenomenon is called Arnol′d diffusion (Arnol′d, 1964). It has been suggested to explain directional emission from deformed fused-silica microspheres (Fig. 1(c)) by Lacey and Wang (2001).

In the absence of Arnol′d diffusion the light output of a weakly deformed cavity is dominated by evanescent leakage (tunneling) of waves. It came as a surprise to observe experimentally directed emission even in this situation (Lacey *et al.*, 2003). This sensitivity to small shape deformations had been explained by preferential tunneling from the local minima of the invariant curves $|p(s)|$. Later, however, Creagh has provided a toy model which clearly demonstrated that the distinctness of the local minima of the invariant curves is not correlated with the degree of directionality of light emission (Creagh, 2007). Based on this observation Creagh and White (2010, 2012) introduced a more sophisticated explanation using the complex Wentzel-Kramers-Brillouin (WKB) approximation and canonical perturbation theory for weakly deformed microcavities.

The sensitivity of the emission directionality to weak boundary deformations can be further enhanced by a strong mixing of nearly degenerate modes induced by the deformation (Ge *et al.*, 2013a,b).

B. Moderate deformation – mixed phase space

1. Adiabatic curves and dynamical eclipsing

In the case of moderate deformation a considerable amount of rays is still confined by invariant curves; see upper part of Fig. 13(b). A ray starting in a sufficiently large chaotic part of phase space, however, can diffuse towards the leaky region and escape refractively; see around $\sin\chi \approx 0.5$ in Fig. 13(b). For moderate deformation the phase-space diffusion can be rather slow, so that the reduction of the Q-factor of the corresponding optical mode (Q-spoiling) is not serious (Mekis *et al.*, 1995; Nöckel *et al.*, 1994). Another consequence of the slow diffusion in $\sin\chi$ is that refractive escape typically occurs near the border of the leaky region, i.e. at the critical angle for total internal reflection χ_c, implying that the ray is emitted almost tangentially to the boundary of the cavity.

In two later papers Nöckel *et al.* (1996) and Nöckel and Stone (1997) showed that a ray in the diffusive part of phase space of a moderately deformed cavity follows for some time the adiabatic curve (see Fig. 14)

$$\sin\chi(s) = \sqrt{1 - \alpha\kappa(s)^{2/3}} \tag{24}$$

with α being an adiabatic constant and $\kappa(s)$ being the curvature of the boundary curve at the position s. Equation (24) is based on an adiabatic approximation introduced by Robnik and Berry (1985) for billiards in magnetic fields. For longer times the *chaotic whispering-gallery ray* diffuses to the leaky region by going through a continuous sequence of adiabatic curves (24) with slowly increasing α. In the moment when the adiabatic curve touches the critical angle χ_c the ray can escape tangentially. From Eq. (24) it can be seen that the mimina of the adiabatic curves occur at the points of maximum curvature. This is consistent with the intuitive expectation that the escape of light happens primarily near the points of maximum curvature. The localization in the spatial coordinate (at the maximum of the curvature) and in the angle (light is emitted tangentially) results in strong emission maxima in the far field in directions tangent to the highest-curvature points (Nöckel and Stone, 1997; Nöckel *et al.*, 1996).

Moreover, using the adiabatic curves allows to derive an approximate quantization of the system via the semiclassical Einstein-Brillouin-Keller (EBK) quantization scheme (Nöckel, 1997; Nöckel and Stone, 1997; Nöckel *et al.*, 1996). In this way a correspondence is made between a set of optical modes and a set of initial conditions for the rays in phase space. This correspondence is needed to set up a ray model to describe quantitatively the properties of optical modes, as mentioned in Sec. II.

The prediction based on Eq. (24) concerning the tangential emission from the highest-curvature points fails if regular islands are located at the critical angle right at the highest-curvature points; cf. Fig. 14 for the low refractive index $n = 1.54$. As the rays cannot enter the regular islands, they do not escape at the maximum of the curvature but mainly at two points separated by roughly the size of the islands. This effect is called *dynamical eclipsing* (Nöckel *et al.*, 1996). It leads to a splitting of the emission peaks in the far field. The first experimental demonstration of dynamical eclipsing of chaotic WGMs has been done for prolate-deformed lasing microdroplets (Chang *et al.*, 2000), see, e.g., Fig. 9. Later, dynamical eclipsing has been also observed in moderately deformed cylindrical polymer lasers (Schwefel *et al.*, 2004).

2. Gaussian modes based on stable periodic orbits

In moderately deformed microcavities there exist not only chaotic WGMs but also other types of long-lived modes depending on boundary shape and refractive index. A particular important example is the bowtie mode, see Fig. 15, first observed by Gmachl *et al.* (1998) in the flattened quadrupole

$$r(\varphi) = R\sqrt{1 + 2\varepsilon \cos 2\varphi}\ . \tag{25}$$

In phase space the bowtie mode is localized inside a regular island centered around a stable periodic ray with the shape of a bowtie. The periodic ray is born in a period-doubling bifurcation as the deformation parameter ε is increased through the critical value of about 0.1. For sufficiently high refractive index, $n \approx 3.3$, and $\varepsilon \approx 0.15$ the regular island is located right on the border of the leaky region which results in directed emission based on refractive escape (in mainly four directions; cf. Fig. 15) and moderate Q-factors. Gmachl *et al.* (1998) demonstrated high-power directional emission from such a bowtie mode in a semiconductor quantum cascade microlaser (Fig. 1(a)) with $R = 30 - 50\,\mu$m at wavelength of around $5.2\,\mu$m. This experiment can be considered as a milestone as it allowed for the first time to systematically vary the shape of a microdisk cavity in a controlled manner.

Optical modes based on regular islands in phase space can be analytically described in a generalized Gaussian optical approach based on the parabolic equation approximation (Tureci *et al.*, 2002).

3. Dynamical tunneling

Dynamical tunneling is a wave phenomenon which couples two distinct regions of ray-dynamical phase space (Davis and Heller, 1981); see also (Bäcker *et al.*, 2008b; Löck *et al.*, 2010). An example is the tunneling from a regular to the chaotic region in the phase space of the mushroom billiard, see Fig. 4, as studied theoretically and experimentally in a microwave mushroom billiard by Bäcker *et al.* (2008a).

Tunneling between regular islands that are separated by a chaotic sea can be enhanced by the presence of the chaotic part of phase space (Doron and Frischat, 1995; Podolskiy and Narimanov, 2003; Tomsovic and Ullmo, 1994). This *chaos-assisted tunneling* can be considered as a three-step process: (i) dynamical tunneling from the initial island into the chaotic sea, (ii) (classical) ray propagation through the chaotic sea to the border of the other island, and (iii) dynamical tunneling into the island. Chaos-assisted tunneling has been first experimentally observed in a microwave billiard (Dembowski *et al.*, 2000).

In open systems such as dielectric microcavities, however, chaos-assisted tunneling may also appear as a two-step process (Nöckel and Stone, 1997): (i) dynamical tunneling from the initial island into the chaotic sea and (ii) ray propagation through the chaotic sea into the leaky region where the ray escapes from the cavity. Effects of this two-step chaos-assisted tunneling have been often discussed for the annular microcavity where outside the leaky region a clear separation of two regular whispering-gallery regions and a chaotic region can be observed; see Fig. 8(a). While rays in these whispering-gallery regions stay in the cavity forever, the rays in the chaotic region can diffuse to the leaky region and leave the cavity. Hackenbroich and Nöckel (1997) showed that modes in this kind of cavity can show strong fluctuations of the quality factor due to dynamical tunneling between the different phase-space regions; for a general theory of this effect see (Podolskiy and Narimanov, 2005). Moreover, dynamical tunneling in this cavity can be utilized to achieve unidirectional light emission from high-Q modes (Wiersig and Hentschel, 2006). For the annular cavity, the quantitative connection of the quality factors to the dynamical tunneling has been established by Bäcker *et al.* (2009). Based on the concept of the fictitious integrable system (Bäcker *et al.*, 2008b) analytical expressions for the tunneling rates from the regular whispering-gallery region to the chaotic sea (see SOS for the annular cavity in Fig. 8(a)) can be derived. If rays in the chaotic region leave the cavity quickly, the dynamical tunneling rates approximate the cavity losses, and therefore allow to compute the Q-factors. The approximation can be improved by including the rates for *direct tunneling* along the radial degree of freedom to the exterior of the cavity; see Fig. 16.

Shinohara *et al.* (2010, 2011b) were the first to provided clear experimental evidence for dynamical tunneling in optical microcavities. They used a cavity whose ray dynamical phase space consists of a dominant chaotic region and an island chain, supporting a rectangular-shaped ray orbit fully confined by total internal reflection. Light emission from the corresponding optical mode happens via dynamical tunneling from the island chain to the chaotic sea. In such a situation, measuring the near and far fields of the light emission unambiguously proves the mechanism of dynamical tunneling (Podolskiy and Narimanov, 2005).

Another clear experimental demonstration of dynamical tunneling in optical microcavities has been achieved by free-space excitation of a liquid-jet cavity (Fig. 1(b)) (Yang *et al.*, 2010). Here, the light couples from outside to the chaotic sea inside the cavity and from there the light tunnels into regular islands which supports high-Q modes for lasing. This scheme is of practical use as the pump efficiency of this microcavity laser is increased by two orders of magnitude. The same scheme has been used to demonstrate experimentally tunneling-induced transparency in a chaotic microcavity similar to the case of electromagnetically induced transparency (Xiao *et al.*, 2013).

Chaos-assisted tunneling as a three-step process has been discussed to determine the frequency splitting of nearly degenerate bowtie modes (Fig. 15) in the quadrupole cavity (Podolskiy and Narimanov, 2003; Tureci *et al.*, 2002).

Another variant of dynamical tunneling is *resonance-assisted tunneling* (Ozorio de Almeida, 1984; Brodier *et al.*, 2001; Löck *et al.*, 2010). Here, island structures in phase space (also called nonlinear resonances) can enhance dynamical tunneling rates. Kwak *et al.* (2013) demonstrated resonance-assisted tunneling in a liquid-jet microcavity (Fig. 1(b)) by measuring avoided resonance spectral gaps which are proportional to the square of the phase-space area associated with the given island chain.

Chaos-assisted tunneling can be exploited for channeling rays into waveguides for efficient collection of light emission from microcavity lasers (Song *et al.*, 2012). Figure 17 shows that an attached waveguide introduces a vertical exit window in the phase space of the microcavity. This exit window seriously spoils the quality factor of (chaotic) WGMs but only mildly influences the quality factor of the modes related to the island chain around the diamond shaped period-4 orbit. In a laser based on this waveguide-cavity system these modes reach the lasing threshold first. Their emission is efficiently collected by the waveguide because emission is due to dynamical tunneling from the island chain into the chaotic sea from which most chaotic rays diffuse laterally to the exit window as illustrated in Fig. 17 instead of vertically down to the critical line. Using this scheme more than 95% of the emission can be collected by the waveguide.

C. Large deformation – predominantly chaotic dynamics

In the case of large boundary deformation the ray dynamics is predominantly chaotic. From a phase space plot such as in Fig. 13(c) one could naively expect that modes in a strongly deformed cavity should be short-lived and exhibit rather diffuse far-field pattern. This is, however, not necessarily the case as we see in the following.

1. *Chaotic saddle and its unstable manifold*

In nonlinear dynamics it is known for quite some time that the long-time behavior of an open chaotic system with time reversible dynamics is governed by the so-called *chaotic saddle* and its *stable and unstable manifolds*; see, e.g., (Lai and Tél, 2010; Lichtenberg and Lieberman, 1992). The chaotic saddle is the set of points in phase space that never visits the leaky region both in forward and backward time evolution. The stable (unstable) manifold of a chaotic saddle is the set of points that converges to the saddle in forward (backward) time evolution. The unstable manifold of the chaotic saddle therefore describes the route of escape from the chaotic system. The stable (unstable) manifold of the chaotic saddle is also called the *forward (backward) trapped set*. The intersection of both sets is the chaotic saddle. The concept of the chaotic saddle and its manifolds had been applied to several physical systems both classical and quantum mechanical; see, e.g., (Gaspard and Rice, 1989a,b). In the field of optics of deformed microcavities this knowledge has been reinvented to a large part as it is discussed below.

In experiments on polymer microlasers with various shapes, Schwefel *et al.* (2004) demonstrated that light emission from microcavities with predominately chaotic ray dynamics can be highly directional. This unexpected finding was explained by the numerical observation that typical rays escape the cavity by following the *unstable manifolds of short periodic orbits* close to boundary of the leaky region; see Fig. 18(a).

The stable (unstable) manifold of a periodic orbit is defined as the set of points in phase space which converge to the periodic orbit in the forward (backward) time evolution. The numerical simulation of intensity-weighted ray dynamics (13) shown in Fig. 18(a) revealed that the asymptotic escape behavior of initially randomly chosen rays above the critical line are well approximated by the unstable manifolds of short periodic orbits. This was nicely confirmed by wave simulations and by a reconstruction of light intensity in the leaky region of phase space by using experimental far-field data of multimode fields; cf. Figs. 18(a) and (b).

In the same year Lee *et al.* (2004) introduced the *survival probability distribution* (SPD) of intensity of rays inside the microcavity to explain the spatial localization of optical modes inside spiral-shaped cavities (an example is shown in Fig. 11(a)). The SPD is defined as the probability $P(s, p, t)$ with which a ray with Birkhoff coordinates (s, p) can survive in the cavity at time t. In strongly chaotic systems, this distribution decays exponentially in time, and the dependence on (s, p) is independent on initial conditions (Ryu *et al.*, 2006).

The SPD of Lee *et al.* (2004) and the computed asymptotic behavior of initially randomly chosen rays by Schwefel *et al.* (2004) is equivalent to the unstable manifold of the chaotic saddle extended by the intensity-weighted ray dynamics (13) as first noted by Wiersig and Hentschel (2008). A systematic and clear discussion of this extended version of the chaotic saddle and its relation to the ergodic theory of transient chaos can be found in (Altmann, 2009; Altmann *et al.*, 2013). Altmann (2009) pointed out that the unstable manifolds of short periodic orbits (which are part of the chaotic saddle) close to the critical line as discussed by Schwefel *et al.* (2004) are parallel to the unstable manifold of the chaotic saddle and therefore lead to nearly the same far-field emission.

Often, the term "chaotic repeller" instead of "chaotic saddle" is used to describe the light emission from dielectric cavities. However, as emphasized by Altmann (2009), the term "chaotic saddle" is more appropriate as the dynamics is time reversible. A "chaotic repeller" appears in noninvertible dynamical systems and possess only unstable manifolds (Lai and Tél, 2010).

The emission mechanism along the unstable manifold of the chaotic saddle indicates that all long-lived modes in a given strongly deformed microcavity exhibit a similar far-field pattern; see Fig. 19. This *universal* output directionality of *single modes* was proven without ambiguity in experiments on a liquid-jet microcavity (Lee *et al.*, 2007c). Using this concept Wiersig and Hentschel (2008) provided numerical evidence that all long-lived modes in the limaçon cavity (23) with deformation parameter $\varepsilon \approx 0.43$ and refractive index between 2.7 and 3.9 exhibit the universal and *unidirectional* light emission. This was confirmed experimentally by a number of groups (Albert *et al.*, 2012; Shinohara *et al.*, 2009; Song *et al.*, 2009b; Wang *et al.*, 2009; Yan *et al.*, 2009; Yi *et al.*, 2009).

In the case of mixed phase space the chaotic saddle is divided into hyperbolic and nonhyperbolic components (Altmann, 2009). The mechanism of escape of electromagnetic radiation along the unstable manifold works also in this case as demonstrated by experiments on microwave cavities of quadrupolar shape (Schäfer *et al.*, 2006). Moreover, a combination with dynamical tunneling is possible. As discussed in subsection IV.B.3 Shinohara *et al.* (2010, 2011b) demonstrated experimentally and theoretically that modes localized in an island chain (a nonhyperbolic component) can tunnel into the chaotic sea (the hyperbolic component). From there, the rays follow the unstable manifold of the chaotic saddle.

The details of the relation between optical modes and the chaotic saddle of the ray dynamics are still not fully understood. For open quantum maps it has been rigorously proven that in the semiclassical limit the right eigenvectors of the non-unitary time evolution matrix U are supported by the corresponding classical unstable manifold of the chaotic saddle (Keating *et al.*, 2006). Long-lived states are localized on the chaotic saddle (which is part of the unstable manifold). The localization, however, is not uniform because of quantum fluctuations. In the case of microcavities these fluctuations can have a significant impact on the far-field emission pattern (Shinohara *et al.*, 2008, 2009).

2. Dynamical localization and scar modes

It is natural to expect that modes in chaotic microdisks have low-Q factors. This Q spoiling (Nöckel and Stone, 1995; Nöckel *et al.*, 1994) would limit the possible applications of deformed microdisks considerably. However, wave localization effects discovered in the field of quantum chaos provide the possibility of high-Q modes in chaotic microcavities. For example, wave packets mimic to some extend the chaotic ray diffusion in phase space. However, destructive interference suppresses the chaotic diffusion on long time scales (Borgonovi *et al.*, 1996; Casati *et al.*, 1979; Fishmann *et al.*, 1982; Frahm and Shepelyansky, 1997). This *dynamical localization* in phase space is closely related to real-space Anderson localization in disordered solids (Fishmann *et al.*, 1982). The first experimental observation of dynamical localization was reported by Moore *et al.* (1994) using ultracold atoms placed in a modulated standing wave of a near-resonant laser.

Another experimental verification of dynamical localization used a microwave circular billiard with boundary roughness (Sirko *et al.*, 2000). In the regime of dynamical localization, the angular momentum $l \sim \sin\chi$ in such a "rough billiard" is exponentially localized around a mode-dependent value. The localization in $\sin\chi$ is of interest for optical microcavities as it suppresses the diffusion into the leaky region and therefore allows for modes with high quality factor even in the regime of fully chaotic ray dynamics (Frahm and Shepelyansky, 1997). The first theoretical study of dynamical localization in optical microdisks with boundary roughness has been performed by Starykh *et al.* (2000). They showed that the dynamical localization leads to a log-normal distribution of the modes' linewidths/decay rates. The direct observation of lasing action from dynamically-localized modes has been reported by Podolskiy *et al.* (2004) and Fang *et al.* (2005a) using GaAs-InAs microdisks with enhanced boundary roughness; see Fig. 20.

Another wave localization phenomenon known from closed chaotic systems is *scarring* (Heller, 1984). It refers to the existence of a small fraction of quantum eigenstates with strong concentration along unstable periodic orbits of the underlying classical system. In optical microcavities, the localization of wave intensity along unstable periodic ray trajectories has been observed experimentally first in liquid-jet microlasers (Lee *et al.*, 2002) and shortly after in GaN microlasers (Rex *et al.*, 2002) and in GaAs/GaInAs/GaInP quantum well microlasers (Gmachl *et al.*, 2002). The observed modes, such as the one shown in Fig. 21, can have high quality factors since the corresponding short periodic orbit is located entirely outside the leaky region, and is therefore part of the chaotic saddle.

A well studied system in the field of quantum chaos is the stadium billiard given by two semicircles and two parallel segments. This system is not a smooth deformation of the circle as the radius of curvature changes discontinuously at the points of connection. For this billiard it is rigorously proven that the ray dynamics is fully chaotic, i.e. there are no regular regions in phase space (Bunimovich, 1974). A microcavity of stadium shape is shown in Fig. 11(c). Theoretical analyzes of such a microcavity revealed a localization along multiple periodic orbits (Fang *et al.*, 2005b; Harayama *et al.*, 2003). Associated with this localization is a non-monotonic decrease of the Q-factor with increasing deformation because of interference of waves propagating along different constituent orbits (Fang *et al.*, 2005b). This interference effect has been discussed in terms of a periodic-orbit-sum formula by Fukushima *et al.* (2006). These theoretical findings have been confirmed experimentally in GaAs/AlGaAs (Harayama *et al.*, 2003), GaAs (Fang *et al.*, 2007) and polymer microstadia (Fang and Cao, 2007). The observation of localization along multiple periodic orbits is consistent with a recent study of an open three-disk system (Weich *et al.*, 2014) which relates this phenomenon to the formation and interaction of resonance chains in the complex frequency plane.

Numerical simulations indicate that scarring in optical microcavities with strongly chaotic ray dynamics is rather the rule than the exception; see, e.g., (Fang and Cao, 2007; Fang *et al.*, 2007, 2005b; Harayama *et al.*, 2003; Lee *et al.*, 2002, 2007c, 2004, 2005; Rex *et al.*, 2002; Wiersig, 2006; Wiersig and Hentschel, 2008; Wiersig *et al.*, 2010). This conclusion can also be drawn from studies of open quantum maps (Ermann *et al.*, 2009; Wisniacki and Carlo, 2008).

An interesting phenomenon not observed in any closed system is the appearance of *quasiscarred modes* showing a strong localization on simple geometric structures with no underlying periodic ray (Lee *et al.*, 2004, 2008a). Lasing on quasiscarred modes has been successfully realized for spiral-shaped InGaAsP microcavity lasers (Kim *et al.*, 2009). Quasiscars find a natural explanation in terms of an extended ray dynamics as discussed in Sec. VIII.A.

3. Level statistics

A central topic of quantum chaos is the analysis of the statistical properties of energy levels in quantum systems whose classical counterpart is chaotic (Stöckmann, 2000). In the last decade, the focus has shifted from closed to open systems. For a review of unsolved problems in this field consult (Nonnenmacher, 2011).

One particularly interesting aspect is the *fractal Weyl law* for long-lived states in open fully chaotic systems. This conjecture, based on the work of Sjöstrand (1990) and Zworski (1999), is an extension of the well-known Weyl's formula for closed systems. The Weyl's formula states that the number of energy levels $N(k)$ with wave number $k_m \leq k$, or more precisely, the smooth part of it, $\bar{N}(k)$, behaves asymptotically as $\sim k^2$ for the particular case of a two-dimensional system which scales with the energy such as quantum billiards. For an open system the number of resonances with complex wave numbers k_m can be defined as

$$N_C(k) = \{k_m : \mathrm{Im}(k_m) > -C,\ \mathrm{Re}(k_m) \leq k\}\ . \tag{26}$$

The cutoff constant $C > 0$ ensures that only long-lived states are taken into account; fast decaying states are ignored. The fractal Weyl law for an open chaotic system (which again scales with the energy) can be written as

$$\bar{N}_C(k) \sim k^{\alpha} \; . \tag{27}$$

It is conjectured that the non-integer exponent in Eq. (27) is

$$\alpha = \frac{D+1}{2} = \frac{d+2}{2} \; , \tag{28}$$

where D is the fractal dimension of the chaotic saddle/repeller (Lin and Zworski, 2002); $d = D - 1$ is the dimension of the saddle in a properly chosen SOS.

The fractal Weyl law has been numerically confirmed for a number of physical model systems: a three-bump scattering potential (Lin, 2002; Lin and Zworski, 2002), a three-disk system (Lu *et al.*, 2003), open quantum maps (Nonnenmacher, 2006; Schomerus and Tworzydlo, 2004; Shepelyansky, 2008), a Hénon-Heiles Hamiltonian with Coriolis term (Ramilowski *et al.*, 2009), and a four-sphere system (Eberspächer *et al.*, 2010). The asymptotic form (27) has been rigorously proven only for a simplified variant of the open quantum baker's map (Nonnenmacher and Zworski, 2007). Experimental evidence for the fractal Weyl law has been obtained for a five-disk microwave system (Potzuweit *et al.*, 2012).

For dielectric cavities the situation is more complicated than in the above examples. First, a dielectric cavity possesses internal and external modes (Bogomolny *et al.*, 2008; Dettmann *et al.*, 2009a; Dubertrand *et al.*, 2008); see the discussion in Sec. III. However, the latter are extremely short-lived and are therefore conveniently withdrawn from the counting process by the cutoff constant C. Second, the *partial* leakage of intensity according to Fresnel's laws has an important implication. Consider a dielectric cavity (n finite) and the corresponding closed billiard system ($n \to \infty$). The states in the billiard system have zero decay rate and their number satisfies the conventional Weyl law. When the openness of the system is gradually increased by reducing n, each mode acquires a nonzero but finite decay rate because the transmission through the boundary is not complete (except at Brewster's angle for TE polarization). Therefore, "no mode can disappear to infinity" along the imaginary direction in complex frequency space. This implies that the total number of internal modes of a dielectric cavity fulfills the conventional k^2 law as it was pointed out by Bogomolny *et al.* (2008). This, however, is not in contradiction with the fractal Weyl law which applies to the long-lived modes within the set of internal modes.

The fractal Weyl law for dielectric microcavities has been tested only for the stadium-shaped cavity (Wiersig and Main, 2008). The numerically computed spectral data is consistent with the fractal Weyl law if the concept of the chaotic saddle is extended to a multifractal by using the intensity-weighted ray dynamics (13) incorporating Fresnel's laws (Wiersig and Main, 2008). However, Nonnenmacher and Schenk (2008) demonstrated that a damped quantum map used as a toy model for dielectric cavities shows the conventional Weyl law.

While the Weyl law characterizes the smooth part of the density of states, the statistical analysis of the energy levels addresses the fluctuations in the density of states. For closed chaotic systems random-matrix theory (RMT) has been applied successfully to describe the universal properties of the spectral statistics; see, e.g., the book of Stöckmann (2000). Quantum eigenenergies of open systems are complex valued with the imaginary part being related to the decay rate and the lifetime of the state. In the case of open systems much work is devoted to resonators with small openings (Fyodorov and Sommers, 1997; Misirpashaev and Beenakker, 1998). Dielectric microcavities, however, allow for refractive escape along the entire boundary, and are in this sense far more open than the resonators considered in standard RMT. It is more related to microwave billiards with an absorber region extended over a significant part of the boundary (Kuhl *et al.*, 2008; Poli *et al.*, 2012).

The first theoretical study of spectral statistics of dielectric cavities has been performed by Starykh *et al.* (2000) in the context of dynamical localization. It was demonstrated for a rough dielectric disk that in the presence of dynamical localization the decay-rate distribution exhibits a log-normal behavior.

The statistics of frequencies in the ideal dielectric disk have been studied numerically and analytically by Ryu *et al.* (2008). As expected for a system with integrable ray dynamics the nearest level spacing distribution (of the real part of the frequencies) is in good agreement with the Poisson distribution. The decay-rate distribution shows a peak structure which details are consistent with the properties of the survival probability distribution.

A RMT model for deformed dielectric cavities has been developed by Keating *et al.* (2008). It combines the internal wave chaos and the Fresnel laws for reflection and refraction at the cavity's boundary. For large refractive index the spectral properties are consistent with RMT for systems with small openings. For low refractive index, the details of the statistics become nonuniversal. Schomerus *et al.* (2009) have confirmed that the model is capable to accurately describe the numerically obtained data for a dielectric microstadium.

An experimental study of the statistical properties of dielectric microcavities in the optical regime has not been done yet. However, an interesting experiment on an optical microstadium billiard bounded by a two-dimensional photonic crystal and attached to waveguides shows good agreement with RMT for systems with a small number of openings (Di Falco *et al.*, 2012).

4. Partial barriers and turnstile transport

In the regime of large deformation all KAM invariant curves, separatrices, and islands are broken. There are no longer perfect barriers which prevent classical trajectories or rays from diffusing across the entire SOS, see, e.g., the transition circle-oval-stadium studied by Tanaka *et al.* (2007). But there are imperfect or *partial barriers*, remnants of the broken invariant structures in phase space (Bensimon and Kadanoff, 1984; MacKay *et al.*, 1984); see also the review by Meiss (1992). On intermediate time scales, a trajectory first explore one subregion of the chaotic sea without crossing the partial barrier under consideration. Later, the trajectory crosses the partial barrier and explores the next subregion, etc. The transport through such a partial barrier resembles that through a revolving door or *turnstile*.

It is well known that these partial barriers to classical dynamics can act as perfect barriers to quantum wave packet evolution (Brown and Wyatt, 1986; Geisel *et al.*, 1986). This happens when the *action flux* Φ (the phase-space area escaping through the partial barrier per iteration) is much less than Planck's constant h (MacKay *et al.*, 1984; MacKay and Meiss, 1988). The *turnstile transport* is then suppressed by the quantum mechanical uncertainty principle. The partial barriers therefore lead to localization of energy eigenstates (Casati and Prosen, 1999). Experimental evidence for this kind of quantum localization phenomenon has been found in ultracold cesium atoms in a standing wave of near resonant light (Vant *et al.*, 1999). For a designed quantum map with an isolated partial barrier it has been shown that the quantum localizing transition is universal with the scaling parameter Φ/h (Michler *et al.*, 2012). The width of this transition is rather broad, being two orders of magnitude in Φ/h.

For deformed microcavities the first theoretical and experimental observation of an uncertainty-limited turnstile transport has been reported by Shim *et al.* (2008). The role of h is here played by the effective Planck's constant $h_{\text{eff}} = 1/nkR$. In the experiment a liquid-jet cavity with quadru-octapole shape

$$r(\varphi) = R(1 + \eta_0 \cos 2\varphi + \varepsilon\eta_0^2 \cos 4\varphi) \tag{29}$$

is used; $R = 14.8\,\mu\text{m}$, $\varepsilon = 0.46$, and refractive index $n = 1.361$. As the deformation parameter η_0 is varied from 0 to 0.26 the suppression of turnstile transport can be identified by the behavior of the far-field emission pattern measured experimentally and compared to ray simulations.

For the same kind of liquid-jet cavity with quadru-octapole shape (29) it has been demonstrated that the concept of turnstile transport can be exploited to enhance the efficiency of optical pumping (Yang *et al.*, 2008) by one order of magnitude. To do so, the pump beam is tightly focused onto the relevant turnstile in the time-reversed ray dynamics. In this way, it is ensured that the pump intensity is efficiently transported to the whispering-gallery regions of phase space where the long-lived modes are located.

The suppression of chaotic diffusion by partial barriers can lead to the adiabatic formation of high-Q WGMs in strongly deformed microcavities (Shim *et al.*, 2013, 2011), in particular in the ultrasmall regime where the vacuum wavelength λ is of the order of the average radius R of the cavity. This effect provides a natural explanation of the observed lasing action from InAs quantum dots in strongly deformed GaAs microdisks with R below $1\,\mu\text{m}$ (Song *et al.*, 2010).

Note that many aspects discussed here for the chaotic phase space of a strongly deformed cavity apply equally to the chaotic component of the mixed phase space of a cavity with moderate boundary deformation.

D. Perturbation theory

In this subsection we review a powerful perturbation theory for optical modes in deformed microcavities introduced by Dubertrand *et al.* (2008) for TM polarization. The extension to TE polarized modes can be found in (Ge *et al.*, 2013b). The perturbation theory treats a boundary deformation of the form

$$r(\varphi) = R\,[1 + \lambda f(\varphi)] \tag{30}$$

in polar coordinates (r, φ). R is the radius of the unperturbed disk for which the solutions of the mode equation (8) are known, λ is a formal perturbation parameter. The deformation function $f(\varphi)$, which we define here to be dimensionless in contrast to Ref. (Dubertrand *et al.*, 2008), is assumed to be single-valued and symmetric: $f(-\varphi) = f(\varphi)$. The perturbation theory in its present formulation is restricted to cavities with at least one mirror-reflection symmetry. Modes in this kind of cavity can be classified as odd-symmetry and even-symmetry modes. The formulas given below are restricted to even-symmetry modes. For odd-symmetry modes all cos functions have to be replaced by sin functions.

The perturbation theory is valid in the perturbative regime

$$k^2\delta a \ll 1 \ , \tag{31}$$

with k being the wave number and δa being the area where the perturbation in terms of the refractive index is nonzero; cf. Fig. 22. For some more, subtle details consider (Dubertrand *et al.*, 2008). It is important to emphasize that the perturbation theory applies also to cavities with large boundary deformation as long as the wave number k is sufficiently small such that the validity of the perturbative regime (31) is guaranteed.

A WGM in an ideal circular cavity is characterized by the azimuthal mode number m and the radial mode number l with dimensionless frequency $\Omega_0 = k_0 R$ given by the quantization condition (18). For the frequency of the perturbed mode $\Omega = kR$ it is found up to order $\mathcal{O}(\lambda^2)$

$$\begin{aligned}\Omega = \Omega_0 \Bigg[1 - \lambda A_{mm} + \lambda^2 \Bigg(& \frac{3A_{mm}^2 - B_{mm}}{2} \\ & + \Omega_0 (A_{mm}^2 - B_{mm}) \frac{H_m^{(1)\prime}(\Omega_0)}{H_m^{(1)}(\Omega_0)} \\ & - (n^2-1)\Omega_0 \sum_{\substack{j=0 \\ j\neq m}}^{\infty} A_{mj} \frac{1}{S_j(\Omega_0)} A_{jm} \Bigg) \Bigg]\end{aligned} \tag{32}$$

with

$$A_{pm} = \frac{\varepsilon_p}{\pi} \int_0^{\pi} f(\varphi) \cos{(p\varphi)} \cos{(m\varphi)} d\varphi \ , \tag{33}$$

$$B_{pm} = \frac{\varepsilon_p}{\pi} \int_0^{\pi} f^2(\varphi) \cos{(p\varphi)} \cos{(m\varphi)} d\varphi \ , \tag{34}$$

$$\varepsilon_p = \begin{cases} 2 & \text{for } p \neq 0 \\ 1 & \text{for } p = 0 \ . \end{cases} \tag{35}$$

The wave function with azimuthal mode number m inside and outside the cavity is

$$\psi_{\text{in}}(r,\varphi) = \frac{J_m(nkr)}{J_m(n\Omega)}\cos(m\varphi) + \sum_{\substack{p=0\\p\neq m}}^{\infty} a_p \frac{J_p(nkr)}{J_p(n\Omega)}\cos(p\varphi) \ , \tag{36}$$

$$\psi_{\text{out}}(r,\varphi) = (1+b_m)\frac{H_m^{(1)}(kr)}{H_m^{(1)}(\Omega)}\cos(m\varphi) + \sum_{\substack{p=0\\p\neq m}}^{\infty}(a_p+b_p)\frac{H_p^{(1)}(kr)}{H_p^{(1)}(\Omega)}\cos(p\varphi) \tag{37}$$

with coefficients up to order $\mathcal{O}(\lambda^2)$

$$\begin{aligned} a_p = \lambda\Omega_0(n^2-1)\frac{1}{S_p(\Omega_0)}\Bigg(A_{pm} &+ \lambda\left\{A_{pm}A_{mm}\left(\frac{\Omega_0}{S_p(\Omega_0)}\frac{\partial S_p(\Omega_0)}{\partial\Omega_0} - 1\right)\right. \\ &+ \frac{B_{pm}}{2}\left[1 + \Omega_0\left(\frac{H_m^{(1)\prime}(\Omega_0)}{H_m^{(1)}(\Omega_0)} + \frac{H_p^{(1)\prime}(\Omega_0)}{H_p^{(1)}(\Omega_0)}\right)\right] \\ &\left.+ \ \Omega_0(n^2-1)\sum_{\substack{j=0\\j\neq m}}^{\infty} A_{pj}\frac{1}{S_j(\Omega_0)}A_{jm}\right\}\Bigg) \ , \end{aligned} \tag{38}$$

$$b_p = \lambda^2\frac{\Omega_0^2}{2}(n^2-1)B_{pm} \ . \tag{39}$$

If the frequency Ω_0 of the unperturbed mode with azimuthal mode number m is nearly degenerate with the frequency of another unperturbed mode with azimuthal mode number $j \neq m$ then the term $1/S_j(\Omega_0)$ in Eqs. (32) and (38) become considerably large. It such a case the perturbation treatment requires modification (Dubertrand *et al.*, 2008).

From Eq. (37) the far-field amplitude $F(\varphi)$ can be derived by exploiting the asymptotical behavior of the Hankel function for large r to give

$$F(\varphi) = (1+b_m)\frac{e^{-i\pi m/2}}{H_m^{(1)}(\Omega)}\cos(m\varphi) + \sum_{\substack{p=0\\p\neq m}}^{\infty}(a_p+b_p)\frac{e^{-i\pi p/2}}{H_p^{(1)}(\Omega)}\cos(p\varphi) \ . \tag{40}$$

The perturbation theory has been applied successfully to compute frequencies, Q-factors and far-field patterns of the cut disk cavity (Dubertrand *et al.*, 2008), microcavities subjected to local boundary perturbations (Wiersig, 2012), and the limaçon cavity (Kraft and

Wiersig, 2014). In all cases the internal ray dynamics is strongly chaotic, i.e. the degree of deformation can be considered to be large. Nevertheless, the wave number k is such that the left-hand side of Eq. (31) is below 1 or close to it. Therefore, the system is in the perturbative regime.

Moreover, the perturbation theory has been proven to be very useful for developing an understanding of an extreme sensitivity of the far-field pattern to subwavelength boundary deformations (Ge *et al.*, 2013b). Another application is the description of multimode coupling by boundary wave scattering (Ge *et al.*, 2013a).

V. CAVITY WITH SHARP CORNER OR BOUNDARY DEFECT

In the previous section, we described the smoothly deformed cavities. In this section, we will consider cavities with a discontinuity at the boundary, and describe how the sharp corners or boundary defects influence the optical modes and ray dynamics.

A. Polygonal cavity

Polygonal cavities differ from the cavities with smooth boundary in two respects. First, they can be fabricated with the bottom-up approach, namely they are self-assembled during the crystal growth processes, leading to crystal facets with a high degree of perfection. Second, the ray dynamics in polygonal billiards is neither chaotic – there is no exponential divergence of trajectories – nor integrable (apart from the rectangles, the equilateral triangles, the $\pi/2, \pi/4, \pi/4$-triangles, and the $\pi/2, \pi/3, \pi/6$-triangles). The motion inside a typical polygon is conjectured to be ergodic on the three-dimensional constant-energy surfaces in phase space (Gutkin, 1996), while the motion inside a rational polygon (all angles are rationally related to π) is restricted to two-dimensional invariant surfaces, like in integrable systems, but the genus of the surfaces is larger than 1; loosely speaking, such a surfaces is a torus with additional handles. Rational polygonal billiards are therefore characterized as *pseudo-integrable* (Richens and Berry, 1981). The dynamics on such a surface of higher genus is not quasiperiodic, which is reflected by multifractal Fourier spectra of dynamical variables (Artuso *et al.*, 2000; Wiersig, 2000). Moreover, the quantum-classical correspondence is exotic (Bogomolny and Schmit, 2004; Wiersig, 2001) and the quantum spectrum obeys critical statistics (Bogomolny *et al.*, 1999; Wiersig, 2002).

However, it has turned out that the properties of rays and modes in dielectric polygons are simpler, in particular if the system is strongly open as in the case of low refractive index contrast (Wiersig, 2003b). Often, it is sufficient to discuss one or two families of periodic ray trajectories to understand the basic optical properties.

The most frequently studied polygonal dielectric cavity is the regular hexagon. The first microcavities with the shape of a regular hexagon have been zeolitic aluminophosphate-cavities with side length R ranging from 2.6 to $4.6\,\mu$m (Braun *et al.*, 2000; Vietze *et al.*, 1998); see Fig. 23(a). These cavities have been used for microlasers by putting organic laser active dye guest molecules into the channel pores of the zeolitic crystal. Numerical simulations have shown that in this kind of low-index cavity ($n = 1.466$, $\lambda \approx 690\,$nm) the light is localized on whispering-gallery-like modes along a family of periodic-6 ray trajectories, which is the only one confined by total internal reflection (Braun *et al.*, 2000); see Fig. 23(b) and (c). Most of the features of these modes can be explained by a semiclassical approximation ($R \gg \lambda$) based on wave interference along the periodic-6 orbits to determine the resonant frequencies, and pseudointegrable ray dynamics and boundary waves to determine the quality factors (Wiersig, 2003b).

Hexagonal-shaped cavities have also been realized as cross-section of ZnO nanoneedles, nanonails, nanodisks, and microwires. Since the refractive index $n \approx 2$ ($n \approx 2.35$ in the ultraviolet) is larger, other orbits than the periodic-6 orbit are confined by total internal reflection, e.g., periodic-3 orbits with the shape of an equilateral triangle, which can lead to higher Q-factors (Kouno *et al.*, 2011; Song *et al.*, 2013a). The nanoneedles studied by Nobis *et al.* (2004) have a conical shape with diameter varying smoothly from 900 down to 270 nm; $\lambda \approx 530\,$nm. This smooth variation of the diameter permitted a systematic study of the whispering-gallery-like modes for small azimuthal mode numbers m in good agreement with the theory by Wiersig (2003b) even close to the ground state. Explicit numerical simulations of low-order modes can be found in (Nobis and Grundmann, 2005).

WGMs have also been observed in experiments on hexagonal ZnO nanodisks (Kim *et al.*, 2006) and nanonails (Liu *et al.*, 2008) and for other material systems, such as GaN (Peng *et al.*, 2005; Tessarek *et al.*, 2013), GaAs (Paek *et al.*, 2010), In_2O_3 (Dong *et al.*, 2009), and Al_2O_3 (Kudo *et al.*, 2013).

Optically pumped WGM lasing action in hexagonal nano- and microresonators has been achieved for ZnO nanonails (Wang *et al.*, 2006), ZnO nanodisks (Gargas *et al.*, 2010), ZnO microwires (Czekalla *et al.*, 2008), ZnO microneedles (Zhu *et al.*, 2009), ZnO nanodisks (Yu *et al.*, 2007), GaN microdisks (Kouno *et al.*, 2011), and InGaAs nanopillars (Chen *et al.*, 2011).

Experiments and simulations on ZnO microwires with slightly deformed (elongated, bent) hexagonal cross-section show the appearance of in-plane Fabry-Pérot modes and WGMs based on periodic-3 orbits (Dietrich and Grundmann, 2012; Dietrich *et al.*, 2011).

The effect of rounding the corners of hexagonal microcavities has been studied in (Dietrich *et al.*, 2012; Kudo *et al.*, 2013; Wiersig, 2003b). While Wiersig (2003b) and Kudo *et al.* (2013) concluded that rounding the corners increases the Q-factor, Dietrich *et al.* (2012) claimed the opposite. It is, however, possible that the conclusion of Dietrich *et al.* (2012) is spoiled by surface roughness in the experiment and the peculiar way the corners are rounded in the numerical simulations.

Other dielectric polygonal cavities have been studied as well, such as squares (Chen *et al.*, 2006; Guo *et al.*, 2003; Lohmeyer, 2002; Poon *et al.*, 2001), rectangles (Wiersig, 2006), regular pentagons (Bogomolny *et al.*, 2011; Lebental *et al.*, 2007), equilateral triangles (Lai *et al.*, 2007; Wysin, 2005), regular dodecagons (Nobis *et al.*, 2007), and octahedrons (Korthout *et al.*, 2009).

A deep insight into the structure of optical modes in polygonal microcavities has been provided by the superscar model (Lebental *et al.*, 2007), which had been originally invented for polygonal billiards (Bogomolny and Schmit, 2004) and experimentally confirmed in microwave cavities (Bogomolny *et al.*, 2006). In brief, the families of periodic ray trajectories in polygonal cavities are unfolded to fictitious straight rectangular channels passing through cavity corners. In the semiclassical limit, wave functions obey simple boundary conditions on the channel boundaries. One can therefore consider the wave functions as states confined in the rectangles, which allows to derive analytic solutions.

B. Boundary defect

Levi *et al.* (1993) were the first who demonstrated that a microdisk with a local boundary defect can show improved emission directionality. The fabricated defect was a small deformation of the boundary with the shape of a “tab”. The same shape and the inverted version (a "notch") had been used by Backes *et al.* (1998) for the same purpose and also for mode discrimination. Microwave studies of dielectric disks with notch were performed by Kuhl *et al.* (2011). Boriskina *et al.* (2006) suggested the possibility to further improve the directionality by using an ellipse with a notch. This idea has been realized in experiments on elliptical-shaped quantum cascade lasers (Wang *et al.*, 2010). It has been demonstrated that this geometry allows for unidirectional light emission with very low divergence angle and high quality factors. The mechanism behind this observation is roughly (for details see Section VII.F) that the notch acts as a small scatterer that scatters light rays towards the opposite side of the elliptical cavity, where the outgoing rays are collimated as a parallel beam by the elliptical boundary. To achieve this goal for a given refractive index, the eccentricity of the ellipse has to be adjusted. An alternative way to direct the scattered rays is to insert a vertical groove at which the light is reflected back towards the cavity's boundary (Cai *et al.*, 2011). The effect of internal point-like defects on WGMs has been analyzed by Dettmann *et al.* (2008, 2009b) and Deych *et al.* (2011). A line defect inside the disk has been studied by Apalkov and Raikh (2004).

A perturbative approach based on the perturbation theory for deformed disks discussed in Sect. IV.D has been applied to disks with a local boundary deformation by Wiersig (2012). This approach allows the efficient and accurate calculation of frequencies, quality factors and far-field patterns.

Mode discrimination for single-mode lasing can be enhanced by considering two or three notches (Schlehahn *et al.*, 2013). The case of many notches is realized in the microgear cavity, which is a disk with Bragg grating at the circumference (Fujita and Baba, 2001, 2002).

A linear increase of the radius of a circle with the polar angle φ gives the spiral shape with a localized defect, the boundary is defined as

$$r(\varphi) = R\left(1 - \frac{\varepsilon}{2\pi}\varphi\right) \tag{41}$$

with deformation parameter $\varepsilon \geq 0$ and "radius" R at $\varphi = 0$. The radius jumps back to R at $\varphi = 2\pi$ creating a notch as shown in Fig. 24(a). Chern *et al.* (2003) have introduced the spiral-shaped cavity to demonstrate unidirectional light emission from a microdisk laser, see Fig. 24(b), which will be discussed in more detail in Sec. VII. In the spiral cavity Lee *et al.* (2004) first observed *quasi-scarred* modes, i.e. modes localized along simple geometric structures which are not supported by any periodic ray, as already mentioned in Sect. IV.C.2. One characteristic feature of the spiral cavity is the broken chiral symmetry: clockwise rotation is distinct from the counter-clockwise rotation (Chern *et al.*, 2003). This broken chirality leads to the appearance of copropagating pairs of almost-degenerate and highly nonorthogonal modes (Wiersig, 2008; Wiersig *et al.*, 2008); see also the discussion in Sec. VI.B. The notch of the spiral can be used to couple a waveguide to the cavity in a non-evanescent manner (Lee *et al.*, 2007a).

VI. MODE COUPLING

This section deals with non-Hermitian physics related to coupling between modes in open dielectric cavities due to, e.g., the change of cavity shape or introduction of external scatterers in the vicinity of the cavity boundary.

A. Avoided resonance crossings

For the convenience of the reader this section begins with a brief summary of the basic knowledge on avoided level crossings (also known as anticrossings) in closed or conservative systems. As illustrated in Fig. 25 such avoided crossings occur when the curves of two energy eigenvalues, as function of a real-valued parameter Δ, come close but then repel each other (von Neumann and Wigner, 1929). This behavior can be understood in terms of a simple toy model, a 2×2 Hamiltonian matrix

$$H = \begin{pmatrix} E_1 & V \\ W & E_2 \end{pmatrix} . \tag{42}$$

The eigenvalues and (not normalized) eigenvectors can be easily computed to be

$$E_\pm = \frac{E_1 + E_2}{2} \pm r \ , \tag{43}$$

$$\vec{\phi}_\pm = \begin{pmatrix} V \\ \frac{E_2 - E_1}{2} \pm r \end{pmatrix} \tag{44}$$

with $V \neq 0$ and

$$r = \sqrt{\frac{(E_1 - E_2)^2}{4} + VW} \ . \tag{45}$$

If the matrix H is Hermitian, describing a closed system, then the diagonal elements E_j are real and the off-diagonal elements $W = V^*$ are complex valued. Sufficiently far away from the region of resonant coupling, $|E_1 - E_2| \gg 2|V|$, the eigenvalues of the coupled system $E_\pm$ equal the energies of the uncoupled system E_j. Exactly at resonant coupling, $E_1 = E_2$, there is an energy splitting $E_+ - E_- = 2|V|$ whenever the coupling strength $|V|$ is nonzero. Around the region of resonant coupling, the eigenstates of the coupled system are hybridized, i.e. the eigenvectors of the matrix (42) are superpositions of the eigenvectors of the uncoupled system; cf. Fig. 25. Note the "exchange of identity" between the eigenstates participating in an anticrossing.

Avoided *resonance* crossings in open or dissipative systems can be described by a non-Hermitian matrix (42). The energies E_j of the uncoupled system are then complex numbers, with the imaginary part being related to the lifetime $\tau_j \propto -1/\mathrm{Im}(E_j)$ of the quasi-bound state. We focus first on the case $W = V^*$ where the *internal coupling* of states is as in a closed system but each state is individually coupled to the continuum. Exactly at resonant coupling, $\mathrm{Re}(E_1) = \mathrm{Re}(E_2)$, the number r is here either real or purely imaginary which allows for two different kinds of avoided resonance crossings (Heiss, 2000). In the weak coupling regime, $|V| < V_c$ with $V_c = |\mathrm{Im}(E_1) - \mathrm{Im}(E_2)|/2$, there is a crossing in the real part of the energy. In the strong coupling regime, $|V| > V_c$, there is an avoided crossing in the real part and a crossing in the imaginary part. These two generic cases are depicted in Fig. 26. The hybridization of modes due to the coupling can be again seen. Note that in the weak coupling regime the hybridization is weak.

The more general case $W \neq V^*$ allows *external coupling* of states via the continuum. Here, the number r can be complex with nonzero real and imaginary part which allows for a new behavior. Figure 27 shows an example in which one of the states has a significantly increased lifetime at the center of the avoided crossing. The lifetime of the other mode has decreased accordingly. In real physical systems the increased (decreased) lifetime is due to the reduction (enhancement) of a major decay channel by destructive (constructive) interference. This remarkable effect is essentially the same as "resonance trapping" where, however, the coupling strength is the parameter that is varied; see, e.g., Desouter-Lecomte and Jacquest (1995) and Persson *et al.* (1998).

In the electromagnetic setting one can consider the Hamiltonian matrix like the one in Eq. (42) as representing the linear operator describing the dynamics of electromagnetic modes in the slowly-varying envelope approximation in the time domain (Siegman, 1986). Energies are then translated to frequencies and energy eigenstates to modes.

Avoided resonance crossings with internal coupling have been experimentally demonstrated first in a microwave cavity with absorbing walls (Philipp *et al.*, 2000) and later in dielectric microcavities in the optical regime (Lee *et al.*, 2009b). The experimental verification of the external coupling type has been done first with a microwave cavity with attached waveguide (Persson *et al.*, 2000). Here, the avoided resonance crossings reduce the coupling of some modes to the waveguide thereby increasing their lifetime. In the optical domain external coupling has been experimentally demonstrated in coupled photonic-crystal defect cavities (Atlasov *et al.*, 2008), coupled microdisk cavities (Benyoucef *et al.*, 2011), and for a rolled-up microtube bottle cavity (Strelow *et al.*, 2012).

The formation of a high-quality mode in the case of external coupling is of particular relevance for optical microcavities as this may allow to tailor light-matter interaction in such devices. The enhancement of the quality factor of modes in optical microcavities has been theoretically analyzed by Boriskina (2006, 2007); Song and Cao (2010); Song *et al.* (2013a,b); Wiersig (2006); Yang and Huang (2007); Yang *et al.* (2009).

A theoretical analysis of two coupled microdisks in terms of periodic orbits in complexified phase space, see (Shudo and Ikeda, 1995, 2012), has been presented in (Shim and Wiersig, 2013). The semiclassical approach leads to an analytical formula for the frequency splitting originating from the evanescent coupling.

Another interesting aspect of mode coupling is the modification of the spatial mode pattern caused by avoided resonance crossings. In the strong coupling regime one can observe in the near-field of the cavity, beside the conventional hybridization of modes (Carmon *et al.*, 2008), a surprising phenomenon, the localization of intensity along special marginal stable periodic rays (Unterhinninghofen *et al.*, 2008; Wiersig, 2006; Yi *et al.*, 2011); see Fig. 28. Because of the resemblance to scarred states in closed systems these modes have been termed *scarlike modes*. The relation between avoided resonance crossings and scarlike modes in the dielectric ellipse finds a natural explanation in terms of an extended ray dynamics discussed in Sec. VIII.A.

Even in the weak coupling regime, in which the intracavity mode pattern is not influenced by the weak hybridization associated with the avoided crossing, the far-field pattern of one mode can be strongly modified provided that the other mode has a significant shorter lifetime. Here the small but leaky contribution to the hybridized mode dominates the far-field pattern. This effect has been utilized to weakly couple high-quality modes with isotropic light emission to low-quality modes with directional light emission. One of the hybridized modes then has kept the high Q-factor while acquired directional light emission (Wiersig and Hentschel, 2006). This scheme to achieve directional light emission from high-quality modes has been studied for several cavity geometries (Redding *et al.*, 2012b; Ryu *et al.*, 2009; Song *et al.*, 2010) which will be addressed in Sec. VII.

Moreover, avoided crossings play an important role in the distribution of resonances in the complex frequency plane (Cho *et al.*, 2011; Dettmann *et al.*, 2009a). The statistics of avoided resonance crossings in open cavities has been studied by Poli *et al.* (2009).

There is a considerable amount of literature on chains of coupled passive cavities, so called coupled resonator optical waveguides (CROWs); for a review see, e.g., Morichetti *et al.* (2012). However, non-Hermitian effects of the kind discussed here are often not explicitly studied; a commendable exception is Grgić *et al.* (2011) who investigated the impact of the imaginary part of the frequencies of the uncoupled cavities on the maximum delay time achievable in CROWs.

B. Exceptional points

A non-Hermitian eigenvalue problem does in general not have an orthogonal set of eigenvectors. In an extreme case, two eigenvectors can become even collinear. In our toy Hamiltonian this happens if the complex number r is vanishing as an inspection of Eq. (44) shows. Simultaneously, the eigenvalues in Eq. (43) become degenerated. As a result, the eigenvectors do not form a complete basis of the Hilbert space. A point in parameter space at which this happens, i.e. at which at least two eigenvectors *and* eigenvalues of a non-Hermitian matrix coalesce is called *exceptional point* (EP) (Heiss, 2000; Kato, 1966). The EP is a non-Hermitian degeneracy which must be distinguished from a diabolic point at which only eigenvalues coalesce (Berry and Wilkinson, 1984).

The EP can also be considered as the critical point where a transition from weak to strong coupling occurs. In the language of the toy model in Eq. (42) it would mean that not only Δ is varied but also another real-valued parameter, let say $|V|$, is precisely tuned to the intermediate situation between the left and right panel of Fig. 26 such that both branches of real and imaginary part of the eigenvalues touch. Varying both parameters simultaneously, the real and imaginary parts of the eigenvalues form rather complicated surfaces as illustrated in Fig. 29. Due to the square root in Eq. (45) these eigenvalue surfaces exhibit a complex-square-root topology with a branch point at the EP for two eigenvalue sheets. A consequence of this topology becomes apparent when the EP is encircled in parameter space. Continuously tracking the pair of eigenvalues reveals that both the real and the imaginary parts cross from one to the other sheet with the result that the eigenvalues swap; see black curves in Fig. 29. One has therefore to encircle the EP twice to recover the original eigenvalues. The eigenstates acquire a phase of π when the EP is encircled twice (Heiss, 1999). Hence, to recover also the original eigenstates one has to encircle the EP even four times.

The physical existence of EPs has been demonstrated by experiments on a number of physical systems as reviewed by Heiss (2012). The first direct experimental verification of the topology of eigenvalue surfaces has been done for a microwave cavity (Dembowski *et al.*, 2004, 2001). In these experiments one had full control over the eigenvalues and eigenstates which allowed also to show the recovery of the eigenstates after encircling the EP four times.

Figure 30 shows the experimental data for a liquid-jet microcavity which clearly confirms the complex-square-root topology of eigenfrequencies also in an optical microcavity (Lee *et al.*, 2009a). The EP is reached by varying a deformation parameter controlling the cavity shape and a quasicontinuous parameter labeling different mode families. Till now, it was not possible to provide experimental evidence for the expected behavior of the wave functions in an optical microcavity near an EP. A theoretical study can be found for a stadium-shaped microcavity in (Lee, 2010).

The temporal behavior of modes near an EP is discussed in detail by Heiss (2010). One experimental signature is the disappearance of Rabi-frequency beats between the two involved modes when the EP is approached. At the EP a quadratic time decay of intensity is expected. Both effects have been experimentally verified by Dietz *et al.* (2007) with a microwave billiard.

Consider a physical system which is invariant under time reversal. Representing the corresponding Hamiltonian in a basis consisting of standing waves (which are also invariant under time reversal) leads to a non-Hermitian matrix (42) with $W = V$ (but in general $W \neq V^*$). Heiss and Harney (2001) have shown that the single eigenstate of such a symmetric

Hamiltonian at the EP (Eq. (44) for $r = 0$) is given by

$$\vec{\phi} \propto \begin{pmatrix} 1 \\ \pm i \end{pmatrix} . \tag{46}$$

The sign in Eq. (46) determines the *chirality* of the EP. It depends on the system and can differ from EP to EP. This intrinsic chirality of EPs has been confirmed by Dembowski *et al.* (2003) in an experiment on microwave cavities. If time-reversal symmetry is violated then the chirality generically persists, only one of the components gathers an additional phase (Harney and Heiss, 2004). This prediction has been successfully tested for a microwave cavity perturbed by an internal ferrite (Dietz *et al.*, 2011).

The chirality of EPs plays an important role for the structure of modes in slightly deformed or perturbed microdisk cavities which lack mirror symmetries. The chirality of a given mode has here a clear physical interpretation as a preferred sense of rotation in real space. Also in the vicinity of the EP the mode exhibit an unbalanced contribution of clockwise and counter-clockwise traveling-wave components. This kind of partial chirality has been predicted by Wiersig *et al.* (2011a, 2008) and Wiersig (2011) and has been confirmed in experiments by Kim *et al.* (2014); see Fig. 31. In such cavities almost all modes appear in highly nonorthogonal pairs of copropagating modes with a preferred sense of rotation. Both features, the nonorthogonality and the chirality, can be related to the EPs. The physical origin of the chirality and the non-Hermiticity in this kind of cavities is asymmetric backscattering between counterpropagating traveling waves. In a traveling-wave basis the strong asymmetry in the backscattering can be well described by the toy Hamiltonian (42) with $|W| \ll |V|$ (or $|V| \ll |W|$). A derivation of the matrix (42) for this case can be found in (Wiersig, 2011, 2014a).

The nonorthogonality of modes in open cavities has drastic consequences for lasers. It leads to quantum excess noise and therefore to an enhancement of the laser linewidth with respect to the well-known Schawlow-Townes formula (Chong and Stone, 2012; Petermann, 1979; Pillay *et al.*, 2014; Schomerus, 2009; Schomerus *et al.*, 2000; Siegman, 1986). This is usually quantified by the Petermann factor K. At an EP the Petermann factor is expected to diverge (Berry, 2003). Lee *et al.* (2008b) have investigated this divergence with extensive numerical simulations on a stadium-shaped microcavity.

Exceptional points not only induce interesting effects in the laser operation; also the laser operation can induce EPs. This possibility has been put forward for microcavity lasers with spatially nonuniform pumping by Liertzer *et al.* (2012); see also (Ge *et al.*, 2011); and has recently been confirmed experimentally (Brandstetter *et al.*, 2014). Here, the signatures of the induced EP can be found in the above-threshold characteristics of the laser.

Like avoided resonance crossings, EPs can play a significant role in the organization of resonances in the complex frequency plane. This has been shown in theoretical works for a microdisk with a point scatterer (Dettmann *et al.*, 2009b) and a deformed microdisk (Ryu and Lee, 2011).

One potential application of EPs is in the field of label-free optical detection at single-particle resolution (Armani *et al.*, 2007; Shao *et al.*, 2013; Vollmer and Arnold, 2008; Vollmer *et al.*, 2008). Nowadays, it is possible to detect single viruses and nanoparticles by the frequency splitting of a pair of WGMs induced by near-field coupling of the particle to a microcavity. A serious problem in this scheme is the unavoidable finite frequency splitting present already in the uncoupled case due to fabrication tolerances. In an elaborate experiment, Zhu *et al.* (2010) have demonstrated that this problem can be removed by carefully placing two nano-fiber tips in the evanescent field of a microtoroid cavity. By a controlled positioning of the nano-fiber tips the cavity-tip system have been tuned to an EP at which the frequency splitting vanishes. Subsequently, it was shown by analytical and numerical calculations that the sensitivity of frequency splitting detection can be significantly enhanced at an EP (Wiersig, 2014b).

The coalescence of three eigenvalues show considerable more involved topologies of eigenvalue surfaces (Demange and Graefe, 2012). The topological structure of eigenvalue surfaces for several neighboring EPs has been studied for the case of two coupled nonidentical microdisks by Ryu *et al.* (2012); see also (Ryu *et al.*, 2009).

Finally, EPs are related to symmetry breaking in $\mathcal{PT}$-symmetric systems. Bender and Boettcher (1998) have discovered that non-Hermitian Hamiltonians which are invariant under a combination of parity ($\mathcal{P}$) and time reversal ($\mathcal{T}$) can have a real spectrum. This is the case if the eigenstates of the Hamiltonian are also symmetric under the $\mathcal{PT}$ operation. When the symmetry is broken for the eigenstates then the eigenvalues appear in complex conjugate pairs. The point in parameter space at which this symmetry breaking occurs is an EP. $\mathcal{PT}$-symmetric systems can be realized by electromagnetic systems which have a balanced arrangement of absorbing and amplifying regions (El-Ganainy *et al.*, 2007; Guo *et al.*, 2009; Rüter *et al.*, 2010). The study of electromagnetic $\mathcal{PT}$ symmetry has become a highly active field which cannot be covered in this review. In the following we therefore focus on $\mathcal{PT}$-symmetric cavities. The general scattering theory of $\mathcal{PT}$-symmetric systems has been presented by Schomerus (2010, 2013) and Chong *et al.* (2011). Schomerus (2010) revealed that quantum noise turns $\mathcal{PT}$-symmetric cavities with stationary states into self-sustained sources of radiation. The relation of quantum noise and mode nonorthogonality in $\mathcal{PT}$-symmetric cavities is theoretically analyzed by Yoo *et al.* (2011). Longhi (2010) discovered that a $\mathcal{PT}$-symmetric cavity that acts as a laser must behave simultaneously as a coherent perfect absorber; see also (Chong *et al.*, 2011). A random-matrix theory for $\mathcal{PT}$-symmetric cavities has been developed by Birchall and Schomerus (2012). An experimental realization of a $\mathcal{PT}$-symmetric cavity in the microwave and in the optical regime has been reported by (Bittner *et al.*, 2012c) and (Chang *et al.*, 2014; Peng *et al.*, 2014), respectively.

In summary, the literature reviewed in this section shows that dielectric cavities are interesting model systems for many features of non-Hermitian physics near avoided resonance crossings and exceptional points.

VII. UNIDIRECTIONAL FREE-SPACE LIGHT EMISSION FROM DEFORMED MICROLASERS

Shortly after the first fabrication of microdisks, it was shown experimentally that deforming the disk boundary from circularity allows for improved directionality of emission and therefore for more efficient extraction and collection of light (Levi *et al.*, 1993; Nöckel *et al.*, 1996). Many shapes have been proposed and realized since then, but only a few lead to light emission into approximately a single direction. Since unidirectional emission is essential to many applications such as lasers and single-photon sources, it has been the driving force behind the development of optical microcavities with various shapes over the years. Moreover, most deformed microcavities suffered severe Q-spoiling: the Q factor degrades dramatically upon deformation (Nöckel *et al.*, 1994), in the worst case ruling out any application. The trade-off between the Q factor and directionality is a critical issue for deformed microcavities. This section will provide an overview over different approaches that have been developed to obtain unidirectional emission while minimizing Q-spoiling. These works illustrate how the cavity shape can be used effectively as a "control knob" to achieve the desired performance, which is important to device applications.

A. Spiral-shaped cavity

In the early studies, the asymmetric resonant cavities retained two discrete reflection symmetry axes, and emitted multiple beams. To obtain emission in a single direction, cavities with only one symmetry axis, e.g., rounded isosceles triangle (Hentschel *et al.*, 2010; Kurdoglyan *et al.*, 2004), space capsule (Schwefel, 2004), were proposed. They, however, suffer severe Q-spoiling, making for instance the lasing threshold too high experimentally.

Another approach to unidirectional emission is to break the chiral symmetry, the prominent example is the spiral-shaped microdisk (Chern *et al.*, 2003; Kneissl *et al.*, 2004). As shown in Section V.B, the notch on the disk boundary scatters light out of the cavity; see Fig. 24. The original idea was that the counter-clockwise (CCW) propagating mode feels the notch, while the CCW one does not; thus the CCW mode has stronger outcoupling than the clockwise (CW) one, giving directional emission (Lee *et al.*, 2007a). Experimentally emission in approximately single direction was obtained by pumping optically or electrically only the edge of the cavity (Chern *et al.*, 2003; Kneissl *et al.*, 2004). Later studies showed that uniform pumping of the entire cavity does not produce directional output (Audet *et al.*, 2007; Hentschel *et al.*, 2009). Further analysis revealed that pairs of CW and CCW modes do not exist in the spiral (Wiersig, 2008; Wiersig *et al.*, 2008). Both modes in a quasi-degenerate pair are dominated by the CW component (in the orientation shown in Fig. 24). Boundary pumping enables a mode-beating mechanism that leads to directional emission (Hentschel and Kwon, 2009).

From the numerical simulations, the optimal size of the notch should be about two wavelengths, so that it is sufficiently large to break the chiral symmetry, but at the same time small enough to ensure the best possible light confinement. Nevertheless, the Q factor of the spiral cavity is greatly reduced from that of a circular cavity with the same area.

B. Interior whispering gallery modes

Next we discuss a different approach based on the construction of cavities with continuous families of periodic orbits (Baryshnikov *et al.*, 2004). Such a cavity can support invariant lines of whispering-gallery type above the critical line of total internal reflection but below the region of conventional whispering-gallery trajectories. These interior WGMs predominately emit by tunneling into the leaky region. Provided that the invariant line has a sufficient asymmetric shape in phase space, this mechanism can lead to directional or even unidirectional emission.

Figure 32 shows that this concept can indeed be used to get optical modes in a deformed microdisk which has emission mainly into a single direction. Unfortunately, the quality factor in this particular case was not reported (Baryshnikov *et al.*, 2004). For bidirectional emission theoretical (experimental) quality factors around 10^4 (6000) are reported (Gao *et al.*, 2007).

One serious problem of such a cavity for laser application is the coexistence of interior and conventional WGMs. The latter have higher quality factors as the distance from the leaky region is larger. In the case of flood (uniform) pumping, the conventional WGMs lase first due to lower threshold, producing non-directional output. Carrier injection to the cavity center selects interior WGMs for lasing because they have better spatial overlap with the gain region (Baryshnikov *et al.*, 2004). This selective pumping method, however, is difficult to implement for microcavities of dimension less than 5 μm.

Another way to suppress the lasing of conventional WGMs is to deliberately introduce surface roughness. As the conventional WGMs are located closer to the boundary of the cavity than the interior ones, the quality factor of the conventional WGMs will suffer more strongly from the Q-spoiling due to surface roughness. In this way the quality factors of the conventional WGMs can be made slightly smaller than those of the interior ones (Gao *et al.*, 2007). Obviously, this approach limits the achievable quality factors and is therefore not favorable.

C. Annular cavity

In this subsection we describe a scheme which overcomes the trade-off between quality factor and directionality by exploring mode coupling (see Section VI) as introduced by Wiersig and Hentschel (2006). The general idea is to exploit the weak coupling scenario to slightly hybridize a high-Q mode (HQM) and a directional low-Q mode (LQM) to a mode with high quality factor and the directed far-field pattern of the LQM. This scheme can be realized in three steps. First, take a cavity with HQMs, e.g., a microdisk. Second, introduce a one-parameter family of perturbations such that at least one HQM is almost unaffected and at least one HQM turns into a LQM having directed emission via refractive escape. Third, vary the parameter such that an avoided resonance crossing occurs between the HQM and the LQM. This scheme allows the systematic design of modes with high quality factors and highly directed emission.

This scheme has been demonstrated first by a theoretical study of an annular cavity, a GaAs microdisk with a circular air hole (Wiersig and Hentschel, 2006). Figure 33 shows for this system an avoided resonance crossing in the weak coupling regime, i.e. the frequencies cross and the quality factors repel each other. Both modes involved in this avoided crossing have even parity with respect to the symmetry axis. One mode has a high Q-value above $5 \cdot 10^5$, the other one has a low Q-value of ≈ 300 and unidirectional emission due to light reflection at the air hole. The hybridization is weak, which keeps the quality factors and the near-field patterns almost unaffected while the far-field pattern is in both cases dominated by the low-Q component; cf. the solid and dashed lines in the lower right panel of Fig. 33. As a result a high-Q mode with unidirectional emission is obtained. This theoretical prediction has been confirmed in an experiment (Wilde, 2008). Recently, another experiment on an annular cavity coupled to a waveguide showed unidirectional emission as well (Preu *et al.*, 2013).

The problem of this particular system is the coexistence of even and odd symmetry modes. Since the scenario of avoided resonance crossings is in general different for the two symmetry classes, the respective output directionality may differ. In most of the practical cases both modes are involved in the process of light emission which then spoils the directionality. To avoid this problem of the mode coupling approach a less symmetric geometry is needed, which will be discussed in VIII.B.

D. Limaçon cavity

This subsection introduces a robust and general mechanism that combines directional light output and ultralow loss in deformed microdisks (Wiersig and Hentschel, 2008). The key idea is to exploit light emission along unstable manifolds of the chaotic saddle of the ray dynamics (see Sec. IV.C) to achieve unidirectional emission and to use wave localization such as scarring (see again Sec. IV.C) to get high Q-factors. When the cavity size is much larger than the wavelength, the output directionality is universal for all the high-Q modes because the corresponding escape routes of rays are similar. This property enables one to robustly achieve unidirectional emission without selective excitation of specific modes in experiments.

The applicability of this idea was demonstrated for the limaçon cavity defined as in Eq. (23). In Fig. 34(a), ray simulations of far-field intensity patterns from the limaçon cavity with refractive index $n = 3.3$ and deformation parameter $\varepsilon = 0.43$ are plotted for the TE polarization (solid curve) and TM polarization (dashed curve). The far-field pattern is determined by the unstable manifold in the leaky region ($|\sin\chi| < 1/n$), which can be computed from the survival probability distribution for an ensemble of rays starting uniformly in phase space with identical intensity. Figure 34(b) depicts the resulting Fresnel weighted unstable manifold of the chaotic saddle for the limaçon cavity, revealing the manifold is concentrated on very few high-intensity spots in the leaky region. Therefore, the escape routes of rays, regardless the starting points, are closely nested in the phase space, leading to highly directional output. Due to the existence of the Brewster angle for the TE polarization, the unidirectionality is better in the TE case than in the TM case (Wiersig and Hentschel, 2008).

Numerical solution to the wave equations confirmed that the limaçon cavity supports high-Q modes of both TE and TM polarization. As an example, Fig. 35 shows a TE mode of $Q = 185,000$ at the normalized frequency $\Omega = \omega R/c = 26.0933$, which corresponds to, e.g., a free-space wavelength of about 900 nm for $R = 3.75\,\mu$m. The mode is spatially confined near the boundary of the cavity. The Husimi function shows the mode intensity is enhanced around an unstable periodic ray trajectory, which is located well above the critical line for total internal reflection ($|\sin\chi| = 1/n$). Hence, the scarring phenomenon results in exponentially small intensity in the leaky region that gives the high Q factor.

Even though the Husimi function has a small contribution in the leaky region, it is precisely this outgoing light that determines the far-field pattern. Figure 35 shows that the Husimi function in the leaky region agrees to the unstable manifold in Fig. 34, confirming its responsibility for the directional emission. Owing to the ray-wave correspondence (Shinohara and Harayama, 2007), all high-Q modes exhibit unidirectional emission patterns closely corresponding to the ray calculation.

Soon after the theoretical proposal by Wiersig and Hentschel (2008), several groups fabricated limaçon cavity lasers (Albert *et al.*, 2012; Shinohara *et al.*, 2009; Song *et al.*, 2009b;

Yan *et al.*, 2009; Yi *et al.*, 2009). Song *et al.* (2009b) studied GaAs limaçon cavities with $R = 2.18\,\mu$m (dimensionless size parameter $n\omega R/c \approx 48$) and measured a Q factor of 22,000, significantly higher than all the previously reported Q values of deformed microcavities. The high-quality factor and small modal volume results in very low lasing threshold, allowing continuous wave operation. The inhomogeneously broadened gain spectrum of InAs quantum dots leads to lasing in multiple modes well separated in wavelength. All the lasing modes have single output beam in the same direction, regardless of their wavelengths and intracavity mode structures. The unidirectionality is robust against cavity sidewall roughness and small shape deviation, allowing fabrication by standard photolithography and wet chemical etching. Shinohara *et al.* (2009) investigated larger GaAs cavities with $R = 20$ to $50\,\mu m$ ($n\omega R/c \approx 480$ to 1200) and obtained lasing by electric pumping with pulsed currents. Yi *et al.* (2009) also achieved lasing in the InGaAsP cavities with $R = 50\,\mu$m ($n\omega R/c \approx 650$) by electric pumping with continuous currents. In all of these studies, measured light emissions were TE-polarized and unidirectional emissions corresponding to the ray simulations were confirmed. TM-polarized unidirectional emission was confirmed by Yan *et al.* (2009) for quantum cascade lasers with the limaçon cavities of $R = 80\,\mu$m ($n\omega R/c \approx 161$), where again close agreement with the ray simulations was reported. In addition to dielectric disks, vertical cavities with limaçon cross section were fabricated, and directional far-field emission was demonstrated from electrically driven quantum dot micropillar lasers (Albert *et al.*, 2012).

For the GaAs-based microcavities described above, the refractive index is around 3.3 and the optimal deformation for unidirectional emission is $\varepsilon = 0.43$. Numerically highly directional far-field pattern and high quality factor were also found for $0.41 \leq \varepsilon \leq 0.49$, and the refractive index between 2.7 and 3.9 (Wiersig and Hentschel, 2008).

E. "Face" cavity

Since the unidirectional emission of limaçon-shaped cavities is valid only for high-refractive-index materials ($n \geq 2.7$), the remaining question is how to obtain high Q and unidirectional emission from low-refractive-index microcavities, such as silica ($n = 1.45$). Experimentally silica microspheres can have much higher Q than GaAs microdisks, and slight deformations of spheres are shown to make the output directional, but not in a single direction (Lacey and Wang, 2001; Xiao *et al.*, 2007, 2009).

Recently, Zou *et al.* (2013) came up with a guideline for the design of low-refractive-index microcavities with high Q-factor and unidirectional emission. First, the cavity deformation must be small, continuous and smooth in order to support high-Q WGMs. Second, the boundary shape should have no more than one axis of symmetry. For planar deformed cavities, two or more lines of symmetry or m-fold rotational symmetry with $m > 1$ will lead to at least two emission directions in far field. According to the aforementioned guidelines, the cavity boundary can be expressed in a general form

$$r(\varphi) = \begin{cases} R(1 - \varepsilon \sum_i a_i \cos^i \varphi), & -\pi/2 < \varphi \leq \pi/2 \\ R(1 - \varepsilon \sum_i b_i \cos^i \varphi), & \pi/2 < \varphi \leq 3\pi/2 \end{cases} \tag{47}$$

where φ is the polar angle, ε is the general deformation, a_i and b_i are coefficients with $i \geq 2$. With small and continuous deformation, the cavity is in the regime of 'mixed phase space' or 'soft chaos', namely, the phase space has a combination of chaotic and regular regions. The high-Q WGMs stay well above the critical line for total internal reflection; through dynamical tunneling light escapes to the chaotic sea and diffuses to the leaky region ($|\sin\chi| < 1/n$) along unstable manifolds. The relative positions of unstable periodic orbits and regular islands for stable periodic orbits determine the shapes of manifolds and the regions on the boundary where rays refract out (called 'refraction regions'). Thus the positions of the refraction regions can be tuned by changing the cavity shape via ε, a_i and b_i.

Zou *et al.* found the cavity of highest unidirectionality in an ensemble of 1000 cavity shapes, with the parameters $\varepsilon = 1.0$, $a_2 = 0.2491$, $a_3 = -0.0520$, $a_4 = -0.0783$, $b_2 = 0.2538$, $b_3 = 0.0446$, and $b_4 = -0.0214$. The refractive index of the cavity is $n = 1.45$. As shown in Fig. 36(a)-(b), the islands for stable rectangle period-4 orbit in the SOS shape the unstable manifolds, making the far-field pattern highly unidirectional [Fig. 36(c)]. Because its SOS assembles a monster face, this cavity is called the "Face" cavity (Zou *et al.*, 2013).

While the results of the ray simulations are impressive, there are problems with respect to the mode properties. Since the approach is based on a mixed phase space, there exist modes located in regular islands which, at least partly, leave the cavity by directed tunneling. Such modes have high Q but cannot entirely follow the unstable manifold in the desired direction. The same is true for modes confined by partial barriers which play an important rule in mixed phase space. This mechanism becomes dominant for low to moderately low

kR (Shim *et al.*, 2011). It is therefore to be expected that Zou *et al.*'s approach does not provide universal far-field patterns already for moderately small cavities.

Recently, shapes of the type in Eq. (47) have been realized experimentally with microdisks (Liu *et al.*, 2013), microtoroids (Jiang *et al.*, 2012), and microspheres (Cui *et al.*, 2013). In the first case Liu *et al.* (2013) fabricated polymer ($n = 1.503$) microcavities by two-photon polymerization. In the second case Jiang *et al.* (2012) fabricated doped silica microtoroids. In the third case, the equator of a silica microsphere is deformed by shooting CO_2 laser pulses to one side of the microsphere. The deformation can be well controlled by adjusting the intensity and the number of heating laser pulses. Using this method, directional emission from WGMs with high quality factor of 10^7 is achieved in these microspheres, and a transition from two-directional to single-directional emission is observed for the special case of a traveling wave excitation using a fiber taper (Cui *et al.*, 2013).

F. Ellipse with a notch

Although the unstable manifolds can produce emission predominantly in a single direction, the far-field divergence angle of the main lobe is relatively large, and side lobes persist. To obtain an output beam with small divergence angle, Wang *et al.* (2010) took a different approach. Instead of utilizing the unstable manifold, they introduced a defect at the cavity boundary to scatter light, most of which was then focused by the cavity boundary to a collimated beam.

Figure 37(a) shows light scattered by a wavelength-size notch at the edge of an elliptical cavity, then collimated as a parallel beam in the far field by the right boundary of the notched ellipse. To achieve optimal collimation, Wang *et al.* utilized the well-known focusing property of the ellipse (auxiliary ellipse in dashed line): for any given refractive index $n > 1$, one can find an auxiliary ellipse such that all incoming parallel rays are collected into one of its foci; conversely in the reciprocal process light emerging from the left focus of the auxiliary ellipse in Fig. 37(a) is refracted by its right half-side into parallel rays. Note that the notch is located at one of the foci of the auxiliary ellipse, but not at the focus of the elliptical cavity. The long-to-short aspect ratio of the elliptical cavity is chosen such that its right-side boundary best (i.e., over the largest possible angle) approximates that of the auxiliary ellipse. Figure 37(b) presents the ray simulation of the collimation effect: a number of rays are started at the position of the notch with different outgoing angles, simulating a scattering process. They travel inside the cavity until they hit its boundary, upon which they either are specularly reflected or, if the angle of incidence at the surface is smaller than the critical angle for total internal reflection, get refracted out. The solid rays, which leave the notch under relatively smaller outgoing angles, get collimated; the collimation is worse for higher outgoing angles (outermost rays). The dash-dotted ray leaves the notch at a high outgoing angle and is relaunched into a WGM. Figure 37(c) shows the ray simulation of whispering-gallery dynamics. A single ray is started at some position along the resonator boundary with an initial condition such that the angle of incidence is larger than the critical angle. It is then specularly reflected many times, corresponding to a whispering-gallery-like mode, until at some point it hits the notch. It then gets reflected to the opposite boundary, and refracted out, leaving the cavity parallel to the horizontal axis due to the collimation effect.

Experimentally the notched-elliptical cavities were fabricated for the quantum cascade laser operating at the free-space wavelength of $10\,\mu$m (Wang *et al.*, 2010); see Fig. 37(d). The long axis and short axis were $96\,\mu$m and $80\,\mu$m, respectively. The optimized notch width was $3\,\mu$m and depth $2\,\mu$m. Wave simulation of a first-order WGM with TM polarization and refractive index $n = 3.2$ gave a Q factor of 590,000. According to the calculated intracavity intensity distribution, only the outermost part of the mode had an overlap with the notch, which explained the high Q factor. The laser output was highly unidirectional, with FWHM (full-width-at-half-maximum) beam divergence angle of merely 6 degree as shown in Fig. 37(e)

For a refractive index below 3 the emission starts to become more uniform. This is due to the fact that for a low index, most of the rays hitting the notch are partially transmitted, and thus much of the intensity is not reflected to the opposite side where collimation can take place (Unterhinninghofen, 2011).

Recently, the collimation effect has been exploited in numerical simulations by coupling a microdisk to a lens-shaped cavity nearby (Ryu and Hentschel, 2011). By a proper choice of parameters unidirectional light emission from high-quality modes is possible even in the low-index regime.

VIII. BEAMS SHIFTS AND SEMICLASSICAL APPROACHES

In this section we discuss beam shifts and semiclassical approaches which are in particular relevant for wavelength-scale microcavities. As will be explained later, the wavelength-scale cavities are important not only for practical applications, but also for fundamental studies on the ray-wave transition in non-Hermitian systems.

A. Beam shifts

As discussed in Sec. IV, certain modes in microdisk cavities possess a simple geometric structure, for instance a Gaussian mode based on a stable periodic orbit (Fig. 15), a scarred mode along an unstable periodic orbit (Fig. 21), or a quasiscarred mode without underlying periodic orbit. In such a case, it is convenient to describe the mode by a single optical beam propagating periodically inside the cavity. It is well-known that when a beam of finite angular spread is incident to a dielectric interface, the reflected and the transmitted beams both undergo spatial and angular shifts. In general, four different kinds of beam shifts can occur, see the recent review (Bliokh and Aiello, 2013), but only the two shifts that are in the plane of incidence are relevant for the quasi-two-dimensional geometry of a (deformed) microdisk cavity. In the geometric optics limit $\lambda \to 0$, the beam shifts disappear and the center of the beam follows the prediction of geometric optics. For finite wavelength λ, however, the effective beam center dynamics including beam shifts deviate from the prediction of geometric optics. In this sense, the beam shifts can be considered as a semiclassical correction to the ray dynamics (Chowdhury *et al.*, 1994; Hentschel, 2001; Hentschel and Schomerus, 2002; Herb *et al.*, 1999).

The beam shift that was discovered first is the *spatial Goos-Hänchen shift* (GHS) (Goos and Hänchen, 1947). Upon reflection of a beam at a dielectric interface near or above the critical angle of incidence for total internal reflection χ_c, the different partial waves in such a beam accumulate different phases, which leads to a lateral shift Δs along the interface due to interference; see Fig. 38(a). The GHS Δs is proportional to the wavelength λ. At a planar interface between two normal dielectrics Δs is positive, but it can be negative for an interface between a normal dielectric and a negative-index metamaterial; see, e.g., (Berman, 2002; Wiersig *et al.*, 2010). A simple analytical formula for $\Delta s(\chi)$ at a planar interface above the critical angle, $\chi > \chi_c$, is due to Artmann (1948). Right at the critical angle the formula exhibits an unphysical singularity. The same is true at $\sin\chi = 1$. For Gaussian beams, there is an analytical result due to Lai *et al.* (1986), which is valid if the beam width σ is much larger than $1/k$, where k is the wave number. In the regime of $k\sigma \approx 1$, the Lai result also shows unphysical singularities (Unterhinninghofen and Wiersig, 2010). Measurements of the GHS in the microwave regime have been done by Müller *et al.* (2006) and Unterhinninghofen *et al.* (2011).

While the GHS is related to the χ-dependence of the phase of the complex reflectivity r, the other beam shift relevant for microdisk cavities is associated with the χ-dependence of the absolute value of r. In this case, partial waves with angles of incidence χ below the critical angle χ_c are (partially) refracted out of the cavity, leading to an angular shift $\Delta\chi$ (or Δp, if one considers the dimensionless momenta $p = \sin\chi$ of the partial waves) of the reflected beam – a violation of the law of reflection – and an angular shift $\Delta\eta$ of the transmitted beam – a violation of Snell's law; see Fig. 38(b). For the case of reflection the beam shift is called *angular Goos-Hänchen shift* (Chan and Tamir, 1985; Ra *et al.*, 1973) and for the case of transmission *Fresnel filtering* (FF) (Tureci and Stone, 2002). There are subtle differences in the precise definition of FF and angular Goos-Hänchen shift which are of no relevance for the discussion here; see (Götte *et al.*, 2013) for a comprehensive comparison. In the following we use the term FF effect both for the reflected and the transmitted beam. The FF effect in transmission has been observed experimentally in the far-field pattern of a scarred optical mode in a GaN microlaser with quadrupolar shape (Rex *et al.*, 2002) and of a Gaussian optical mode in a quasi-stadium GaAs/AlGaAs microlaser (Shinohara *et al.*, 2011a). The FF effect in reflection has been measured in the microwave regime (Müller *et al.*, 2006) and in the optical regime (Merano *et al.*, 2009).

Studies of beam shifts at *curved* interfaces have also been done; see, e.g., (Hentschel and Schomerus, 2002; Schomerus and Hentschel, 2006; Tran *et al.*, 1995; Zhou *et al.*, 2011).

As both beam shifts, GHS and FF, are associated to the χ-dependence of the reflectivity r they can be considered as two aspects of a unique beam-propagation phenomenon (Aiello *et al.*, 2009) which becomes obvious in the mode representation using the Husimi function in the SOS (Schomerus and Hentschel, 2006).

Extending the ray dynamics by incorporating the GHS preserves the Hamiltonian character of the dynamical system (Altmann *et al.*, 2008; Unterhinninghofen *et al.*, 2008) whereas the FF effect leads to non-Hamiltonian features as will be discussed below. A number of interesting effects on the phase space and the mode properties have been discovered. For instance, the GHS increases the round-trip optical path and thereby modifies the mode spacing. This has been demonstrated by Mie theory calculations for dielectric spheres (Chowdhury *et al.*, 1994).

Foster *et al.* (2007) were the first to show that the GHS can modify the structure of phase space not only quantitatively but also qualitatively and can therefore lead to new types of mode patterns. In their dome-shaped cavity the GHS creates in phase space a stable periodic orbit surrounded by a small island. Following the semiclassical eigenfunction hypothesis (Berry, 1977; Percival, 1973) the island can support modes which have been indeed observed in the dome cavity by numerical calculations. Unterhinninghofen *et al.* (2008) have confirmed this GHS-induced localization for modes in the dielectric ellipse; see Fig. 39. Moreover, they have shown that the GHS applied to integrable ray dynamics cannot only create stable periodic orbits but also unstable ones in accordance with the Poincaré-Birkhoff theorem (Lichtenberg and Lieberman, 1992; Ott, 1993). The existence of scarred modes localized along such unstable periodic orbits has been confirmed in numerical simulations (Unterhinninghofen *et al.*, 2008) and experiments (Yi *et al.*, 2011) on the dielectric ellipse. If the GHS is sufficiently small, the created stable and unstable periodic orbits are spatially close to the corresponding geometric-optics orbits; cf. Fig. 39 and Fig. 28(c). Hence, the discussed modes are also localized near these special marginal stable periodic orbits. Because of this, these modes have been originally termed *scarlike modes* as discussed in Sec. VI. The scarlike modes in the ellipse appear together with avoided resonance crossings (see Fig. 28) since the GHS breaks the integrability of the internal ray dynamics in this kind of cavity (Unterhinninghofen *et al.*, 2008).

The dynamical interplay of GHS (calculated for a planar interface) and boundary curvature of a deformed disk leads to shifts of phase-space structures in momentum direction (Unterhinninghofen and Wiersig, 2010), which had been misinterpreted as FF effect before (Lee *et al.*, 2005). Using the local radius of curvature ρ, one finds the periodic-orbit shift

$$\Delta p_{\mathrm{POS}} = \frac{\Delta s}{2\rho} \cos\chi. \tag{48}$$

Numerical calculations confirm that the modes localize along the shifted periodic orbits rather than along the periodic orbits of the conventional ray dynamics. The periodic-orbit shift (48) has turned out to be important for a quantitative understanding of resonance-assisted tunneling in deformed microcavities (Kwak *et al.*, 2013). The extended ray dynamics with GHS calculated for a curved interface has been studied in (Kotik and Hentschel, 2013).

While the GHS is a Hamiltonian correction, the FF renders the extended ray dynamics non-Hamiltonian (Altmann *et al.*, 2008). This can have dramatic consequences on the long-time dynamics shown in phase space portraits since attractors and repellers may replace KAM invariant curves, regular islands, and chaotic regions (Altmann *et al.*, 2008; Arroyo *et al.*, 2009; Unterhinninghofen and Wiersig, 2010).

The ray dynamics augmented by FF explicitly takes the openness of the system into account. Because of this the extended ray dynamics violates time-reversal symmetry (Altmann *et al.*, 2008). One consequence is that time-reversal periodic orbit partners of the conventional ray dynamics are distorted differently by the FF and therefore split (Altmann *et al.*, 2008; Redding *et al.*, 2012b; Shim *et al.*, 2012; Song *et al.*, 2011).

The quasiscars (modes localized on simple geometric structures without underlying geometric-optics rays; see Sec. IV) observed in spiral-shaped microcavities (Lee *et al.*, 2004) can be understood as real scars localized along unstable periodic orbits in a ray dynamics augmented by FF (Altmann *et al.*, 2008).

B. Wavelength-scale microcavities

In recent years there has been a strong push towards further reduction of microlaser size for applications to nanophotonic circuits, on-chip optical interconnects, very local chemical and biological sensing. The typical microdisk lasers have diameter over 1 μm to avoid high optical bending losses inside dielectric disks (Baba, 1997). In 2007 Zhang *et al.* realized submicron disk lasers which operated at room temperature and emitted in the visible regime (Zhang *et al.*, 2007b). The smallest disks for which they achieved lasing operation have a diameter of 645 nm, which is equal to the lasing wavelength in vacuum. In 2009 Song *et al.* reported single-mode lasing in subwavelength GaAs disks at near-IR frequency (Song *et al.*, 2009a). The smallest disk diameter, about twice of the wavelength inside the disk, is 30% less than the emission wavelength in free space. These submicron disks, fabricated by standard photolithography and wet chemical etching, had good circularity, smooth boundary, and vertical sidewalls, which facilitated lasing in whispering-gallery modes of the azimuthal number as small as 4. The rotational symmetry of the circular microdisk, however, results in an uniform far-field emission pattern, which is a considerable disadvantage for most applications. In order to obtain directional emission, wavelength-scale deformed microcavities were investigated subsequently.

As elaborated in previous sections, directional output from cavities of size much larger than the optical wavelength ($kR \gg 1$) has been obtained by manipulating the intracavity ray dynamics via deliberate deformation of the cavity shape. As the wavelength approaches the cavity size, the classical ray model breaks down, and wave phenomena become significant. High-Q modes (HQMs) may be formed by partial barriers in phase space (Shim *et al.*, 2011), and their emission to free space is not as directional as from larger cavities. Moreover, the output directionality is no longer universal, it varies from mode to mode, in contrast to the prediction of the ray model. Nevertheless, unidirectional emission can still be generated from such small cavities by coupling an isotropic HQM to an anisotropic low-Q mode (LQM) (Song *et al.*, 2010, 2011). As an example, let us consider a cavity of shape similar to the limaçon cavity discussed in Section VII.D. The intracavity ray dynamics is predominantly chaotic, the escape of rays is dictated by the unstable manifolds which gives unidirectional emission. Experimentally, both unidirectional and bidirectional emission were observed for different lasing modes in the size regime $5 < kR < 10$. Wave simulations revealed that in this regime there are a set of HQMs and a set of LQMs with different mode spacing [Fig. 40(a)]. At $kR \simeq 7$, the particular pair of modes, one from each set, are nearly degenerate in frequency and become coupled. The coupling results in a drop in the Q of the HQM and an increase of its emission directionality

$$U = \int f(\varphi) \cos\varphi \, d\varphi \ , \tag{49}$$

(with the far-field intensity pattern $f(\varphi)$ normalized to unity) as shown in Fig. 40. Comparison of the intensity distributions of the HQM and LQM at frequencies away from the coupling region and near the coupling point reveals a hybridization of the HQM and the LQM at the coupling point. Such hybridization makes the HQM possess the directed far-field pattern of the LQM, which is the same as the mechanism discussed in Section VII.C for the annular cavity.

The directional emission of the LQM is attributed to the beam shifts (see Section VIII.A) in the wavelength-scale cavity. The Husimi function on the classical Poincaré SOS reveals that the LQM is concentrated on a periodic orbit of triangle shape with three bounces from the cavity boundary. The beam shifts, i.e., the GHS and the FF, are evident in the incident and emergent Husimi functions (Song *et al.*, 2010, 2011). Consequently, the triangle orbit is broken into two distinct CW and CCW periodic pseudo-orbits. This split is confirmed by direct calculation of periodic orbits with the extended ray dynamics that incorporates the beam shifts (Song *et al.*, 2011). Figure 41 plots the CW and CCW orbits of period 3 that correspond to the LQM. In the case of CCW (CW) motion the angle of incidence is smallest at bounce point iii (i) leading to the strongest emission there. In both cases the emitted rays emanate in the same direction leading to a unidirectional output.

The beam shifts, which are significant for the LQM and makes its emission directional, are negligible for the HQM, which is concentrated on a period-4 orbit with larger angle of incidence (Song *et al.*, 2010, 2011). Hence, directional output for a HQM can only be obtained by accidental coupling to a LQM. However, with a further reduction of the cavity size, the underlying orbits for the HQMs have decreasing number of bounces and the angles of incidence approach the critical angle for total internal reflection. Let us again take the limaçon cavity as an example. In the regime of $2 < kR < 5$, the HQMs correspond to triangle orbits with angle of incidence near the critical angle; consequently, the beam shifts (FF and GHS) become much stronger, making the HQM directional without coupling to a LQM. Figure 42(a,b) shows the constitute CW and CCW waves in a directional HQM of $kR = 3.2$. The CW wave has enhanced amplitude at three locations on the cavity boundary, which are close to but not coincident with the bounce points of a triangle orbit predicted by ray optics. A similar phenomenon is seen for the CCW wave, with enhanced intensity at different locations. These locations agree well with the positions of the bounces from the Husimi function of the HQM. The spatial separation of the CW and CCW intensity maxima results from the beam shifts, which produces directional output, as shown in Fig. 42(c,d). Experimentally lasing was realized in the HQM of kR down to 3, and unidirectional emission was observed (Song *et al.*, 2010, 2011).

The spatial separation of the intensity maxima for the CW and CCW waves introduces local chirality, defined as $W(\theta) \equiv [I_{CCW}(\theta) - I_{CW}(\theta)]/[I_{CCW}(\theta) + I_{CW}(\theta)]$, where θ specifies the angle along the cavity boundary (Redding *et al.*, 2012b). Despite that the cavity shape possesses chiral symmetry $r(-\varphi) = r(\varphi)$, the local balance between the intensities of CW and CCW waves is broken by GHS and FF, namely, $I_{CW}(\theta) \neq I_{CCW}(\theta)$ at the cavity boundary. By placing a waveguide tangentially to the cavity boundary, either CW and

CCW wave is selectively coupled out, depending on the coupling position, thus making the evanescent waveguide coupling directional (Redding *et al.*, 2012a,b). Figure 43 shows a straight waveguide with the same refractive index as the deformed disk placed in the near field of the disk boundary, and the location of the coupling point is specified by the angle θ. At each θ, J_{CW} (J_{CCW}) represents the intensity of emission from a cavity resonance to the waveguide in the CW (CCW) direction. Quantitatively, the directionality of the coupled emission, defined as $V(\theta) \equiv [J_{CCW}(\theta) - J_{CW}(\theta)]/[J_{CCW}(\theta) + J_{CW}(\theta)]$, was plotted as a function of the coupling position θ in Fig. 43(b). As the coupling point moves along the cavity boundary, the sign of $V(\theta)$ changes, reflecting the switch of the outcoupling direction. The variation of $V(\theta)$ mirrors that of the local chirality $W(\theta)$ in Fig. 43(d), confirming that the directional coupling originates from local chirality. Experimentally local chirality and directional coupling to a waveguide have been demonstrated with wavelength-scale semiconductor lasers (Redding *et al.*, 2012a,b).

Selective coupling of CW (CCW) wave reduces its amplitude inside the cavity, making CCW (CW) wave dominant. In other words, with this selective coupling scheme, the cavity resonance is composed mainly of the less coupled CCW (CW) wave. The standing wave pattern is thus replaced by a propagating wave, which produces a more uniform spatial distribution of the field intensity inside the cavity (Redding *et al.*, 2012a). In the application to laser, the spatial hole burning effect is reduced, and the lasing mode can utilize the optical gain at the field nodes of a standing wave pattern. This effect is most significant in gain materials with limited carrier mobility, such as quantum dots.

C. Semiclassical approaches

An important tool of the semiclassical description of multidimensional wave and quantum systems are trace formulas (Balian and Bloch, 1970, 1971, 1972; Berry and Tabor, 1976; Gutzwiller, 1971, 1990). Such a formula relates the density of states (DOS) to the sum of a smooth part given by a series of Weyl terms and an oscillating part given in the leading order by a sum over classical periodic orbits.

Bogomolny *et al.* (2008) extended this concept to open dielectric cavities by using the Krein formula. Their result can be written in the form

$$\frac{1}{\pi}\sum_m \frac{-\operatorname{Im} k_m}{(k-\operatorname{Re} k_m)^2+(\operatorname{Im} k_m)^2} = \bar{d}(k) + d^{(\mathrm{osc})}(k) \ , \tag{50}$$

with real wave number $k = \omega/c$. On the left-hand side is the excess DOS which is a sum over Lorentzian terms for all internal modes (Feshbach resonances) with complex k_m. On the right hand side is the semiclassical approximation of the DOS consisting of a smooth part $\bar{d}(k)$ and an oscillating part $d^{(\mathrm{osc})}(k)$. Note that in contrast to (Bogomolny *et al.*, 2008) we use the DOS $d(k) = dN/dk$ instead of $d(E) = dN/dE = d(k)/2k$ with $E = k^2$. The two leading terms of the smooth part are

$$\bar{d}(k) = \frac{An^2}{2\pi}k + \tilde{r}(n)\frac{L}{4\pi} \ , \tag{51}$$

where A and L are the area and the perimeter of the cavity. The prefactor $\tilde{r}(n)$ depends on the refractive index n and on the polarization. Explicit expressions for TM and TE polarization can be found in (Bogomolny *et al.*, 2008) and (Bogomolny and Dubertrand, 2012), respectively. Note that the smooth part in Eq. (51) is not in contradiction with the fractal Weyl law discussed in Sec. IV as the latter considers only a part of the internal modes with small $|\operatorname{Im} k_m|$.

The oscillating part of the DOS is a sum taken over all periodic ray trajectories inside the cavity,

$$d^{(\mathrm{osc})}(k) = \sum_p \left(c_p e^{inkl_p} + c.c.\right) \ . \tag{52}$$

l_p is the length of the periodic ray trajectory. The coefficient c_p can be calculated from the properties of the considered ray trajectory. c_p differs from the closed billiard case only by a product over Fresnel reflection coefficients (TM or TE) computed at all reflection points of the given trajectory.

The comparison of measurements, numerical calculations, and trace formula can be most conveniently done by a Fourier transformation of the DOS with respect to the wave number k. According to Eq. (52) the resulting *length spectrum* is peaked at the lengths of the periodic ray trajectories. An example is shown in Fig. 44.

The trace formula (50)-(52) has been derived for the integrable circular cavity but there is numerical and experimental evidence that the formula applies also to other geometries.

Bogomolny *et al.* (2011) confirmed the validity of the trace formula for the square, rectangle, ellipse, pentagon, and stadium in numerical simulations and in experiments on organic microlasers (such as in Fig. 11(a)). Good qualitative agreement between the trace formula and microwave experiments on dielectric resonators of circular, square, and stadium shape has been reported by Bittner *et al.* (2010, 2012a,b). However, the authors emphasized the need of higher-order corrections of the trace formula and showed that the application of curvature corrections to the Fresnel reflection coefficients improves the agreement (Bittner *et al.*, 2012b). Bogomolny *et al.* (2008) have shown that higher-order corrections lead to a small shift of the peak positions in the length spectrum which can be interpreted as an analogue to the Goos-Hänchen shift.

Hales *et al.* (2011) extended the trace formula to the case of a dielectric disk with a point scatterer. In this nonintegrable system, additional contributions appear stemming from diffractive ray trajectories, which are closed trajectories that begin and end at the scatterer. Good agreement with full numerical calculations was obtained.

A superficially similar approach is the periodic-orbit-sum formula introduced by Fukushima *et al.* (2006) for the decay rate of modes $\Gamma = -\mathrm{Im}\,\omega$ in an elongated quasistadium laser diode. It is based on a semiclassical approximation to the extended Fox-Lie mode calculation method.

A very different semiclassical approach is the one developed by Narimanov *et al.* (1999) for the decay rate Γ and far-field intensity pattern $f(\varphi)$ of isolated resonances. These quantities are expressed in terms of eigenstates of a related closed billiard, which incorporates the effect of a refractive index in the boundary conditions. In a semiclassical approximation this allows to represent Γ and $f(\varphi)$ as sums over the contribution of ray trajectories which escape the cavity by refraction (evanescent escape is ignored). This approach can be considered as a first-order perturbation theory in Γ. It is not perturbative in the degree of deformation. The original formulation by Narimanov *et al.* (1999) suffers from spurious solutions that correspond to bound states satisfying Neumann boundary conditions at the boundary. A subsequent formulation by Hackenbroich (2001) avoids any spurious solution. Because of the requirement that the eigenstates of the closed billiard have to be known beforehand, this semiclassical approach seems to be only practical for Gaussian modes based on stable periodic orbits (Sec. IV, Fig. 15) computed in the parabolic equation approximation (Tureci *et al.*, 2002). For this particular case, a full analytic semiclassical solution can be found.

IX. ROTATING MICROCAVITIES

The previous sections describe stationary microcavities. In this section, we will consider microcavities that rotate. Light propagation in rotating macrocavities has been studied as one of the most fundamental problems of electromagnetics in arbitrary accelerated systems (Chow *et al.*, 1985; Post, 1967). Of particular interest is the rotating ring cavity, due to its application to the optical gyroscope. Since the cavity size is typically much larger than the wavelength, the ray dynamical description has been widely used. What happens in a microcavity of size comparable to the wavelength? How will the rotation modify the cavity resonances? Answering these questions is important not only in terms of the fundamental physics but also for the realization of ultrasmall optical gyroscopes.

A. Sagnac effect in microcavities

In 1913 Sagnac pointed out that the path length of clockwise (CW) propagating light in a rotating ring interferometer for one round trip is different from that of counterclockwise (CCW) propagating light; the resulting phase difference was later used to detect the rotation speed (Chow *et al.*, 1985; Post, 1967). In a ring cavity, the round-trip path-length difference for the CW and CCW waves lift the degeneracy of resonances; the frequency splitting has become the operation principle for ring laser gyroscope.

In 2006 Harayama and coworkers studied Sagnac effect in 2D microcavities of various shape (Sunada and Harayama, 2006). The microcavity rotates around a fixed axis (z-axis) perpendicular to the cavity plane (xy-plane). The rotation angular velocity Ω is assumed to be constant in time, and the maximal speed $v = \Omega R$ to be small in magnitude compared to the speed of light. In the reference frame rotating with the cavity, the Maxwell's equations retain their forms in the inertial frame, but the constitutive relations are modified (Shiozawa, 1973). Like in an inertial frame, the electromagnetic fields in a rotating 2D system can be decomposed to transverse electric (TE) modes and transverse magnetic (TM) modes (Sarma *et al.*, 2012). Without loss of generality, we consider TM modes below. To the first order of $\Omega R/c$, the wave equation for the electric field (parallel to z-axis) can be written in the polar coordinates as (Sunada and Harayama, 2006):

$$\left[\frac{\partial^2}{\partial r^2} + \frac{1}{r}\frac{\partial}{\partial r} + \frac{1}{r^2}\frac{\partial^2}{\partial \varphi^2} + 2ik\frac{\Omega}{c}\frac{\partial}{\partial \varphi} + n^2k^2\right] E_z(r,\varphi) = 0, \tag{53}$$

where n is the refractive index inside the cavity, $k = 2\pi/\lambda$, λ is the vacuum wavelength.

In a circular cavity of radius R, the separation of variables gives $E_z(r,\varphi) = f(r)e^{-im\varphi}$, where m is an integer, and

$$\left[\frac{\partial^2}{\partial r^2} + \frac{1}{r}\frac{\partial}{\partial r} - \frac{m^2}{r^2} + K_m^2\right] f(r) = 0, \tag{54}$$

where

$$K_m^2 = k^2\left[n^2 + 2m\left(\frac{\Omega}{\omega}\right)\right], \tag{55}$$

and $\omega = ck$. Equation (55) implies that rotation induces a change of the dielectric constant or the refractive index, which is given by

$$n_\Omega^2 = n^2 + 2m(\Omega/\omega). \tag{56}$$

For a given direction of rotation, the CW and CCW waves inside the cavity experience different n_Ω as their azimuthal numbers, m, are of opposite sign. The wave traveling in the same direction of rotation acquires a higher n_Ω than that traveling in the opposite rotation, thus rotation lifts the degeneracy of WGMs. For a closed cavity, where Dirichlet boundary conditions are applied at the boundary, the frequency splitting between CW and CCW modes can be obtained to the first order of Ω (Sunada and Harayama, 2006)

$$\Delta\omega = \frac{2|m|}{n^2}\Omega. \tag{57}$$

Equation (57) describes the Sagnac effect in a closed cavity.

For an open cavity, n_Ω is modified both inside and outside the cavity. It is difficult, however, to obtain an analytical expression for the Sagnac effect. Numerical simulation (Sarma *et al.*, 2012) shows that the rotation-induced frequency splitting between CW and CCW modes in an open microcavity is larger than that in a closed cavity of same R. This is attributed to the increased mode size in the open cavity, where the electromagnetic fields extend beyond the cavity boundary.

B. Wave chaos in rotating cavities

In the last subsection, we consider circular cavities in which the WGMs consist of CW- and CCW-propagating waves, and the Sagnac effect is consistent with the original description based on the path length difference between the CW and CCW waves. When the cavity shape is deformed from a circle, the intracavity ray dynamics may become chaotic or partially chaotic, and the resonant modes may not localize on well-defined ray trajectories. What happens to the chaotic microcavities upon rotation? To answer this question, Harayama and coworkers developed a perturbation theory to analyze the effects of rotation in deformed microcavities (Sunada and Harayama, 2006). They treated the rotation term in the wave equation as a perturbation to the cavity resonances, and calculated the changes in resonance frequencies and wave functions.

Without rotation, the CW and CCW waves in a circular cavity have the same frequency, and their superposition forms the standing waves. In a deformed cavity, the CW and CCW waves are often coupled, which lift the degeneracy. The eigenmodes have slightly different frequencies, and the eigenfunctions are standing waves [assuming that a mirror-reflection symmetry is present or that the system is closed (Wiersig *et al.*, 2011a)] approximately described for small deformation by sine or cosine functions. Due to their frequency difference, the eigenmodes cannot superpose to form CW or CCW modes. The frequency splitting, caused by cavity shape deformation, leads to a threshold for the Sagnac effect (Sunada and Harayama, 2007). When the rotation speed Ω is less than the threshold value Ω_{th}, the frequency shift due to rotation is negligible.

Figure 45(a) presents an example of the quadrupole cavity. A pair of quasi-degenerate modes localized on a diamond-shaped periodic orbit is chosen. At low rotation speed, the frequency difference of the two modes does not increase with the angular velocity Ω. Only when Ω exceeds a threshold (Ω_{th}), the frequency difference increases proportionally to the angular velocity Ω. Therefore, there exists a dead zone ($|\Omega| < \Omega_{th}$) for the Sagnac effect due to intrinsic frequency splitting from cavity deformation.

The existence of a dead zone is detrimental to the application of microcavity to optical gyroscope. To eliminate the dead zone, Sunada and Harayama (2007) designed a microcavity of symmetry $C_{p\nu}$. The cavity boundary is defined by $r(\varphi) = R(1 + \varepsilon \cos p\varphi)$, where p is an integer and $p \geq 3$. Despite its shape is deformed from a circle, such cavity supports degenerate modes. Upon rotation, the frequency degeneracy is lifted, and the frequency splitting is proportional to angular velocity Ω. Figure 45(b) shows an example of a pair of degenerate modes localized on a triangle-shaped periodic orbit in a cavity of $p = 3$ and $\varepsilon = 0.065$. The absence of dead zone is evident.

In the above examples, the cavity resonances localize on periodic ray orbits, so the Sagnac effect is similar to that in a ring cavity. However, the deformed microcavities also support wave chaotic modes, which do not localize on any ray-dynamical trajectories. The Sagnac effect still exists for wave chaotic modes, even though such modes do not convert to unidirectional-propagating wave modes upon rotation. Harayama *et al.* (2007) showed numerically that the angular momentum spectra of wave-chaotic modes contain both CW and CCW propagating wave components even at high rotation speed. Nevertheless, the frequency splitting of two degenerate modes is proportional to the angular velocity. This can be explained by the average angular momentum $\langle m \rangle$, which turns positive and negative for the two modes upon rotation. The frequency splitting is then given by the difference in their average angular momenta, $\Delta\omega = 2|\langle m \rangle|\Omega/n^2$, which is a more general expression than Eq. (57).

C. Rotation-induced changes of quality factors of open microcavities

In the previous subsection, the rotating microcavities have closed boundary, and the frequency splitting is the only observable for rotation sensing. The small cavity size, however, weakens the Sagnac effect dramatically, and the frequency shift in a microcavity is too small to detect. In reality, most microcavities at optical frequency are made of dielectric materials, as metal is lossy. Such cavities have open boundaries, from which light may escape. Hence, the cavity resonances have complex frequencies, the real part representing the oscillation frequency, the imaginary part reflecting the decay time or the quality (Q) factor. The Q determines the lasing threshold and the emission power above the threshold. According to Eq. (56), both the refractive index inside the cavity n_i and outside the cavity n_o are modified by rotation. The resulting change in the refractive index contrast affects the degree of optical confinement in the cavity. Therefore, in an open microcavity, rotation not only induces a resonant frequency shift, but also modifies the lasing threshold and the output power level. The latter modifications can be more sensitive to the rotation than the lasing frequencies, because the lasing threshold is determined by the Q factor which scales exponentially with the refractive index contrast. For example, in circular Bragg microlasers, the rotation-induced intensity modulation has exponential dependence on the rotation velocity (Scheuer, 2007). Next let us see what happens to a dielectric microdisk where light is confined by total internal reflection at the disk boundary.

To investigate the change of quality factor by rotation, Sarma *et al.* (2012) developed a FDTD algorithm to simulate microdisk cavities in the rotating frame. Unlike the previous FDTD model which substitutes the constitutive relations into the Maxwell's equations, they solved simultaneously and separately the Maxwell's equations (which is identical to those in a stationary frame) and the modified constitutive relations in the rotating frame. In a circular microdisk, for a WGM traveling in the same direction of rotation, the Q factor decreases exponentially with the angular velocity Ω, whereas the Q factor for a WGM traveling in the opposite direction of rotation increases exponentially (Sarma *et al.*, 2012).

The exponential dependence of Q factor on Ω can be explained by the rotation-induced change in the refractive index contrast. Assuming the refractive index outside the cavity is equal to 1 at $\Omega = 0$, the refractive index difference at the angular velocity Ω is

$$n_i(\Omega) - n_o(\Omega) \simeq (n_i(0) - 1) + \left(\frac{m\Omega}{\omega}\right)\left[\frac{1}{n_i(0)} - 1\right]. \tag{58}$$

Equation (58) implies the rotation increases the refractive index difference for the counter-propagating mode (wave traveling in the opposite direction of rotation). Thus its Q factor increases with the rotation speed Ω. For the co-propagating mode (wave traveling in the same direction of rotation), the Q factor decreases with rotation. In a circular microdisk, the change in the refractive index contrast is symmetric and opposite for the pair of CW and CCW modes. The Q factor of the WGM depends exponentially on the difference in the refractive index inside and outside the cavity. Since the index difference varies linearly with the rotation speed (Eq. (58)), the Q factor changes exponentially with Ω.

For the wavelength-scale cavity, Sarma *et al.* (2012) found the sensitivity of the Q factor to rotation is more than one order of magnitude higher than that of the resonant frequency (Fig. 46). The change of Q by rotation would modify the lasing thresholds for CW and CCW modes, and break the balance between the CW and CCW output power. The higher sensitivity of Q to Ω indicates the rotation-induced changes in lasing threshold and output power can be more dramatic than the lasing frequency shift in the wavelength-scale microdisk lasers.

In deformed microcavities, the Q factors for a quasi-degenerate pair of resonances may cross or anticross with increasing rotation speed (Ge *et al.*, 2014b). While the standing-wave resonances at $\Omega = 0$ evolve to traveling-wave resonances at high Ω, either the clockwise (CW) or counterclockwise (CCW) traveling-wave resonance can have a lower Q, contrary to the intuitive expectation from the rotation-dependent effective index of refraction in a circular cavity. With increasing rotation speed, a phase locking between the CW and CCW waves in a resonance takes place. These phenomena result from the rotation-induced mode coupling, which is strongly influenced by the openness of the microcavity. Such coupling can also make the frequency splitting change non-monotonically with rotation (Ge *et al.*, 2014b).

D. Far-field patterns from rotating microcavities of deformed shape

Besides the resonant frequency and Q factor of a dielectric microcavity, the emission pattern in the far-field zone is also modified by rotation. A characteristic of deformed microcavities is the directional output. The output directionality can be dramatically altered due to rotation, which may be useful for rotation sensing. This is an advantage that deformed cavities have over circular cavities which have isotropic output.

Ge *et al.* (2014a) used a non-perturbative approach based on the modified scattering matrix method to calculate the far-field emission patterns of deformed microcavities. This method utilizes the analytical form of the cavity boundary and is free of spatial grids that are used in the finite-difference or finite-element method. When the deformed cavity has the chiral symmetry $[\rho(-\varphi) = \rho(\varphi)]$, CW and CCW traveling waves make equal contributions to each standing-wave resonance. The output directions of CW and CCW waves may differ, but they are symmetric with respect to the $\varphi = 0$ axis. Consequently, the far-field pattern of a standing-wave resonance has the mirror symmetry about the $\varphi = 0$ axis. With rotation, the balance between the CW and CCW waves in a resonance is broken, and the far-field pattern becomes asymmetric. This asymmetry increases linearly at low rotation speed, which is free of the “dead zone” that plagues the Sagnac effect. A coupled-mode theory has been employed to provide a quantitative explanation and guidance on the optimization of the far-field sensitivity to rotation (Ge *et al.*, 2014a).

A further increase of the emission sensitivity to rotation can be achieved by breaking the chiral symmetry of cavity shape (Sarma *et al.*, 2014). Without rotation, a pair of nearly-degenerate modes in an open microcavity with broken chiral symmetry $[\rho(-\varphi) \neq \rho(\varphi)]$ have similar far-field patterns, because they are both dominated by either CW or CCW traveling waves. With rotation, one of them evolves from co-propagating to counter-propagating wave mode, and its far-field pattern will change dramatically if the CW and CCW waves have distinct output directions. This is illustrated in Fig. 47 for an asymmetric limaçon cavity. The degree of spatial chirality can be tuned to maximize the difference between CW and CCW far-field patterns, and reach the highest sensitivity of microcavity emission to rotation (Sarma *et al.*, 2014).

In summary, the sensitivity of emission pattern to rotation can be many orders of magnitude higher than the Sagnac effect, providing an alternative mechanism of rotation sensing for on-chip gyroscopes.

X. SUMMARY AND PROSPECTS

In the past two decades, the quest to achieve directional radiation from microcavity lasers has stimulated a lot of activities in the field of optical microresonators and considerably deepened our understanding of them by applying very different physical principles and mechanisms and by using theoretical concepts that were originally developed in other fields. As a result, a number of distinct approaches were found and investigated, and they comprise a broad range of concepts from tailoring resonator shapes for directed light emission (such as in the limaçon microlasers) to mode interactions occurring at avoided resonance crossings (such as in the annular resonator) or a pumping-induced mode-beating interaction (such as in the spiral cavity). They not only considerably enlarged our understanding of microlasers, but at the same time highlighted the role played by wave chaos in such open systems. The recognition of the importance of the unstable manifold that explains, e.g., the observed universality of the far-field patterns, is one prominent example for this. In turn, based on this knowledge, new resonator shapes can now be designed and easily (pre-)tested by ray and wave simulations, which is a tremendously help to the application side.

The output directionality of deformed microcavities also provide alternative schemes for microcavity-based sensors. In addition to resonance frequency shift, a change of far-field pattern may be used for high-precision on-chip rotation rate detection. From the time reversal point of view, directional emission implies directional excitation, namely, free-space propagating beams can be efficiently coupled into microcavities (Lee *et al.*, 2007b; Liu *et al.*, 2012). More recently, active control of emission directionality of semiconductor microdisk lasers has been demonstrated by shaping the spatial profile of the pump (Liew *et al.*, 2014). The adaptive pumping technique provides an efficient way of tuning the lasing frequency and the output direction. Such tunability by external pump after the laser is fabricated will enhance the functionality of microcavity lasers.

One important direction for future research on chaotic microcavities is the study of the details of the localization of optical modes on the chaotic saddle and its unstable manifold. In particular, it is still a puzzle why the appearance of scarred modes in open microcavities is the rule rather than the exception. Another future direction is three-dimensional chaotic microcavities. Most of the work that have been done so far is on two-dimensional microcavities. Three-dimensional cavities have more degree of freedom and can produce interesting effects that do not exist in two dimension.

Although most studies on deformed cavities were focused on microlasers, single photon sources would also benefit from the unique characteristic of deformed microcavities, e.g., efficient collection of emission and directional coupling to waveguides. One future direction could be the application of deformed dielectric microcavities to the cavity quantum electrodynamics, e.g., to study the influence of wave chaos on weak or strong coupling of single emitters to cavity resonances.

For dense on-chip integration, there is an increasing push for further reduction of cavity size to subwavelength scale. Although optical diffraction limits the cavity size to the wavelength (in the dielectric material), recent works aimed to overcome this limit by utilizing plasmonic effects (Bergman and Stockman, 2003; Ma *et al.*, 2012). Hybrid metal-dielectric cavities were fabricated, and surface-plasmons at the meta-dielectric interfaces enable confinement of optical energy in nanoscale dimension (Hill *et al.*, 2007; Ma *et al.*, 2010; Min *et al.*, 2009; Nezhad *et al.*, 2010; Oulton *et al.*, 2009). It would be interesting to extend the concepts and approaches developed for the dielectric microcavities to metal-dielectric nanocavities to control the surface plasmon modal distributions, spectra, lifetimes and emission characteristics. Furthermore, the exploration of microcavities made with novel materials, e.g., metamaterials with negative refractive index, would lead to unusual phenomena such as negative refraction and negative Goos-Hänchen shift (Wiersig *et al.*, 2010).

The existence of exceptional points and related non-Hermitian effects in optical microcavities is now established. It would be interesting to study in the future the influence of the exceptional points on light-matter interaction in microcavities. Further future topics are non-Hermitian effects in CROWs and the properties of higher-order exceptional points in optical microcavities.

ACKNOWLEDGMENTS

We thank A. Eberspächer, Q. H. Song, L. Ge, B. Redding, R. Sarma for preparing some of the figures, and M. Hentschel and J.-B. Shim for discussions. Financial support from the DFG research unit 760 and US NSF Divisions of ECCS and CMP is acknowledged.

REFERENCES

Aiello, A., M. Merano, and J. P. Woerdman (2009), Phys. Rev. A **80**, 061801(R).

Albert, F., T. Braun, T. Heidel, C. Schneider, S. Reitzenstein, S. Höfling, L. Worschech, and A. Forchel (2010), Appl. Phys. Lett **97**, 101108.

Albert, F., C. Hopfmann, A. Eberspächer, F. Arnold, M. Emmerling, C. Schneider, S. Höfling, A. Forchel, M. Kamp, J. Wiersig, and S. Reitzenstein (2012), Appl. Phys. Lett **101**, 021116.

Ozorio de Almeida, A. M. (1984), J. Phys. Chem. **88**, 6139.

Altmann, E. G. (2009), Phys. Rev. A **79**, 013830.

Altmann, E. G., G. Del Magno, and M. Hentschel (2008), Euro. Phys. Lett. **84**, 10008.

Altmann, E. G., J. S. E. Portela, and T. Tél (2013), Rev. Mod. Phys. **85**, 869.

Andreasen, J., H. Cao, J. Wiersig, and A. E. Motter (2009), Phys. Rev. Lett. **103**, 154101.

Aoki, T., B. Dayan, E. Wilcut, W. P. Bowen, A. S. Parkins, T. J. Kippenberg, K. J. Vahala, and H. J. Kimble (2006), Nature **443**, 671.

Apalkov, V. M., and M. E. Raikh (2004), Phys. Rev. B **70**, 195317.

Armani, A. M., R. P. Kulkarni, S. E. Fraser, R. C. Flagan, and K. J. Vahala (2007), Science **317**, 783.

Armani, D. K., T. J. Kippenberg, S. M. Spillane, and K. J. Vahala (2003), Nature **421**, 925.

Arnol′d, V. I. (1963), Russ. Math. Surveys **18** (6), 85.

Arnol′d, V. I. (1964), Sov. Math. Dokl. **6**, 581.

Arnol′d, V. I. (1978), *Mathematical Methods of Classical Mechanics*, Graduate Texts in Mathematics, Vol. 60 (Springer, Berlin).

Arroyo, A., R. Markarian, and D. P. Sanders (2009), Nonlinearity **22**, 1499.

Artmann, K. (1948), Ann. Phys. (Leipzig) **437**, 87.

Artuso, R., I. Guarneri, and L. Rebuzzini (2000), Chaos **10** (1), 189.

Aspelmeyer, M., T. J. Kippenberg, and F. Marquardt (2013), Arxiv **cond-mat.mes-hall**, 1303.0733v1.

Atlasov, K. A., K. F. Karlsson, A. Rudra, B. Dwir, and E. Kapon (2008), Opt. Express **16**, 16255.

Audet, R., M. A. Belkin, J. A. Fan, B. G. Lee, K. Lin, and F. Capasso (2007), Appl. Phys. Lett. **91**, 131106.

Baba, T. (1997), IEEE J. Sel. Top. Quantum Electron. **3**, 808.

Bäcker, A., R. Ketzmerick, S. Löck, M. Robnik, G. Vidmar, R. Höhmann, U. Kuhl, and H.-J. Stöckmann (2008a), Phys. Rev. Lett. **100**, 174103.

Bäcker, A., R. Ketzmerick, S. Löck, and L. Schilling (2008b), Phys. Rev. Lett. **100**, 104101.

Bäcker, A., R. Ketzmerick, S. Löck, J. Wiersig, and M. Hentschel (2009), Phys. Rev. A **79**, 063804.

Backes, S. A., J. R. A. Cleaver, A. P. Heberle, and K. Köler (1998), J. Vac. Sci. Technol. B **16**, 3817.

Bahl, G., M. Tomes, F. Marquardt, and T. Carmon (2012), Nature Physics **8**, 203.

Bahl, G., J. Zehnpfennig, M. Tomes, and T. Carmon (2011), Nature Communications **2**, 403.

Balian, R., and C. Bloch (1970), Ann. Phys. **60**, 401.

Balian, R., and C. Bloch (1971), Ann. Phys. **64**, 271.

Balian, R., and C. Bloch (1972), Ann. Phys. **69**, 76.

Baryshnikov, Y., P. Heider, W. Parz, and V. Zharnitsky (2004), Phys. Rev. Lett. **93**, 133902.

Ben-Messaoud, T., and J. Zyss (2005), Appl. Phys. Lett. **86**, 241110.

Bender, C. M., and S. Boettcher (1998), Phys. Rev. Lett. **80**, 5243.

Bensimon, D., and L. P. Kadanoff (1984), Physica D **13**, 82.

Benyoucef, M., J.-B. Shim, J. Wiersig, and O. G. Schmidt (2011), Opt. Lett. **36**, 1317.

van den Berg, P. M., and J. T. Fokkema (1979), IEEE Trans. Antennas Propag. **27** (5), 577.

Bergman, D. J., and M. I. Stockman (2003), Phys. Rev. Lett. **90**, 027402.

Berman, P. R. (2002), Phys. Rev. E **66**, 067603.

Berry, M. V. (1977), J. Phys. A **10**, 2083.

Berry, M. V. (1981), Eur. J. Phys. **2**, 91.

Berry, M. V. (2003), J. Mod. Optics **50**, 63.

Berry, M. V., and M. Tabor (1976), Proc. R. Soc. Lond. A **349**, 101.

Berry, M. V., and M. Wilkinson (1984), Proc. R. Soc. Lond. A. **392**, 15.

Birchall, C., and H. Schomerus (2012), J. Phys. A: Math. Theor. **45**, 444006.

Birkhoff, G. D. (1927), Acta Math **50**, 359.

Bittner, S., E. Bogomolny, B. Dietz, M. Miski-Oglu, P. O. Iriarte, A. Richter, and F. Schäfer (2010), Phys. Rev. E **81**, 066215.

Bittner, S., E. Bogomolny, B. Dietz, M. Miski-Oglu, and A. Richter (2012a), Phys. Rev. E **85**, 026203.

Bittner, S., B. Dietz, R. Dubertrand, J. Isensee, M. Miski-Oglu, and A. Richter (2012b), Phys. Rev. E **85**, 056203.

Bittner, S., B. Dietz, U. Günther, H. L. Harney, M. Miski-Oglu, A. Richter, and F. Schäfer (2012c), Phys. Rev. Lett. **108**, 024101.

Bittner, S., B. Dietz, M. Miski-Oglu, P. O. Iriarte, A. Richter, and F. Schäfer (2009), Phys. Rev. A **80**, 023825.

Bliokh, K. Y., and A. Aiello (2013), J. Opt. **15**, 014001.

Bogomolny, E., B. Dietz, M. Miski-Oglu, A. Richter, F. Schäfer, and C. Schmit (2006), Phys. Rev. Lett. **97**, 254102.

Bogomolny, E., N. Djellali, R. Dubertrand, I. Gozhyk, M. Lebental, C. Schmit, C. Ulysee, and J. Zyss (2011), Phys. Rev. E **83**, 036208.

Bogomolny, E., and R. Dubertrand (2012), Phys. Rev. E **86**, 026202.

Bogomolny, E., R. Dubertrand, and C. Schmit (2008), Phys. Rev. E **78**, 056202.

Bogomolny, E., and C. Schmit (2004), Phys. Rev. Lett. **92**, 244102.

Bogomolny, E. B., U. Gerland, and C. Schmit (1999), Phys. Rev. E **59**, R1315.

Borgonovi, F., G. Casati, and B. Li (1996), Phys. Rev. Lett. **77** (23), 4744.

Boriskina, S. V. (2006), Opt. Lett **31**, 338.

Boriskina, S. V. (2007), Opt. Lett **32**, 1557.

Boriskina, S. V., T. M. Benson, P. Sewell, and A. Nosich (2006), IEEE J. Sel. Top. Quantum Electron. **12**, 52.

Boriskina, S. V., P. Sewell, T. M. Benson, and A. Nosich (2004), J. Opt. Soc. Am. A **21**, 393.

Borselli, M., J. Johnson, and O. Painter (2005), Opt. Express **13**, 1515.

Brandstetter, M., M. Liertzer, C. Deutsch, P. Klang, J. Schoöberl, H. E. Türeci, G. Strasser, K. Unterrainer, and S. Rotter (2014), Nat. Commun. **5**, 4034.

Braun, I., G. Ihlein, F. Laeri, J. U. Nöckel, G. Schulz-Ekloff, F. Schüth, U. Vietze, Ö. Weiß, and D. Wöhrle (2000), Appl. Phys. B: Lasers Opt. **70**, 335.

Brodier, O., P. Schlagheck, and D. Ullmo (2001), Phys. Rev. Lett. **87**, 064101.

Brown, R. C., and R. E. Wyatt (1986), Phys. Rev. Lett. **57**, 1.

Bunimovich, L. A. (1974), Funct. Anal. Appl. **8**, 254.

Bunimovich, L. A. (2001), Chaos **11**, 802.

Cai, M., O. Painter, and K. J. Vahala (2000), Phys. Rev. Lett. **85**, 74.

Cai, X. C., G. Mezosi, M. Sorel, Z. Wang, Y. Shu, P. Jiang, and S. Yu (2011), IEEE Photon. Tech. Lett. **23**, 1636.

Cao, H., J. Y. Xu, Y. Xiang, W. H. Ma, S.-H. Chang, S. T. Ho, and G. S. Solomon (2000), Appl. Phys. Lett. **76**, 3519.

Carmon, T., H. G. L. Schwefel, L. Yang, M. Oxborrow, A. D. Stone, and K. J. Vahala (2008), Phys. Rev. Lett. **100**, 103905.

Carmon, T., and K. J. Vahala (2007), Phys. Rev. Lett. **98**, 123901.

Casati, G., B. V. Chirikov, F. M. Izraelev, and J. Ford (1979), Lect. Notes. Phys. **93**, 334.

Casati, G., and T. Prosen (1999), Phys. Rev. E **59**, 2516(R).

Chan, C. C., and T. Tamir (1985), Opt. Lett. **10**, 378.

Chang, L., X. Jiang, S. Hua, C. Yang, J. Wen, L. Jiang, G. Li, G. Wang, and M. Xiao (2014), Nat. Photon. **8**, 524.

Chang, R. K., and A. J. Campillo (1996), *Optical Processes in Microcavities*, Advanced Series in applied Physics, Vol. 3 (World Scientific, Singapore).

Chang, S., R. K. Chang, A. D. Stone, and J. U. Nöckel (2000), J. Opt. Soc. Am. B **17** (4), 1828.

Chen, Q., Y.-Z. Huang, and L.-J. Yu (2006), IEEE J. Quantum Electronics **42**, 59.

Chen, R., T.-T. D. Tran, K. W. Ng, W. S. Ko, F. G. Chuang, L. S. Sedgwick, and C. Chang-Hasnain (2011), Nature Photonics **5**, 170.

Chern, G. D., A. W. Poon, R. K. Chang, T. Ben-Messaoud, O. Alloschery, E. Toussaere, J. Zyss, and S. Y. Kuo (2004), Opt. Lett. **29**, 1674.

Chern, G. D., H. E. Tureci, A. D. Stone, R. K. Chang, M. Kneissl, and N. M. Johnson (2003), Appl. Phys. Lett. **83**, 1710.

Chiasera, A., Y. Dumeige, P. Féron, M. Ferrari, Y. Jestin, G. N. Conti, S. Pelli, S. Sora, and G. C. Righini (2010), Laser Photonics Rev. **4**, 457.

Cho, J., S. Rim, and C.-M. Kim (2011), Phys. Rev. A **83**, 043810.

Chong, Y. D., L. Ge, and A. D. Stone (2011), Phys. Rev. Lett. **106**, 093902.

Chong, Y. D., and A. D. Stone (2012), Phys. Rev. Lett. **109**, 063902.

Chow, W. W., J. Geabanacloche, L. M. Pedrotti, V. E. Sanders, W. Schleich, and M. O. Scully (1985), Rev. Mod. Phys. **57**, 61.

Chowdhury, D. Q., D. H. Leach, and R. K. Chang (1994), J. Opt. Soc. Am. A **11** (3), 1110.

Collot, L., V. Lefevre-Seguin, M. Brune, J. Raimond, and S. Haroche (1993), Europhys. Lett. **23**, 327.

Creagh, S. C. (2007), Phys. Rev. Lett. **98**, 153901.

Creagh, S. C., and M. M. White (2010), J. Phys. A: Math. Theor. **43**, 465102.

Creagh, S. C., and M. M. White (2012), Phys. Rev. E **85**, 015201(R).

Crespi, B., G. Perez, and S.-J. Chang (1993), Phys. Rev. E **47**, 986.

Cui, J. M., C. H. Dong, C. L. Zou, F. W. Sun, Y. F. Xiao, Z. F. Han, and G. C. Guo (2013), IEEE J. Sel. Top. Quantum Electron. **19**, 9000406.

Czekalla, C., C. Sturm, R. Schmidt-Grund, B. Cao, M. Lorenz, and M. Grundmann (2008), Appl. Phys. Lett. **92**, 241102.

Davis, M. J., and E. J. Heller (1981), J. Chem. Phys. **75**, 246.

Demange, G., and E.-M. Graefe (2012), J. Phys. A: Math. Theor. **45**, 025303.

Dembowski, C., B. Dietz, H.-D. Gräf, H. L. Harney, A. Heine, W. D. Heiss, and A. Richter (2003), Phys. Rev. Lett. **90**, 034101.

Dembowski, C., B. Dietz, H.-D. Gräf, H. L. Harney, A. Heine, W. D. Heiss, and A. Richter (2004), Phys. Rev. E **69**, 056216.

Dembowski, C., H.-D. Gräf, H. L. Harney, A. Heine, W. D. Heiss, H. Rehfeld, and A. Richter (2001), Phys. Rev. Lett. **86**, 787.

Dembowski, C., H.-D. Gräf, A. Heine, R. Hofferbert, H. Rehfeld, and A. Richter (2000), Phys. Rev. Lett. **84**, 867.

Desouter-Lecomte, M., and V. Jacquest (1995), J. Phys. B **28**, 3225.

Dettmann, C. P., G. V. Morozov, M. Sieber, and H. Waalkens (2008), Europhys. Lett. **82**, 34002.

Dettmann, C. P., G. V. Morozov, M. Sieber, and H. Waalkens (2009a), Europhys. Lett. **87**, 34003.

Dettmann, C. P., G. V. Morozov, M. Sieber, and H. Waalkens (2009b), Phys. Rev. A **80**, 063813.

Deych, L., M. Ostroswski, and Y. Yi (2011), Opt. Lett. **36**, 3154.

Di Falco, A., T. F. Krauss, and Fratalocchi (2012), Appl. Phys. Lett. **100**, 184101.

Dietrich, C. P., and M. Grundmann (2012), Phys. Status Solidi B **249**, 871.

Dietrich, C. P., M. Lange, C. Böntgen, and M. Grundmann (2012), Appl. Phys. Lett. **101**, 141116.

Dietrich, C. P., M. Lange, C. Sturm, R. Schmidt-Grund, and M. Grundmann (2011), New J. Phys. **13**, 103021.

Dietz, B., T. Friedrich, J. Metz, M. Miski-Oglu, A. Richter, F. Schäfer, and C. A. Stafford (2007), Phys. Rev. E **75**, 027201.

Dietz, B., H. L. Harney, O. N. Kirillov, M. Miski-Oglu, A. Richter, and F. Schäfer (2011), Phys. Rev. Lett. **106**, 150403.

Djellali, N., I. Gozhyk, D. Owens, S. Lozenko, M. Lebental, J. Lautru, C. Ulysse, B. Kippelen, and J. Zyss (2009), Appl. Phys. Lett. **95**, 101108.

Dong, H., Z. Chen, L. Sun, J. Lu, W. Xie, H. Hoe Tan, C. Jagadish, and X. Shen (2009), Appl. Phys. Lett **94**, 173115.

Doron, E., and S. D. Frischat (1995), Phys. Rev. Lett. **75**, 3661.

Dubertrand, R., E. Bogomolny, N. Djellali, M. Lebental, and C. Schmit (2008), Phys. Rev. A **77**, 013804.

Eberspächer, A., J. Main, and G. Wunner (2010), Phys. Rev. E **82**, 046201.

El-Ganainy, R., K. G. Makris, D. N. Christodoulides, and Z. H. Musslimani (2007), Opt. Lett. **32**, 2632.

Ermann, L., G. G. Carlo, and M. Saraceno (2009), Phys. Rev. Lett. **103**, 054102.

Faist, J., C. Gmachl, M. Striccoli, C. Sirtori, F. Capasso, D. L. Sivco, and A. Y. Cho (1996), Appl. Phys. Rev. **69**, 2456.

Fang, W., and H. Cao (2007), Appl. Phys. Lett. **91**, 041108.

Fang, W., H. Cao, V. Podolskiy, and E. Narimanov (2005a), Opt. Express **13**, 5641.

Fang, W., H. Cao, and G. S. Solomon (2007), Appl. Phys. Lett. **90**, 081108.

Fang, W., A. Yamilov, and H. Cao (2005b), Phys. Rev. A **72**, 023815.

Fishmann, S., D. R. Grempel, and R. E. Prange (1982), Phys. Rev. Lett. **49**, 509.

Foster, D. H., A. K. Cook, and J. U. Nöckel (2007), Opt. Lett. **32**, 1764.

Frahm, K. M., and D. L. Shepelyansky (1997), Phys. Rev. Lett. **78**, 1440.

Fujita, M., and T. Baba (2001), IEEE J. Quantum Electronics **37**, 1253.

Fujita, M., and T. Baba (2002), Appl. Phys. Lett. **80**, 2051.

Fukushima, T., and T. Harayama (2004), J. Select. Top. Quantum Elec. **10**, 1039.

Fukushima, T., T. Harayama, and J. Wiersig (2006), Phys. Rev. A **73**, 023816.

Fyodorov, Y. V., and H.-J. Sommers (1997), J. Math. Phys. **38**, 1918.

Gamow, G. (1928), Z. Phys. **51**, 204.

Gao, J., P. Heider, C. J. Chen, X. Yang, C. A. Husko, and C. W. Wong (2007), Appl. Phys. Lett. **91**, 181101.

Gargas, D. J., M. C. Moore, A. Ni, S.-W. Chang, Z. Zhang, S.-L. Chuang, and P. Yang (2010), ACS Nano **4**, 3270.

Garrett, C. G. B., W. Kaiser, and W. L. Bond (1961), Phys. Rev. **124**, 1807.

Gaspard, P., and S. A. Rice (1989a), J. Chem. Phys. **90** (4), 2255.

Gaspard, P., and S. A. Rice (1989b), J. Chem. Phys. **90** (4), 2225.

Ge, L., Y. D. Chong, S. Rotter, H. E. Türeci, and A. D. Stone (2011), Phys. Rev. A **84**, 023820.

Ge, L., R. Sarma, and H. Cao (2014a), arXiv:1404.5289.

Ge, L., R. Sarma, and H. Cao (2014b), Phys. Rev. A **90**, 013809.

Ge, L., Q. Song, B. Redding, A. Eberspächer, J. Wiersig, and H. Cao (2013a), Phys. Rev. A **88**, 043801.

Ge, L., Q. H. Song, B. Redding, and H. Cao (2013b), Phys. Rev. A **87**, 023833.

Geisel, T., G. Radons, and J. Rubner (1986), Phys. Rev. Lett. **57**, 2883.

Gensty, T., K. Becker, I. Fischer, W. Elsasser, C. Degen, P. Debernardi, and G. P. Bava (2005), Phys. Rev. Lett. **94**, 233901.

Gmachl, C., F. Capasso, E. E. Narimanov, J. U. Nöckel, A. D. Stone, J. Faist, D. L. Sivco, and A. Y. Cho (1998), Science **280**, 1556.

Gmachl, C., E. E. Narimanov, F. Capasso, J. N. Baillargeon, and A. Y. Cho (2002), Opt. Lett. **27**, 824.

Goos, F., and H. Hänchen (1947), Ann. Phys. (Leipzig) **436**, 333.

Gorodetsky, M. L., and V. S. Ilchenko (1994), Opt. Commun. **113**, 133.

Gorodetsky, M. L., and V. S. Ilchenko (1999), J. Opt. Soc. Am. B **16**, 147.

Gorodetsky, M. L., A. D. Pryamikov, and V. S. Ilchenko (2000), J. Opt. Soc. Am B **17**, 1051.

Gorodetsky, M. L., A. A. Savchenkov, and V. S. Ilchenko (1996), Opt. Lett. **21**, 453.

Götte, J. B., S. Shinohara, and M. Hentschel (2013), J. Opt. **15**, 014009.

Grgić, J., E. Campaioli, S. Raza, P. Bassi, and N. A. Mortensen (2011), Opt. Quant. Electron **42**, 511.

Guo, A., G. J. Salamo, D. Duchesne, R. Morandotti, M. Volatier-Ravat, V. Aimez, G. A. Siviloglou, and D. N. Christodoulides (2009), Phys. Rev. Lett. **103**, 093902.

Guo, W.-H., Y.-Z. Huang, Q.-Y. Lu, and L.-J. Yu (2003), IEEE J. Quantum Elect. **39**, 1106.

Gutkin, E. (1996), J. Stat. Phys. **83** (1/2), 7.

Gutzwiller, M. C. (1971), J. Math. Phys. **12** (3), 343.

Gutzwiller, M. C. (1990), *Chaos in Classical and Quantum Mechanics*, Interdisciplinary Applied Mathematics, Vol. 1 (Springer, Berlin).

Hackenbroich, G. (2001), Physica E **9**, 560.

Hackenbroich, G., and J. U. Nöckel (1997), Europhys. Lett. **39**, 371.

Hales, R. F. M., M. Sieber, and H. Waalkens (2011), J. Phys. A: Math. Theor. **44**, 155305.

Harayama, T., T. Fukushima, P. Davis, P. Vaccaro, T. Miyasaka, T. Nishimura, and T. Aida (2003), Phys. Rev. E **67**, 015207(R).

Harayama, T., and S. Shinohara (2011), Lasers & Photonics Reviews **5**, 247.

Harayama, T., S. Sunada, and T. Miyasaka (2007), Phys. Rev. E **76**, 016212.

Harney, H. L., and W. D. Heiss (2004), Eur. Phys. J. D **29**, 429.

He, L., S. K. Özdemir, and L. Yang (2013), Laser Photonics Rev. **7**, 60.

He, L., S. K. Özdemir, J. Zhu, W. Kim, and L. Yang (2011), Nature Nanotechnology **6**, 428.

Heiss, W. D. (1999), Eur. Phys. J. D **7**, 1.

Heiss, W. D. (2000), Phys. Rev. E **61**, 929.

Heiss, W. D. (2010), Eur. Phys. J. D **60**, 257.

Heiss, W. D. (2012), J. Phys. A: Math. Theor. **45**, 444016.

Heiss, W. D., and H. L. Harney (2001), Eur. Phys. J. D **17**, 149.

Heller, E. J. (1984), Phys. Rev. Lett. **53**, 1515.

Hentschel, M. (2001), *Mesoscopic wave phenomena in electronic and optical ring structures*, PhD thesis (Universität Dresden).

Hentschel, M., and T.-Y. Kwon (2009), Opt. Lett. **34**, 163.

Hentschel, M., T.-Y. Kwon, M. A. Belkin, R. Audet, and F. Capasso (2009), Opt. Express **17**, 10335.

Hentschel, M., and K. Richter (2002), Phys. Rev. E **66**, 056207.

Hentschel, M., and H. Schomerus (2002), Phys. Rev. E **65**, 045603(R).

Hentschel, M., H. Schomerus, and R. Schubert (2003), Europhys. Lett. **62**, 636.

Hentschel, M., Q. J. Wang, C. Yan, F. Capasso, T. Edamura, and H. Kan (2010), Opt. Express **18**, 16437.

Herb, J., P. Meerwald, M. J. Moritz, and H. Friedrich (1999), Phys. Rev. A **60**, 853.

Hill, M. T., Y.-S. Oei, B. Smalbrugge, Y. Zhu, T. de Vries, P. J. vanVeldhoven, F. M. van Otten, T. J. Eijkemans, J. P. Turkiewicz, H. deWaardt, E. J. Geluk, S.-H. Kwon, Y.-H. Lee, R. Nótzel, and S. M. K. (2007), Nature Photon. **1**, 589.

Huang, K. F., Y. F. Chen, H. C. Lai, and Y. P. Lan (2002), Phys. Rev. Lett. **89**, 224102.

Husimi, K. (1940), Proc. Phys. Math. Soc. Jpn. **22**, 264.

Ilchenko, V. S., and A. B. Matsko (2006), IEEE J. Sel. Top. Quantum Electron. **12**, 15.

Jackson, J. D. (1962), *Classical Electrodynamics* (John Wiley and Sons, New York).

Jiang, X.-F., Y.-F. Xiao, C.-L. Zou, L. He, C.-H. Dong, B.-B. Li, Y. Li, F.-W. Sun, L. Yang, and Q. Gong (2012), Adv. Mater. **24**, 260.

Kapur, P. L., and R. Peierls (1938), Proc. Roy. Soc. Lond. A **166**, 277.

Kato, T. (1966), *Perturbation Theory for Linear Operators* (Springer, New York).

Keating, J. P., M. Novaes, S. D. Prado, and M. Sieber (2006), Phys. Rev. Lett. **97**, 15406.

Keating, J. P., M. Novaes, and H. Schomerus (2008), Phys. Rev. A **77**, 013834.

Kim, C., Y. J. Kim, E. S. Jang, G. C. Yi, and H. H. Kim (2006), Appl. Phys. Lett. **88**, 093104.

Kim, C.-M., S. H. Lee, K. R. Oh, and J. H. Kim (2009), Appl. Phys. Lett. **94**, 231120.

Kim, M., K. Kwon, J. Shim, Y. Jung, and K. Yu (2014), Opt. Lett. **39**, 2423.

Kim, S.-K., S.-H. Kim, G.-H. Kim, H.-G. Park, D.-J. Shin, and Y.-H. Lee (2004), Appl. Phys. Lett. **84**, 861.

Kippenberg, T. J., R. Holzwarth, and S. A. Diddams (2011), Science **332**, 555.

Kippenberg, T. J., J. Kalkman, A. Polman, and K. J. Vahala (2006), Phys. Rev. A **74**, 051802(R).

Kippenberg, T. J., and K. J. Vahala (2008), Science **321**, 1172.

Kneissl, M., M. Teepe, N. Miyashita, N. M. Johnson, G. D. Chern, and R. K. Chang (2004), Appl. Phys. Lett. **84**, 2485.

Kolmogorov, A. N. (1954), Dokl. Akad. Nauk SSSR **98**, 527.

Korthout, K., P. F. Smet, and D. Poelman (2009), Appl. Phys. Lett. **94**, 051104.

Kotik, D., and M. Hentschel (2013), J. Opt. **15**, 014010.

Kouno, T., K. Kishino, and M. Sakai (2011), IEEE J. Quantum Elect. **47** (12), 1565.

Kraft, M., and J. Wiersig (2014), to appear in Phys. Rev. A.

Kudo, H., R. Suzuki, and T. Tanabe (2013), arXiv:1304.3496.

Kuhl, U., R. Höhmann, J. Main, and H.-J. Stöckmann (2008), Phys. Rev. Lett. **100**, 254101.

Kuhl, U., R. Schäfer, and H. J. Stöckmann (2011), in *Trends in Nano- and Micro-Cavities*, edited by O. Kwon, B. Lee, and K. An (Bentham Books, Sharjah) pp. 153–185.

Kurdoglyan, M. S., S.-Y. Lee, S. Rim, and C.-M. Kim (2004), Opt. Lett. **29**, 2758.

Kuwata-Gonokami, M., R. H. Jordan, A. Dodabalapur, H. E. Katz, M. L. Schilling, R. E. Slusher, and S. Ozawa (1995), Opt. Lett. **20**, 2093.

Kwak, H., Y. Shin, S. Moon, and K. An (2013), arXiv:1305.6019.

Lacey, S., and H. Wang (2001), Opt. Lett. **26**, 1943.

Lacey, S., H. Wang, D. H. Foster, and J. U. Nöckel (2003), Phys. Rev. Lett. **91**, 033902.

Lai, C. M., H.-M. Wu, P.-C. Huang, S.-L. Wang, and L.-H. Peng (2007), Appl. Phys. Lett. **90**, 141106.

Lai, H. M., F. C. Cheng, and W. K. Tang (1986), J. Opt. Soc. Am. A **3**, 550.

Lai, Y.-C., and T. Tél (2010), *Transient Chaos* (Springer, Berlin).

Landau, R. H. (1996), *Quantum Mechanics II*, 2nd ed. (John Wiley & Sons, New York).

Lazutkin, Y. F. (1973), Izv. Acad. Sci. Ser. Math. **37**, 186.

Lebental, M., C. Djellali, N. Arnaud, J. S. Lauret, J. Zyss, R. Dubertrand, C. Schmit, and E. Bogomolny (2007), Phys. Rev. A **76**, 023830.

Lebental, M., J. S. Lauret, R. Hierle, and J. Zyss (2006), Appl. Phys. Lett. **88**, 031108.

Lee, J. Y., X. Luo, and A. W. Poon (2007a), Opt. Express **15**, 14650.

Lee, S. B., J. H. Lee, J. S. Chang, H. J. Moon, S. W. Kim, and K. An (2002), Phys. Rev. Lett. **88**, 033903.

Lee, S.-B., J. Yang, S. Moon, J.-H. Lee, K. An, J.-B. Shim, H.-W. Lee, and S. W. Kim (2007b), Appl. Phys. Lett. **90**, 041106.

Lee, S.-B., J. Yang, S. Moon, J.-H. Lee, K. An, J.-B. Shim, H.-W. Lee, and S. W. Kim (2007c), Phys. Rev. A **75**, 011802(R).

Lee, S.-B., J. Yang, S. Moon, S.-Y. Lee, J.-B. Shim, S. W. Kim, J.-H. Lee, and K. An (2009a), Phys. Rev. Lett. **103**, 134101.

Lee, S. B., J. Yang, S. Moon, S.-Y. Lee, J.-B. Shim, S. W. Kim, J.-H. Lee, and K. An (2009b), Phys. Rev. A **80**, 011802(R).

Lee, S.-Y. (2010), Phys. Rev. A **82**, 064101.

Lee, S.-Y., S. Rim, J.-W. Ryu, T.-Y. Kwon, M. Choi, and C.-M. Kim (2004), Phys. Rev. Lett. **93**, 164102.

Lee, S.-Y., S. Rim, J.-W. Ryu, T.-Y. Kwon, M. Choi, and C.-M. Kim (2008a), J. Phys. A: Math. Theor. **41**, 275102.

Lee, S.-Y., J.-W. Ryu, T.-Y. Kwon, S. Rim, and C.-M. Kim (2005), Phys. Rev. A **72**, 061801(R).

Lee, S.-Y., J.-W. Ryu, J.-B. Shim, S.-B. Lee, S. W. Kim, and K. An (2008b), Phys. Rev. A **78**, 015805.

Levi, A. F. J., R. E. Slusher, S. L. McCall, J. L. Glass, S. J. Pearton, and R. A. Logan (1993), Appl. Phys. Lett. **62**, 561.

Lichtenberg, A. J., and M. A. Lieberman (1992), *Regular and Chaotic Dynamics* (Springer, Berlin).

Liertzer, M., L. Ge, A. Cerjan, A. D. Stone, H. E. Türeci, and S. Rotter (2012), Phys. Rev. Lett. **108**, 173901.

Liew, S. F., B. Redding, L. Ge, G. S. Solomon, and H. Cao (2014), Appl. Phys. Lett. **104**, 231108.

Lin, H. B. (1992), J. Opt. Soc. Am. B **9**, 43.

Lin, H. B., J. D. Eversole, A. J. Campillo, and J. P. Barton (1998), Opt. Lett. **23**, 1921.

Lin, K. K. (2002), J. Comput. Phys. **176**, 295.

Lin, K. K., and M. Zworski (2002), Chem. Phys. Lett. **355**, 201.

Liu, J., S. Lee, Y. H. Ahn, J.-Y. Park, K. H. Koh, and K. H. Park (2008), Appl. Phys. Lett. **92**, 263102.

Liu, X., W. Fang, Y. Huang, X. H. Wu, S. T. Ho, H. Cao, and R. P. H. Chang (2004), Appl. Phys. Lett. **84**, 2488.

Liu, Y.-C., Y. F. Xiao, X.-F. Jiang, B.-B. Li, Y. Li, and Q. Gong (2012), Phys. Rev. A **85**, 013843.

Liu, Z.-P., X.-F. Jiang, Y. Li, Y.-F. Xiao, L. Wang, J.-L. Ren, S.-J. Zhang, H. Yang, and Q. Gong (2013), Appl. Phys. Lett. **102**, 221108.

Löck, S., A. Bäcker, R. Ketzmerick, and P. Schlagheck (2010), Phys. Rev. Lett. **104**, 114101.

Lohmeyer, M. (2002), Opt. Quantum Electron. **34**, 541.

Longhi, S. (2010), Phys. Rev. A **82**, 031801.

Lozenko, S., N. Djellali, I. Gozhyk, C. Delezoide, J. Lautru, C. Ulysse, J. Zyss, and M. Lebental (2012), J. Appl. Phys. **111**, 103116.

Lu, W. T., S. Sridhar, and M. Zworski (2003), Phys. Rev. Lett. **91**, 154101.

Ma, R. M., R. F. Oulton, V. J. Sorger, G. Bartal, and X. Zhang (2010), Nature Mater. **10**, 110.

Ma, R.-M., R. F. Oulton, V. J. Sorger, and X. Zhang (2012), Laser Photonics Rev. **7**, 1.

MacKay, R., I. Percival, and J. Meiss (1984), Physica D **13**, 55.

MacKay, R. S., and J. D. Meiss (1988), Phys. Rev. A **37**, 4702.

Martin, O. J. F., C. Girard, D. R. Smith, and S. Schultz (1999), Phys. Rev. Lett. **82**, 315.

Matsko, A. B., and V. S. Ilchenko (2006), IEEE J. Sel. Top. Quantum Electron. **12**, 3.

McCall, S. L., A. F. J. Levi, R. E. Slusher, S. J. Pearton, and R. A. Logan (1992), Appl. Phys. Lett. **60**, 289.

Meiss, J. (1992), Rev. Mod. Phys. **64**, 795.

Mekis, A., J. U. Nöckel, G. Chen, A. D. Stone, and R. K. Chang (1995), Phys. Rev. Lett. **75**, 2682.

Merano, M., A. Aiello, M. P. van Exter, and J. P. Woerdman (2009), Nature Photon. **3**, 337.

Mexis, M., S. Sergent, T. Guillet, C. Brimont, T. Bretagnon, B. Gil, F. Semond, M. Leroux, D. Néel, S. David, X. Checoury, and P. Boucaud (2011), Opt. Lett. **36**, 2203.

Michael, C. P. (2009), *Optical material characterization using microdisk cavities*, PhD thesis (California Institute of Technology).

Michler, M., A. Bäcker, R. Ketzmerick, H.-J. Stöckmann, and S. Tomsovic (2012), Phys. Rev. Lett. **109**, 234101.

Min, B. K., E. Ostby, V. Sorger, E. Ulin-Avila, L. Yang, X. Zhang, and K. J. Vahala (2009), Nature **457**, 455.

Misirpashaev, T. S., and C. Beenakker (1998), Phys. Rev. A **57**, 2041.

Moon, H. J., K. H. Ko, Y. C. Noh, G. H. Kim, J. H. Lee, and J. S. Chang (1997), Opt. Lett. **22**, 1739.

Moon, S., J. Yang, S.-B. Lee, J.-B. Shim, S. W. Kim, J.-H. Lee, and K. An (2008), Opt. Express **16**, 11007.

Moore, F. L., J. C. Robinson, C. Bharucha, P. E. Williams, and M. G. Raizen (1994), Phys. Rev. Lett. **73**, 2974.

Morichetti, F., C. Ferrari, A. Canciamilla, and A. Melloni (2012), Laser Photonics Rev. **6**, 74.

Moser, J. (1962), Nachr. Akad. Wiss. Gött., Math. Phys. Kl.II , 1.

Müller, D., D. Tharanga, A. A. Stahlhofen, and G. Nimtz (2006), Europhys. Lett. **73**, 526.

Narimanov, E. E., G. Hackenbroich, P. Jacquod, and A. D. Stone (1999), Phys. Rev. Lett. **83** (24), 4991.

von Neumann, J., and E. P. Wigner (1929), Z. Phys. **30**, 467.

Nezhad, M. P., A. Simic, O. Bondarenko, B. Slutsky, A. Mizrahi, L. Feng, V. Lomakin, and Y. Fainman (2010), Nature Photon. **6**, 395.

Nobis, T., and M. Grundmann (2005), Phys. Rev. A **72**, 063806.

Nobis, T., E. Kaidashev, A. Rahm, M. Lorenz, and M. Grundmann (2004), Phys. Rev. Lett. **93** (10), 103903.

Nobis, T., A. Rahm, C. Czekalla, M. Lorenz, and M. Grundmann (2007), Superlattices and Microstructures **42**, 333.

Nöckel, J. U. (1997), *Resonances in Nonintegrable Open Systems*, Ph.D. thesis (Yale University).

Nöckel, J. U., and A. D. Stone (1995), in *Optical Processes in Microcavities*, Advanced Series in applied Physics, Vol. 3, edited by R. K. Chang and A. J. Campillo (World Scientific, Singapore) pp. 389–426.

Nöckel, J. U., and A. D. Stone (1997), Nature (London) **385**, 45.

Nöckel, J. U., A. D. Stone, and R. K. Chang (1994), Opt. Lett. **19**, 1693.

Nöckel, J. U., A. D. Stone, G. Chen, H. L. Grossman, and R. K. Chang (1996), Opt. Lett. **21**, 1609.

Nonnenmacher, S. (2006), in *Mathematical Physics of Quantum Mechanics*, Springer Lecture Notes in Physics, Vol. No. 690, edited by J. Asch and A. Joye (Springer, Berlin) pp. 435–450.

Nonnenmacher, S. (2011), Nonlinearity **24**, R123.

Nonnenmacher, S., and E. Schenk (2008), Phys. Rev. E **78**, 045202(R).

Nonnenmacher, S., and M. Zworski (2007), Commun. Math. Phys. **269**, 311.

Ott, E. (1993), *Chaos in Dynamical Systems* (Cambridge University Press, Cambridge).

Oulton, R. F., V. J. Sorger, T. Zentgraf, R. M. Ma, C. Gladden, G. Dai, L. Bartal, and X. Zhang (2009), Nature **461**, 629.

Paek, J. H., T. Nishiwaki, M. Yamaguchi, and N. Sawaki (2010), Physica E **42**, 2722.

Park, Y.-S., and H. Wang (2009), Nature Physics **5**, 489.

Peng, B., Ş. K. Özdemir, F. Lei, F. Monfi, M. Gianfreda, G. L. Long, S. Fan, F. Nori, C. M. Bender, and L. Yang (2014), Nature Physics **10**, 394.

Peng, L.-H., C.-Y. Lu, W.-H. Wu, and S.-L. Wang (2005), Appl. Phys. Lett. **87**, 161902.

Percival, I. C. (1973), J. Phys. B **6**, L229.

Persson, E., T. Gorin, and I. Rotter (1998), Phys. Rev. E **58**, 1334.

Persson, E., I. Rotter, H.-J. Stöckmann, and M. Barth (2000), Phys. Rev. Lett. **85**, 2478.

Peter, E., P. Senellart, D. Martrou, A. Lemaitre, J. Hours, J. M. Gérard, and J. Bloch (2005), Phys. Rev. Lett. **95**, 067401.

Petermann, K. (1979), IEEE J. Quantum Electron. **15**, 566.

Philipp, M., P. von Brentano, G. Pascovici, and A. Richter (2000), Phys. Rev. E **62**, 1922.

Pillay, J. C., Y. Natsume, A. D. Stone, and Y. D. Chong (2014), Phys. Rev. A **89**, 033840.

Podolskiy, V., and E. Narimanov (2003), Phys. Rev. Lett. **91**, 263601.

Podolskiy, V., and E. Narimanov (2005), Opt. Lett. **30**, 474.

Podolskiy, V. A., E. Narimanov, W. Fang, and H. Cao (2004), Proceedings of Nat. Acad. of Sci. USA **101**, 10498.

Poellinger, M., D. O'Shea, F. Warken, and A. Rauschenbeutel (2009), Phys. Rev. Lett. **103**, 053901.

Poli, C., B. Dietz, O. Legrand, F. Mortessagne, and A. Richter (2009), Phys. Rev. E **80**, 035204(R).

Poli, C., G. A. Luna-Acosta, and H.-J. Stöckmann (2012), Phys. Rev. Lett. **108**, 174101.

Poon, A. W., F. Courvoisier, and R. K. Chang (2001), Opt. Lett. **26** (9), 632.

Post, E. J. (1967), Rev. Mod. Phys. **39**, 475.

Potzuweit, A., T. Weich, S. Barkhofen, U. Kuhl, H.-J. Stöckmann, and M. Zworski (2012), Phys. Rev. E **86**, 066205.

Preu, S., S. I. Schmid, F. Sedlmeir, J. Evers, and H. G. L. Schwefel (2013), Opt. Express **21**, 16370.

Qian, S.-X., B. J. Snow, H.-M. Tzeng, and R. K. Chang (1986), Science **231**, 486.

Qiu, M. (2002), Appl. Phys. Lett. **81**, 1163.

Ra, J. W., H. L. Bertoni, and L. B. Felsen (1973), SIAM J. Appl. Math. **24** (3), 396.

Rahachou, A. I., and I. V. Zozoulenko (2003), J. Appl. Phys. **94**, 7929.

Ramilowski, J. A., S. D. Prado, F. Borondo, and D. Farrelly (2009), Phys. Rev. E **80**, 055201(R).

Rayleigh, L. (1945), *The Theory of Sound* (American edition: Dover, New York) first published 1877.

Redding, B., L. Ge, G. S. Solomon, and H. Cao (2012a), Appl. Phys. Lett. **100**, 061125.

Redding, B., L. Ge, Q. H. Song, J. Wiersig, G. S. Solomon, and H. Cao (2012b), Phys. Rev. Lett. **108**, 253902.

Rex, N. B., H. E. Tureci, H. G. L. Schwefel, R. K. Chang, and A. D. Stone (2002), Phys. Rev. Lett. **88**, 094102.

Richens, P. J., and M. V. Berry (1981), Physica D **2**, 495.

Richter, A. (1999), in *Emerging Applications of Number Theory*, Vol. 109, edited by D. A. Heijhal, J. Friedman, M. C. Gutzwiller, and A. M. Odlyzko (Springer, New York) pp. 479–523.

Righini, G. C., Y. Dumeige, P. Feron, M. Ferrari, G. N. Conti, D. Ristic, and S. Soria (2011), RIVISTA DEL NUOVO CIMENTO **34**, 435.

Robnik, M., and M. V. Berry (1985), J. Phys. A **18**, 1361.

Rüter, C. E., K. G. Makris, R. El-Ganainy, D. N. Christodoulides, M. Segev, and D. Kip (2010), Nature Physics **6**, 192.

Ryu, J.-W., and M. Hentschel (2011), Opt. Lett. **36**, 1116.

Ryu, J.-W., and S.-Y. Lee (2011), Phys. Rev. E **83**, 015203(R).

Ryu, J.-W., S.-Y. Lee, C.-M. Kim, and Y.-J. Park (2006), Phys. Rev. E **73**, 036207.

Ryu, J.-W., S.-Y. Lee, and S. W. Kim (2009), Phys. Rev. A **79**, 053858.

Ryu, J.-W., S.-Y. Lee, and S. W. Kim (2012), Phys. Rev. A **85**, 042101.

Ryu, J.-W., S. Rim, Y.-J. Park, C.-M. Kim, and S.-Y. Lee (2008), Phys. Lett. A **372**, 3531.

Sandoghdar, V., F. Treussart, J. Hare, V. Lefèvre-Seguin, J.-M. Raimond, and S. Haroche (1996), Phys. Rev. A **54**, 1777.

Sarma, R., L. Ge, J. Wiersig, and H. Cao (2014), arXiv:1404.5362.

Sarma, R., H. Noh, and H. Cao (2012), J. Opt. Soc. Am. B **29**, 1648.

Schäfer, R., U. Kuhl, and H.-J. Stöckmann (2006), New. J. Phys. **8**, 1.

Scheuer, J. (2007), Opt. Express **15**, 15053.

Scheuer, J., W. M. J. Green, G. A. DeRose, and A. Yariv (2005), IEEE J. Sel. Top. Quantum Electron. **11**, 476.

Schlehahn, A., F. Albert, C. Schneider, S. Höfling, S. Reitzenstein, J. Wiersig, and M. Kamp (2013), Opt. Express **21**, 15951.

Schliesser, A., P. Del'Haye, N. Nooshi, K. J. Vahala, and T. J. Kippenberg (2006), Phys. Rev. Lett. **97**, 243905.

Schomerus, H. (2009), Phys. Rev. A **79**, 061801(R).

Schomerus, H. (2010), Phys. Rev. Lett. **104**, 233601.

Schomerus, H. (2013), Proc. R. Soc. Lond. A **371**, 20120194.

Schomerus, H., K. M. Frahm, M. Patra, and C. W. J. Beenakker (2000), Physica A **278**, 469.

Schomerus, H., and M. Hentschel (2006), Phys. Rev. Lett. **96**, 243903.

Schomerus, H., and J. Tworzydlo (2004), Phys. Rev. Lett. **93**, 154102.

Schomerus, H., J. Wiersig, and M. Hentschel (2004), Phys. Rev. A **70**, 012703.

Schomerus, H., J. Wiersig, and J. Main (2009), Phys. Rev. A **79**, 053806.

Schwefel, H. G. L. (2004), *Directionality and Vector Resonances of Regular and Chaotic Dielectric Microcavities*, Ph.D. thesis (Yale University).

Schwefel, H. G. L., N. B. Rex, H. E. Tureci, R. K. Chang, A. D. Stone, T. Ben-Messaoud, and J. Zyss (2004), J. Opt. Soc. Am. B **21**, 923.

Shainline, J., S. Elston, Z. Liu, G. Fernandes, R. Zia, and J. Xu (2009), Opt. Express **17**, 23323.

Shao, L., X.-F. Jiang, X.-C. Yu, B.-B. Li, W. R. Clements, F. Vollmer, W. Wang, Y.-F. Xiao, and Q. Gong (2013), Adv. Mater. **25**, 5616.

Shepelyansky, D. L. (2008), Phys. Rev. E **77**, 015202(R).

Shim, J.-B., A. Eberspächer, and J. Wiersig (2013), New. J. Phys. **15**, 113058.

Shim, J.-B., A. Eberspächer, J. Wiersig, J. Unterhinninghofen, Q. H. Song, L. Ge, H. Cao, and A. D. Stone (2012), in *Quantum optics with semiconductor nanostructures*, edited by F. Jahnke (Woodhead Publishing) pp. 225–251.

Shim, J.-B., S.-B. Lee, S. W. Kim, S.-Y. Lee, J. Yang, S. Moon, J.-H. Lee, and K. An (2008), Phys. Rev. Lett. **100**, 174102.

Shim, J.-B., and J. Wiersig (2013), Opt. Express **21**, 24240.

Shim, J.-B., J. Wiersig, and H. Cao (2011), Phys. Rev. E **84**, 035202(R).

Shinohara, S., T. Fukushima, and T. Harayama (2008), Phys. Rev. A **77**, 033807.

Shinohara, S., and T. Harayama (2007), Phys. Rev. E **75**, 036216.

Shinohara, S., and T. Harayama (2011), in *Trends in Nano- and Micro-Cavities*, edited by O. Kwon, B. Lee, and K. An (Bentham Books, Sharjah) pp. 62–108.

Shinohara, S., T. Harayama, and T. Fukushima (2011a), Opt. Lett. **36**, 1023.

Shinohara, S., T. Harayama, T. Fukushima, M. Hentschel, T. Sasaki, and E. E. Narimanov (2010), Phys. Rev. Lett. **104**, 163902.

Shinohara, S., T. Harayama, T. Fukushima, M. Hentschel, S. Sunada, and E. E. Narimanov (2011b), Phys. Rev. A **83**, 053837.

Shinohara, S., M. Hentschel, J. Wiersig, T. Sasaki, and T. Harayama (2009), Phys. Rev. A **80**, 031801(R).

Shiozawa, T. (1973), Proceedings OF The IEEE **61**, 1694.

Shudo, A., and K. S. Ikeda (1995), Phys. Rev. Lett. **74**, 682.

Shudo, A., and K. S. Ikeda (2012), Phys. Rev. Lett. **109**, 154102.

Siegman, A. E. (1986), *Lasers* (University Science Books, Sausalito, CA).

Sirko, L., S. Bauch, Y. Hlushchuck, P. M. Koch, R. Blümel, M. Barth, U. Kuhl, and H.-J. Stöckmann (2000), Phys. Lett. A **266**, 331.

Sjöstrand, J. (1990), Duke Math. **60**, 1.

Slusher, R. E., A. F. J. Levi, U. Mohideen, S. L. McCall, S. J. Pearton, and R. A. Logan (1993), Appl. Phys. Lett. **63**, 1310.

Smotrova, E. I., A. I. Nosich, T. M. Benson, and P. Sewell (2005), IEEE J. Sel. Top. Quantum Electron. **11**, 1135.

Soltani, M., S. Yegnanarayanan, and A. Adibi (2007), Opt. Express **15**, 4694.

Song, Q. H., and H. Cao (2010), Phys. Rev. Lett. **105**, 053902.

Song, Q. H., H. Cao, S. T. Ho, and G. S. Solomon (2009a), Appl. Phys. Lett. **94**, 061109.

Song, Q. H., W. Fang, B. Liu, S. T. Ho, G. S. Solomon, and H. Cao (2009b), Phys. Rev. A **80**, 041807(R).

Song, Q. H., L. Ge, B. Redding, and H. Cao (2012), Phys. Rev. Lett. **108**, 243902.

Song, Q. H., L. Ge, A. D. Stone, H. Cao, J. Wiersig, J.-B. Shim, J. Unterhinninghofen, W. Fang, and G. S. Solomon (2010), Phys. Rev. Lett. **105**, 103902.

Song, Q. H., L. Ge, J. Wiersig, and H. Cao (2013a), Phys. Rev. A **88**, 023834.

Song, Q. H., L. Ge, J. Wiersig, J.-B. Shim, J. Unterhinninghofen, A. Eberspächer, W. Fang, G. S. Solomon, and H. Cao (2011), Phys. Rev. A **84**, 063843.

Song, Q. H., C. Zeng, and S. Xiao (2013b), Phys. Rev. A **87**, 013831.

Spillane, S. M., T. J. Kippenberg, O. J. Painter, and K. J. Vahala (2003), Phys. Rev. Lett. **91**, 043902.

Spillane, S. M., T. J. Kippenberg, and K. J. Vahala (2002), Nature **415**, 621.

Srinivasan, K., M. Borselli, T. J. Johnson, P. Barclay, O. Painter, A. Stintz, and S. Krishna (2005), Appl. Phys. Lett **86**, 151106.

Srinivasan, K., M. Borselli, O. Painter, A. Stintz, and S. Krishna (2006), Opt. Express **14**, 1094.

Srinivasan, K., and O. Painter (2006), Nature **450**, 862.

Starykh, O. A., P. R. J. Jacquod, E. E. Narimanov, and A. D. Stone (2000), Phys. Rev. E **62**, 2078.

Stöckmann, H.-J. (2000), *Quantum Chaos* (Cambridge University Press, Cambridge, UK).

Stone, A. D. (2001), Physica Scripta **T90**, 248.

Strelow, C., C. M. Schultz, H. Rehberg, M. Sauer, H. Welsch, A. Stemmann, C. Heyn, D. Heitmann, and T. Kipp (2012), Phys. Rev. B **85**, 155329.

Sumetsky, M., Y. Dulashko, and R. S. Windeler (2010), Opt. Lett. **35**, 898.

Sunada, S., and T. Harayama (2006), Phys. Rev. A **74**, 021801(R).

Sunada, S., and T. Harayama (2007), Opt. Express **15**, 16245.

Symes, R., R. M. Sayer, and J. P. Reid (2004), Phys. Chem. Chem. Phys. **6**, 474.

Taflove, A., and S. C. Hagness (2000), *Computational Electrodynamics the Finite-Difference Time-Domain Method* (Artech House, London).

Tamboli, A. C., E. D. Haberer, R. Sharma, K. W. Lee, S. Nakamura, and E. L. Hu (2007), Nature Photonics **1**, 61.

Tanaka, T., M. Hentschel, T. Fukushima, and T. Harayama (2007), Phys. Rev. Lett. **98**, 033902.

Tessarek, C., G. Sarau, M. Kiometzis, and S. Christiansen (2013), Opt. Express **21**, 2733.

Tomsovic, S., and D. Ullmo (1994), Phys. Rev. E **50** (1), 145.

Tran, N. H., L. Dutriaux, P. Balcou, A. Le Floch, and F. Bretenaker (1995), Opt. Lett. **20** (11), 1233.

Tureci, H. E., H. G. L. Schwefel, P. Jacqoud, and A. D. Stone (2005), Prog. Opt. **47**, 75.

Tureci, H. E., H. G. L. Schwefel, A. D. Stone, and E. E. Narimanov (2002), Opt. Express **10** (16), 752.

Tureci, H. E., and A. D. Stone (2002), Opt. Lett. **27**, 7.

Tzeng, H.-M., K. F. Wall, M. B. Long, and R. K. Chang (1984), Opt. Lett. **9** (11), 499.

Unterhinninghofen, J. (2011), *Ray-wave correspondence and extended ray dynamics in optical microcavities*, PhD thesis (Otto-von-Guericke-Universität Magdeburg).

Unterhinninghofen, J., U. Kuhl, J. Wiersig, H.-J. Stöckmann, and M. Hentschel (2011), New J. Phys. **13**, 023013.

Unterhinninghofen, J., and J. Wiersig (2010), Phys. Rev. E **82**, 026202.

Unterhinninghofen, J., J. Wiersig, and M. Hentschel (2008), Phys. Rev. E **78**, 016201.

Vahala, K. J. (2003), Nature (London) **424**, 839.

Vahala, K. J. (2004), *Optical Microcavities*, Advanced Series in applied Physics, Vol. 5 (World Scientific, Singapore).

Vant, K., G. Ball, H. Ammann, and N. Christensen (1999), Phys. Rev. E **59**, 2846.

Vietze, U., O. Kraus, F. Laeri, G. Ihlein, G. Schüth, B. Limburg, and M. Abraham (1998), Phys. Rev. Lett. **81**, 4628.

Vollmer, F., and S. Arnold (2008), Nature Methods **5**, 591.

Vollmer, F., S. Arnold, and D. Keng (2008), Proceedings of Nat. Acad. of Sci. USA **105**, 20701.

Wang, D., H. W. Seo, C.-C. Tin, M. J. Bozack, J. R. Williams, and M. Park (2006), J. Appl. Phys. **99**, 093112.

Wang, Q. J., C. Yan, L. Diehl, M. Hentschel, J. Wiersig, N. Yu, C. Pflügl, M. A. Belkin, T. Edamura, M. Yamanishi, H. Kan, and F. Capasso (2009), New J. Phys. **11**, 125018.

Wang, Q. J., C. Yan, N. Yu, J. Unterhinninghofen, J. Wiersig, C. Pflügl, L. Diehl, T. Edamura, M. Yamanishi, H. Kan, and F. Capasso (2010), Proceedings of Nat. Acad. of Sci. USA **107**, 22407.

Weich, T., S. Barkhofen, U. Kuhl, C. Poli, and H. Schomerus (2014), New J. Phys. **16**, 033029.

Wiersig, J. (2000), Phys. Rev. E **62** (1), R21.

Wiersig, J. (2001), Phys. Rev. E **64**, 026212.

Wiersig, J. (2002), Phys. Rev. E **65**, 046217.

Wiersig, J. (2003a), J. Opt. A: Pure Appl. Opt. **5**, 53.

Wiersig, J. (2003b), Phys. Rev. A **67**, 023807.

Wiersig, J. (2006), Phys. Rev. Lett. **97**, 253901.

Wiersig, J. (2008), Opt. Express **16**, 5874.

Wiersig, J. (2011), Phys. Rev. A **84**, 063828.

Wiersig, J. (2012), Phys. Rev. A **85**, 063838.

Wiersig, J. (2014a), Phys. Rev. A **89**, 012119.

Wiersig, J. (2014b), Phys. Rev. Lett. **112**, 203901.

Wiersig, J., A. Eberspächer, J.-B. Shim, J.-W. Ryu, S. Shinohara, M. Hentschel, and H. Schomerus (2011a), Phys. Rev. A **84**, 023845.

Wiersig, J., and M. Hentschel (2006), Phys. Rev. A **73**, 031802(R).

Wiersig, J., and M. Hentschel (2008), Phys. Rev. Lett. **100**, 033901.

Wiersig, J., S. W. Kim, and M. Hentschel (2008), Phys. Rev. A **78**, 053809.

Wiersig, J., and J. Main (2008), Phys. Rev. E **77**, 036205.

Wiersig, J., J. Unterhinninghofen, H. Schomerus, U. Peschel, and M. Hentschel (2010), Phys. Rev. A **81**, 023809.

Wiersig, J., J. Unterhinninghofen, Q. H. Song, H. Cao, M. Hentschel, and S. Shinohara (2011b), in *Trends in Nano- and Micro-Cavities*, edited by O. Kwon, B. Lee, and K. An (Bentham Books, Sharjah) pp. 109–152.

Wilde, F. (2008), *Unidirectional photoluminescence emission of pierced microdisks*, PhD thesis (Universität Hamburg).

Wisniacki, D., and G. G. Carlo (2008), Phys. Rev. E **77**, 045201(R).

Wysin, G. M. (2005), J. Opt. A: Pure Appl. Opt. **7**, 502.

Xiao, Y. F., C. H. Dong, Z. F. Han, G. C. Guo, and Y. S. Park (2007), Opt. Lett. **32**, 644.

Xiao, Y. F., C. H. Dong, C. F. Zou, Z. F. Han, L. Yang, and G. C. Guo (2009), Opt. Lett. **34**, 509.

Xiao, Y.-F., X.-F. Jiang, Q.-F. Yang, L. Wang, K. Shi, Y. Li, and Q. Gong (2013), Laser Photonics Rev. **7**, L51.

Xiao, Y.-F., C.-L. Zou, Y. Li, C.-H. Dong, Z.-F. Han, and Q. Gong (2010), Front. Optoelectron. China **3**, 109.

Yan, C., Q. J. Wang, L. Diehl, M. Hentschel, J. Wiersig, N. Yu, Pfügel, F. Capasso, M. A. Belkin, T. Edamura, M. Yamanishi, and H. Kan (2009), Appl. Phys. Lett. **94**, 251101.

Yang, J., S.-B. Lee, S. Moon, S.-Y. Lee, S. W. Kim, T. T. A. Dao, J.-H. Lee, and K. An (2010), Phys. Rev. Lett. **104**, 243601.

Yang, J., S.-B. Lee, J.-B. Shim, S. Moon, S.-Y. Lee, S. W. Kim, J.-H. Lee, and K. An (2008), Appl. Phys. Lett. **93**, 061101.

Yang, J., S. Moon, S.-B. Lee, J.-H. Lee, K. An, J.-B. Shim, H.-W. Lee, and S. W. Kim (2006), Rev. Sci. Intrum. **77**, 083103.

Yang, L., D. K. Armani, and K. J. Vahala (2003), Appl. Phys. Lett. **83**, 825.

Yang, Y.-D., and Y.-Z. Huang (2007), IEEE J. Quantum Elect. **43**, 497.

Yang, Y.-D., S.-J. Wang, and Y.-Z. Huang (2009), Opt. Express **17**, 23010.

Yariv, A. (2000), Electron. Lett. **36**, 321.

Yi, C.-H., M.-W. Kim, and C.-M. Kim (2009), Appl. Phys. Lett. **95**, 141107.

Yi, C.-H., S. H. Lee, M.-W. Kim, J. Cho, J. Lee, S.-Y. Lee, J. Wiersig, and C.-M. Kim (2011), Phys. Rev. A **84**, 041803.

Yoo, G., H.-S. Sim, and H. Schomerus (2011), Phys. Rev. A **84**, 063833.

Yu, D., Y. Chen, B. Li, X. Chen, M. Zhang, F. Zhao, and S. Ren (2007), Appl. Phys. Lett. **91**, 091116.

Zhang, Z., L. Yang, T. Hong, K. Vahala, and A. Scherer (2007a), Appl. Phys. Lett **90**, 111119.

Zhang, Z., L. Yang, V. Liu, T. Hong, K. J. Vahala, and A. Scherer (2007b), Appl. Phys. Lett. **90**, 111119.

Zhou, L.-M., C.-L. Zou, Z.-F. Han, G.-C. Guo, and F.-W. Sun (2011), Opt. Lett. **36**, 624.

Zhu, G. P., C. X. Xu, J. Zhu, C. G. Lv, and Y. P. Cu (2009), Appl. Phys. Lett. **94**, 051106.

Zhu, J., Ş. K. Özdemir, L. He, and L. Yang (2010), Opt. Express **18**, 23535.

Zou, C.-L., H. G. L. Schwefel, F.-W. Sun, Z.-F. Han, and G. Guo (2011), Opt. Express , 15669.

Zou, C. L., F. W. Sun, C. H. Dong, F. J. Shu, X. W. Wu, J. M. Cui, Y. Yang, Z. F. Han, and G. C. Guo (2013), IEEE J. Sel. Top. Quantum Electron. **19**, 9000406.

Zworski, M. (1999), Inv. Math. **136**, 353.

FIGURES

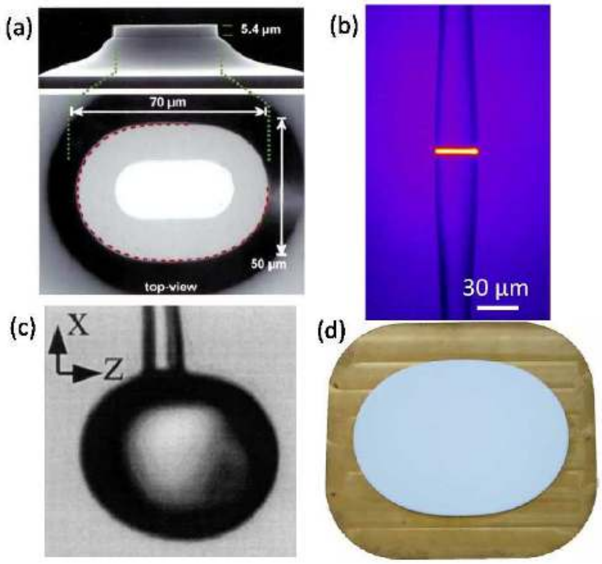

FIG. 1 (Color online) A few examples of deformed dielectric cavities. (a) Side-view and top-view scanning electron microscope (SEM) images of a quantum cascade laser made of a flattened quadrupolar-shaped GaAs cylinder. From (Gmachl *et al.*, 1998). (b) Optical image of a liquid microjet which traps light on one cross section by total internal reflection from the liquid-air interface. Image courtesy of Kyungwon An, Seoul National University. (c) Optical image of a deformed fused-silica sphere with the long axis equal to 200 μm. From (Lacey and Wang, 2001). (d) Photo of a microwave cavity made of a Teflon disc on a brass ground plate with dimensions 380 mm × 260 mm. From (Schäfer *et al.*, 2006).

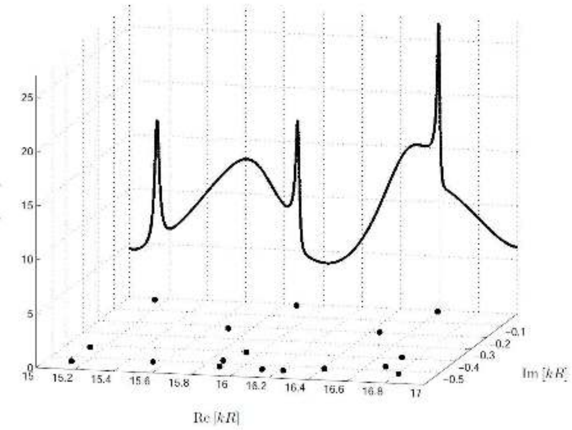

FIG. 2 Resonances and long-lived optical modes. The back panel shows the intensity scattered off a dielectric circular disk of radius R and refractive index $n = 1.5$ at 170° with respect to the incoming plane wave with wave number $k = \omega/c$, where c is the speed of light in vacuum. The scattering intensity shows narrow peaks (resonances) at the scaled complex frequencies $\Omega = \omega R/c = kR$ which are closest to the real axis. These are the frequencies of the long-lived modes; the short-lived modes contribute to broader peaks and the scattering background. From (Tureci *et al.*, 2005).

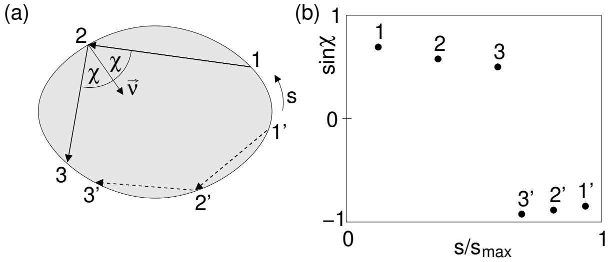

FIG. 3 Illustration of ray dynamics in a billiard; s is the arclength coordinate along the boundary of the cavity and χ is the angle of incidence with respect to the boundary normal $\vec{\nu}$. (a) The solid line $1 \to 2 \to 3$ is a counterclockwise traveling ray in real space and the dashed line $1' \to 2' \to 3'$ is a clockwise traveling ray. (b) The same dynamics in the Poincaré surface of section. The coordinate s is normalized to the total circumference of the boundary $s_{\max}$. In this representation the angle χ is conventionally defined negative for clockwise traveling rays.

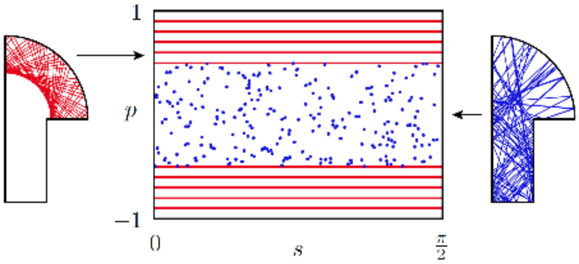

FIG. 4 (Color online) Example of a simple mixed phase space. Numerically computed Poincaré surface of section for a desymmetrized mushroom billiard showing regular and chaotic regions in phase space; the size of the billiard is scaled such that $s_{\max} = \pi/2$. From (Bäcker *et al.*, 2008a).

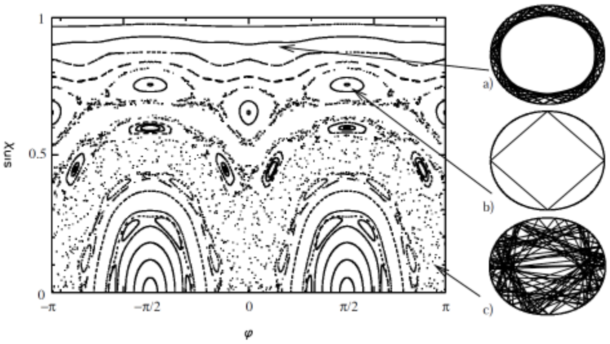

FIG. 5 Poincaré surface of section of a quadrupole billiard (12) for $\varepsilon = 0.072$. The boundary is here parametrized by the polar angle φ. The direction $\varphi = 0$ corresponds to the right part of the horizontal axis in the three real space plots. From (Tureci *et al.*, 2002).

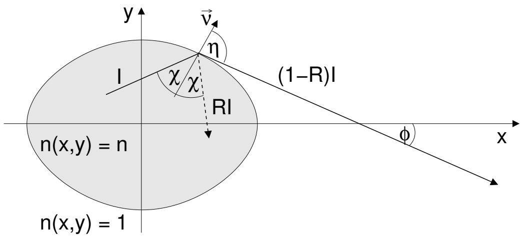

FIG. 6 Refractive escape from a dielectric cavity with refractive index $n > 1$. A ray with intensity I is split into a reflected ray with intensity $R^{\mathrm{TM,TE}}I$ and a transmitted ray with intensity $(1 - R^{\mathrm{TM,TE}})I$. $\vec{\nu}$ is the outward normal vector. The angle of the reflected ray η is related to the angle of the incident ray χ by Snell's law. The emission direction can be described by the polar angle φ which equals asymptotically the angle ϕ between the x-axis and the emitted ray.

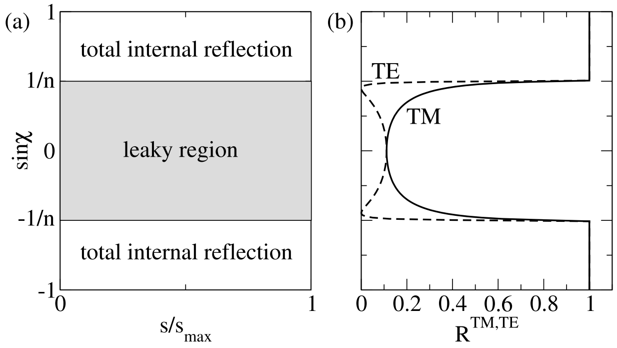

FIG. 7 The leaky region in phase space of a dielectric cavity. (a) Poincaré surface of section with leaky region $|\sin\chi| \leq 1/n$ in which the condition for total internal reflection is not met. (b) Reflection coefficient $R^{\mathrm{TM,TE}}(\sin\chi)$ for a planar dielectric interface with the incident plane wave coming from the high-index medium ($n = 2$). The low-index medium is air with $n = 1$.

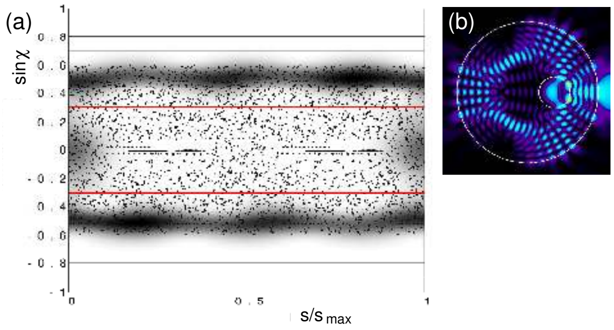

FIG. 8 (Color online) Husimi function in phase space. (a) Poincaré surface of section (dots, horizontal lines with $|\sin\chi| > 0.6$), critical lines (horizontal lines with $|\sin\chi| \approx 0.3$), and emerging Husimi function (shaded regions) of a mode in an annular cavity. (b) Mode in real space.

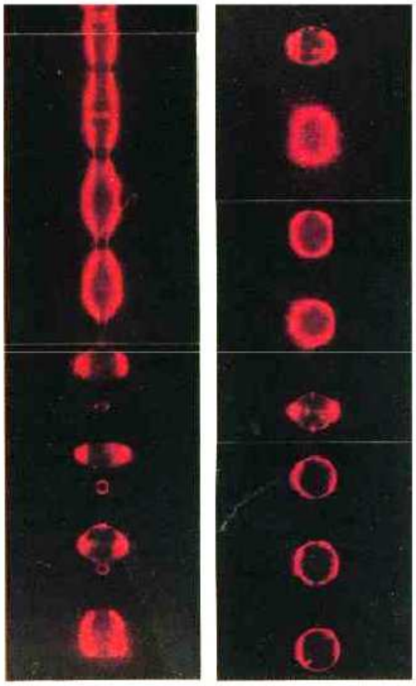

FIG. 9 (Color online) A series of photographs of laser emission from the droplet stream within the first few millimeters of the vibrating orifice. (Left) The upper portion of the stream showing the periodically perturbed, continuously connected liquid cylinder and the development of separate, highly distorted droplets. (Right) The lower portion of the stream, showing the transition from oscillating prolate-to- oblate spheroids to a stream of monodisperse, equally spaced spherical droplets. From (Qian *et al.*, 1986).

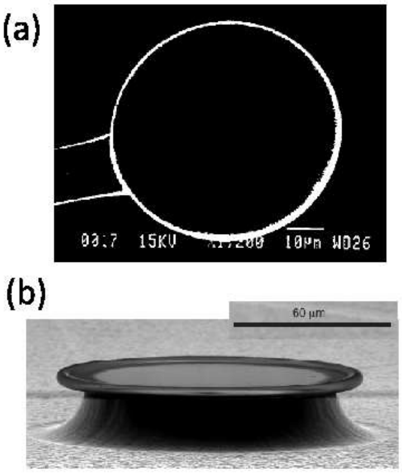

FIG. 10 (a) Scanning electron micrograph (SEM) of a silica microsphere at the end of the preform wire. Its diameter is 70 μm. No surface defect was observed on a 30 nm scale. From (Collot *et al.*, 1993). (b) SEM of a silica microtoroid. From (Armani *et al.*, 2003).

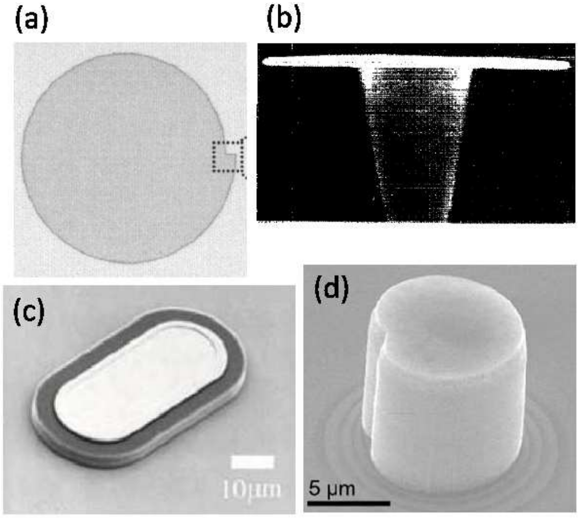

FIG. 11 (a) Optical microscope image of a spiral microcavity made of a DCM-doped polysmethylmethacrylated film. From (Ben-Messaoud and Zyss, 2005). (b) Side-view SEM of a InGaAsP microdisk on top of an InP pedestal. The disk diameter is 3 μm. From (McCall *et al.*, 1992). (c) SEM of a GaAs/AlGaAs microstadium laser with an metal electrode on the top for current injection. From (Fukushima and Harayama, 2004). (d) SEM of a limaçon-shaped micropillar with a vertical cavity formed by two Bragg mirrors. Image courtesy of S. Reitzenstein, TU Berlin.

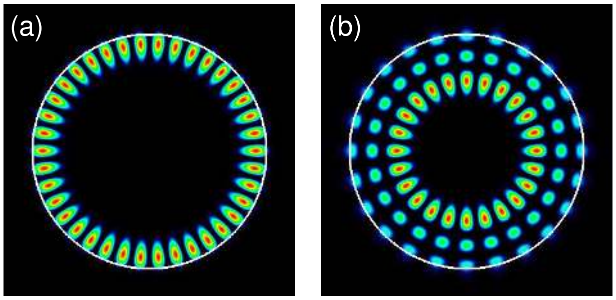

FIG. 12 (Color online) Numerically computed standing wave modes in a dielectric microdisk; $n = 3.3$ (GaAs), TM polarization. (a) Radial mode number $l = 1$ and azimuthal mode number $m = 19$, scaled frequency $\Omega = kR = 7.02783 - i2.99188 \cdot 10^{-13}$; (b) $l = 3$, $m = 12$, and $\Omega = 7.0175 - i6.29188 \cdot 10^{-5}$.

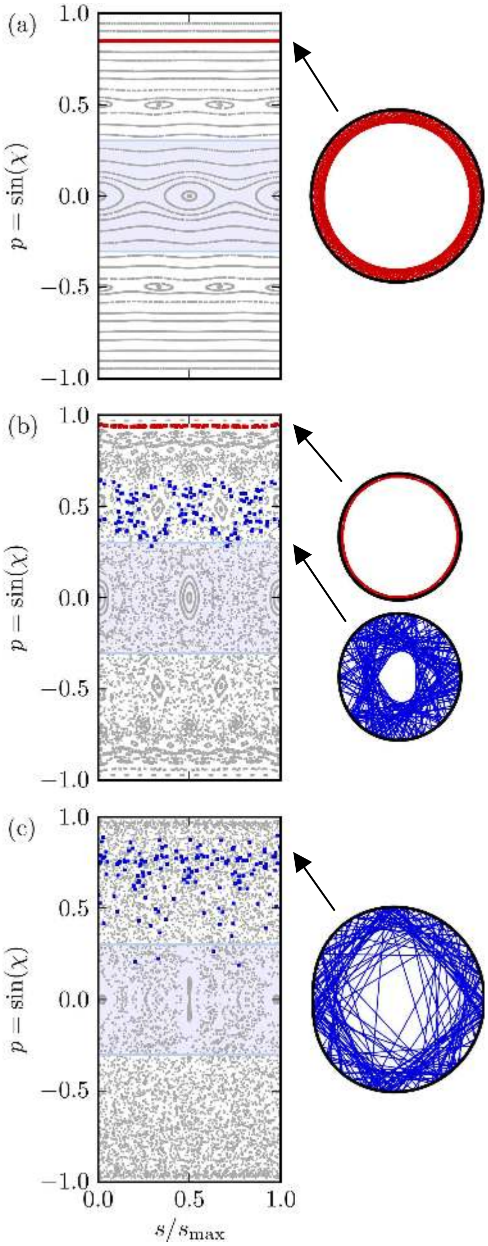

FIG. 13 (Color online) Kolmogorov-Arnol′d-Moser transition to chaos in the limaçon cavity (23). The left-hand side shows the Poincaré surface of section for parameter $\varepsilon = 0.1$ (a), $\varepsilon = 0.3$ (b), $\varepsilon = 0.43$ (c). The shaded region indicate the leaky region for $n = 3.3$. The right-hand side shows the marked trajectories in real space.

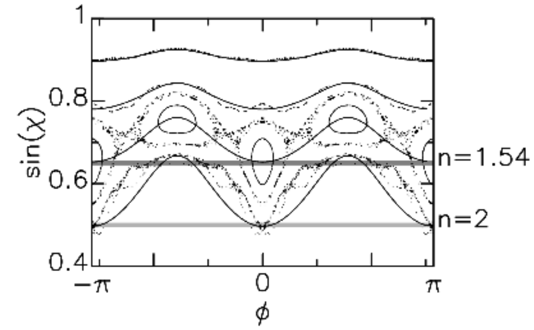

FIG. 14 Four chaotic whispering gallery rays in the phase space of the quadrupole billiard (12) for $\varepsilon = 0.072$ followed for 100-200 reflections. Superimposed are the adiabatic curves (24) for different values of α. The thick lines mark the border of the leaky region for two different refractive indices n. From (Nöckel *et al.*, 1996).

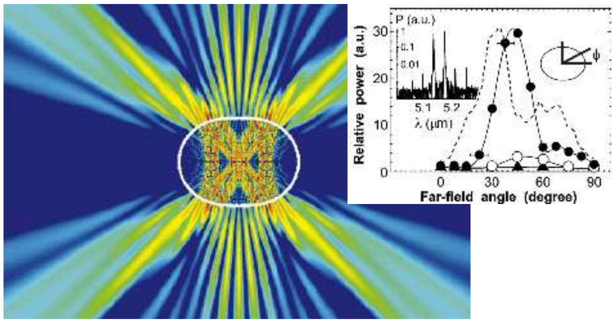

FIG. 15 (Color online) Calculated bowtie mode localized on a stable periodic orbit in a flattened quadrupole (25) with TM polarization, refractive index $n = 3.3$ and deformation parameter $\varepsilon = 0.15$. Inset: measured far-field pattern for $\varepsilon = 0$ (triangles), $\varepsilon = 0.14$ (open circles), and $\varepsilon = 0.16$ (filled circles) compared to calculated data for $\varepsilon = 0.15$ (dashed line). Adapted from (Gmachl *et al.*, 1998).

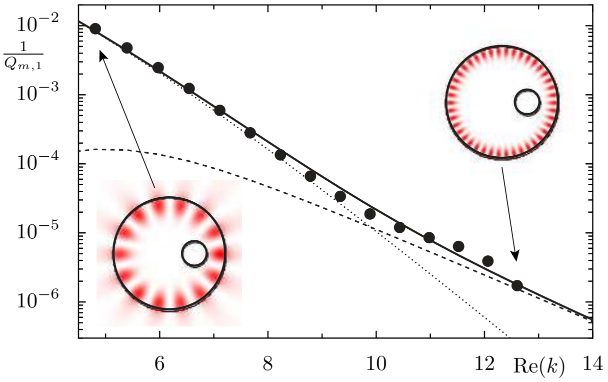

FIG. 16 (Color online) Quality factors and dynamical tunneling rates for the annular microcavity. Shown is the theoretical prediction (solid curve) which is the sum of the direct tunneling contribution (dotted curve) and the dynamical tunneling contribution (dashed curve) based on the fictitious integrable system, and numerical data (filled circles) for azimuthal mode number $m = 7, \dots, 21$. From (Bäcker *et al.*, 2009).

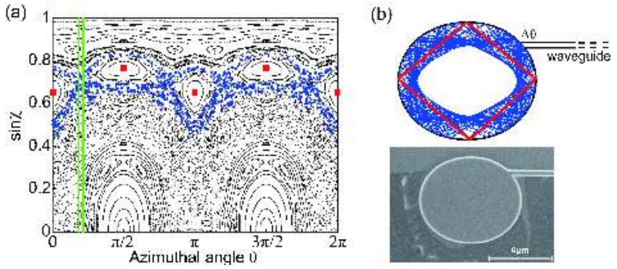

FIG. 17 (Color online) Using chaos-assisted tunneling for channeling rays into waveguides for efficient collection of light emission from microcavities. (a) Poincaré surface of section of a quadruple billiard, Eq. (12), at $\varepsilon = 0.08$. Red squares mark a period-4 orbit in the center of an island chain. Blue dots indicate a typical chaotic trajectory out of the island chain. Vertical lines mark the exit window due to the attached waveguide. (b) Real space representation of the period-4 orbit and the chaotic trajectory. Inset: scanning electron microscope image of the experimental realization (Song *et al.*, 2012).

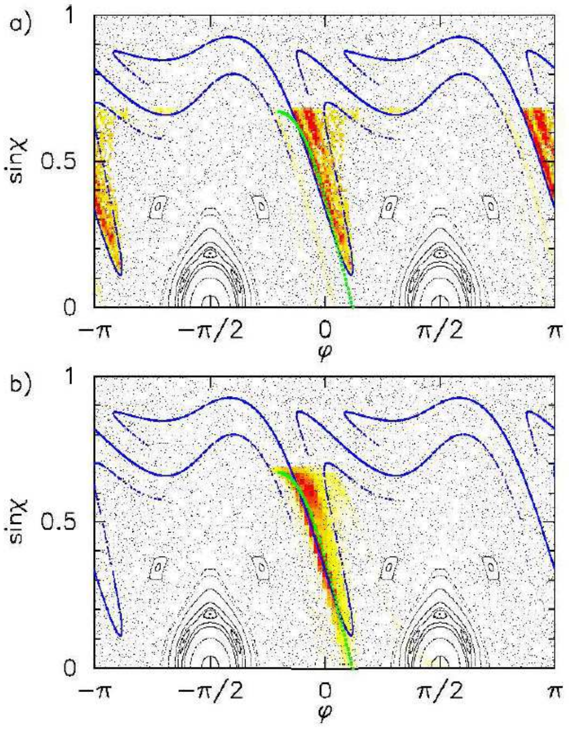

FIG. 18 (Color online) Light emission along unstable manifolds of short periodic orbits. (a) Emitted-ray intensity (color scale) overlaid on the Poincaré surface of section of the quadruple cavity for $\varepsilon = 0.18$, Eq. (12), and refractive index $n = 1.49$. The blue curve is the unstable manifold of a rectangular periodic orbit. (b) Experimental far-field data (color scale) projected onto the Poincaré surface of section (available data is restricted to $\varphi \in [-\pi/2, \pi/2]$). From (Schwefel *et al.*, 2004).

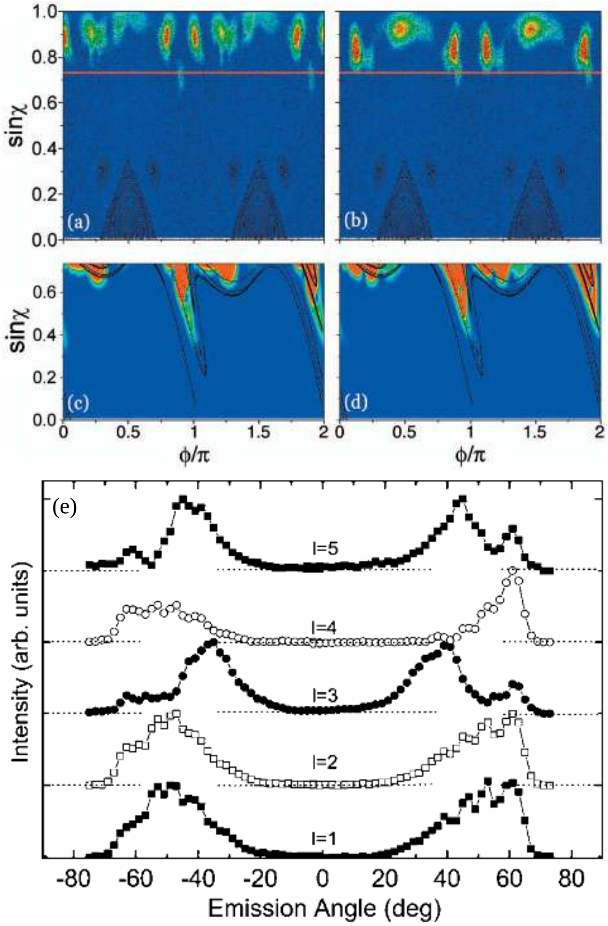

FIG. 19 (Color online) Light emission along the unstable manifold of the chaotic saddle. (a) and (b) Calculated Husimi functions of two different modes in the quadruple cavity (12) for $\varepsilon = 0.16$ and refractive index $n = 1.361$. The leaky region below the critical line $\sin\chi_c = 1/n$ (red horizontal line) is magnified in (c) and (d), respectively. Superimposed is the unstable manifold of the chaotic saddle. (e) Measured far-field pattern of individual modes in a liquid-jet cavity of the same shape and refractive index as in (a)-(d). Adapted from (Lee *et al.*, 2007c).

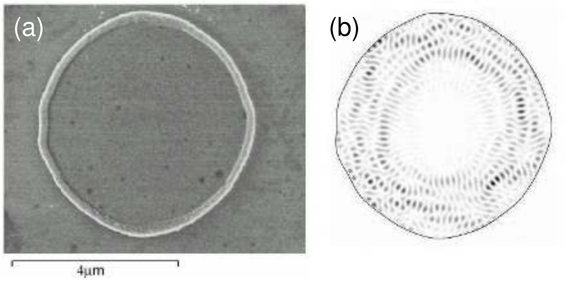

FIG. 20 Dynamical localization in optical microcavities with strong boundary roughness. (a) Scanning electron microscope image of rough microdisk (Podolskiy *et al.*, 2004). (b) Computed high-Q mode dynamically localized in angular momentum space.

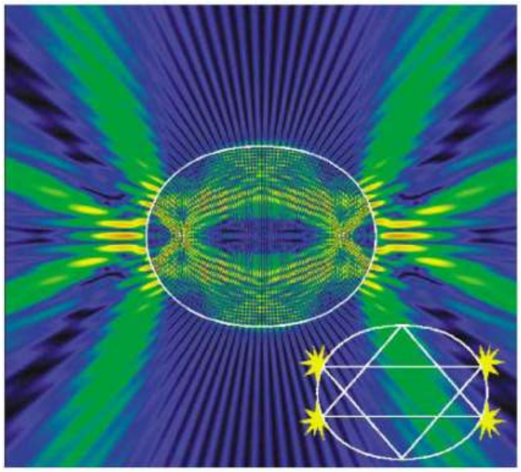

FIG. 21 (Color online) Scarring in optical microcavities. Computed optical mode in the quadruple cavity (12) which is scarred by the triangular periodic ray trajectories depicted in the inset; $\varepsilon = 0.12$ and refractive index $n = 2.65$. From (Rex *et al.*, 2002).

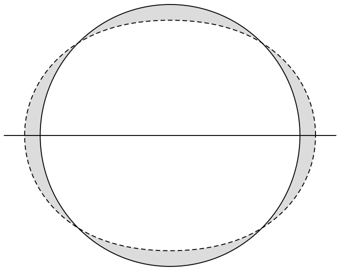

FIG. 22 Illustration for the perturbation theory of deformed microdisk cavities. Circle (solid curve) and a deformed circle (dashed). The horizontal line represents a symmetry axis. Grey regions mark the area δa where the refractive index of the deformed cavity differs from the one of the circular cavity.

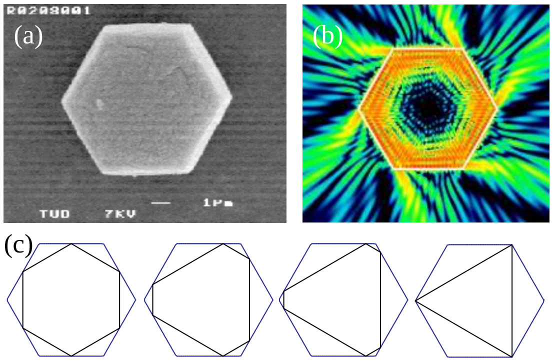

FIG. 23 (Color online) Hexagonal-shaped microcavities. (a) Scanning electron microscope image of a zeolitic aluminophosphate-microcavity. (b) Computed mode structure. (c) Four members of the family of periodic-6 ray trajectories. The ray picture breaks down for the rightmost orbit which hits the corners of the hexagon. Adapted from (Braun *et al.*, 2000).

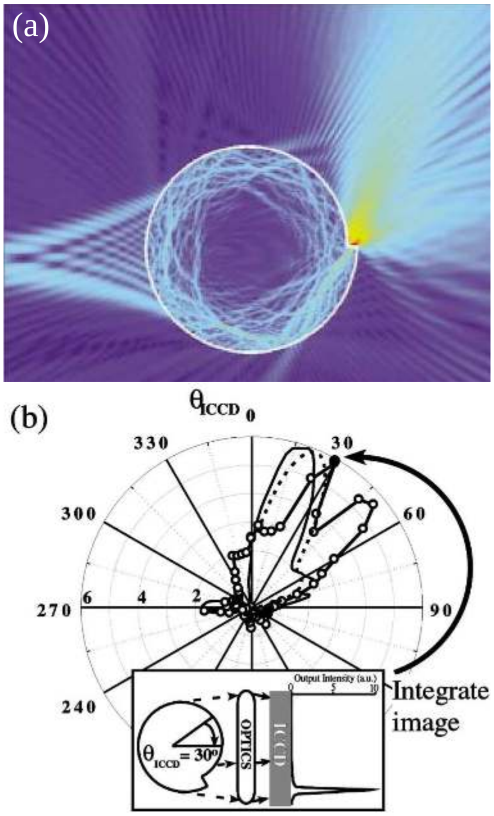

FIG. 24 (Color online) (a) Calculated optical mode in the spiral (41) with $\varepsilon = 0.1$, $n = 2.6$, and $nkR \approx 200$. (b) Experimental (open circles) and calculated (solid and dashed) far-field pattern. Reproduced with permission from (Chern *et al.*, 2003). Copyright 2003, AIP Publishing LLC.

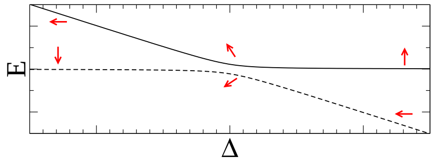

FIG. 25 (Color online) Illustration of an avoided crossing of two energy levels $E_{\pm}(\Delta)$ in a closed system. Equation (43) has been used with E_1 being linear dependent on the parameter Δ, whereas E_2 and $V = W^*$ are kept constant. The arrows visualize the eigenvectors for certain values of Δ.

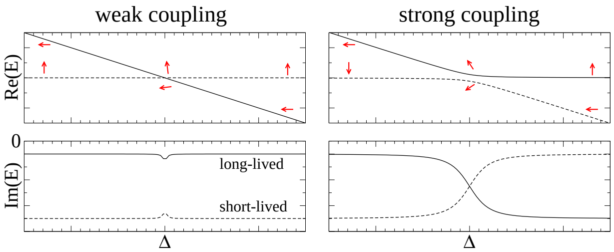

FIG. 26 (Color online) Illustration of an avoided resonance crossing in the weak (left) and strong (right) coupling regime in the case of internal coupling. Small (large) $|\mathrm{Im}(E)|$ corresponds to a long (short) lifetime. The arrows indicate eigenvectors of the system which hybridize near the region of resonant coupling.

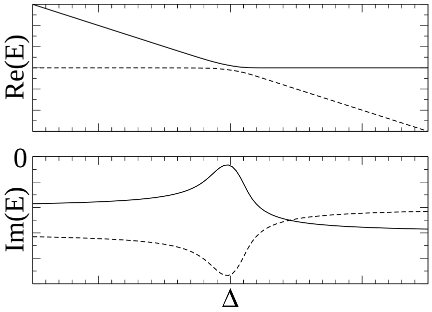

FIG. 27 Illustration of an avoided resonance crossing in the strong coupling regime for the case of external coupling. The resonant formation of a long-lived mode moving close to the real energy axis can be clearly seen.

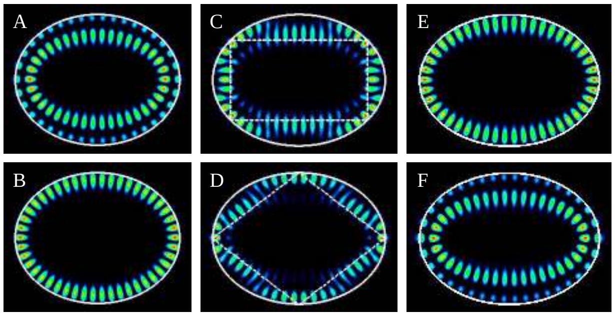

FIG. 28 (Color online) Calculated near field intensity of modes in a dielectric ellipse with refractive index $n = 3.3$. Modes A and B (E and F) are on the left (right) hand side of an avoided crossing. The rectangular-shaped mode C and the diamond-shaped mode D at the center of the avoided crossing show a localization of intensity along periodic ray trajectories (dashed lines). From Unterhinninghofen *et al.* (2008).

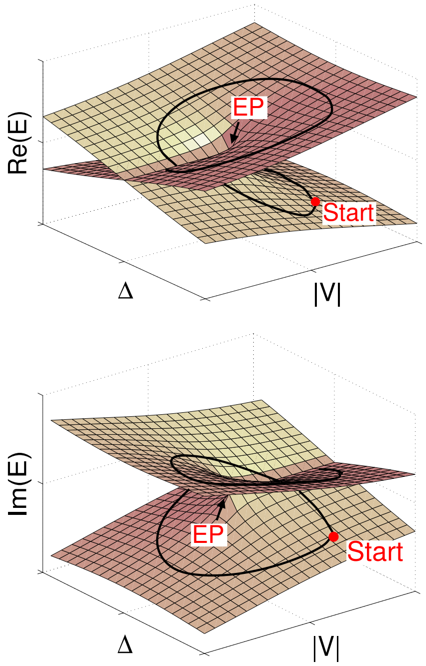

FIG. 29 (Color online) Complex-square-root topology of eigenvalue surfaces $E = E_{\pm}(\Delta, |V|)$ with a branch point singularity at the exceptional point (EP). The black curves result from a double loop in the parameter space $(\Delta, |V|)$.

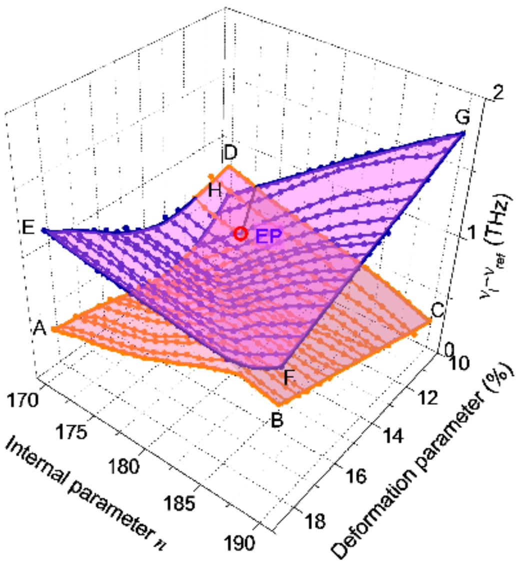

FIG. 30 (Color online) Measured eigenfrequency surfaces $\nu_l - \nu_{\mathrm{ref}}$ of modes in a smoothly deformed liquid-jet microcavity near an exceptional point (EP). The two independent parameters consists of a deformation parameter and a quasicontinuous internal parameter, the mode number n. From Lee *et al.* (2009a).

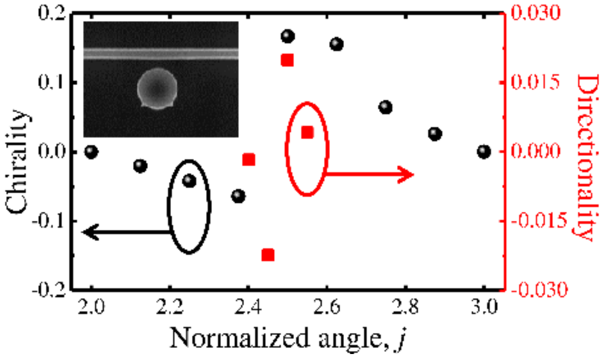

FIG. 31 (Color online) Chirality of a mode in a microdisk perturbed by two small bumps. The disk is optically excited and the directionality of the light outcoupled to a waveguide is measured (squares) as function of the normalized angle between the bumps. Positive (negative) values mean transmission mainly to the left (right) indicating a finite chirality of the excited mode. The calculated chirality shown as circles is positive (negative) for mainly counter-clockwise (clockwise) rotation of the mode. Inset: SEM of the perturbed microdisk with the coupling waveguide. From Kim *et al.* (2014).

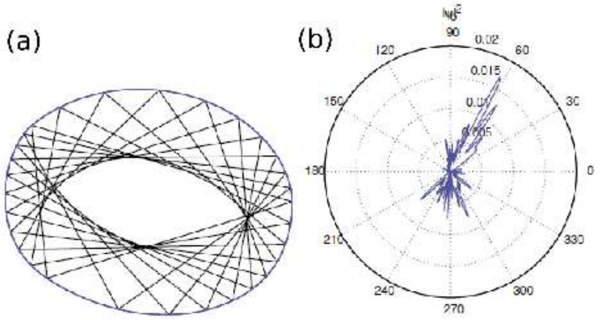

FIG. 32 (Color online) (a) Family of interior whispering-gallery type trajectories. (b) Far-field intensity distribution, showing unidirectional emission. The index of refraction of the dielectric disk is $n = 3$. Adapted from Ref. (Baryshnikov *et al.*, 2004).

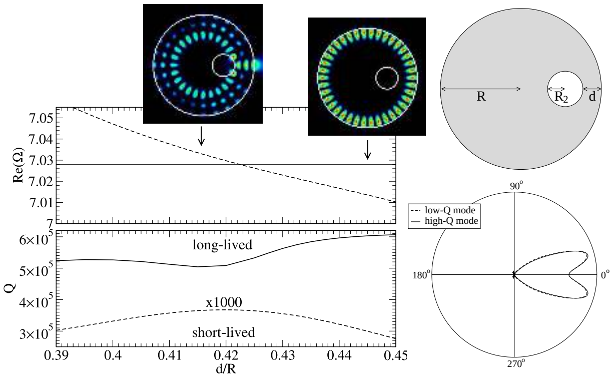

FIG. 33 (Color online) Normalized frequencies $\Omega = \omega R/c$ and quality factors vs. d for a high-Q WGM and a low-Q mode with directed emission in the annular cavity, a microdisk of radius R with an air hole of radius $R_2 = 0.22R$ located at the distance d to the disk's boundary. The index of refraction for TM polarization is $n = 3.3$. The coupling of the two modes leads to unidirectional emission in the far field (lower right).

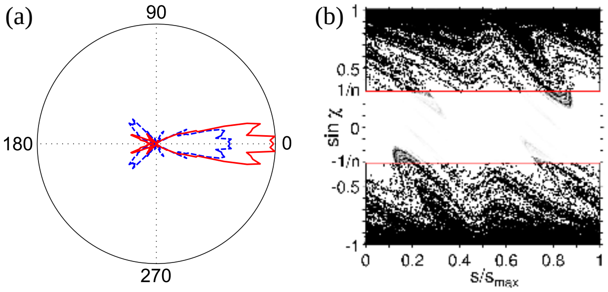

FIG. 34 (Color online) Ray simulations of unidirectional emission from a limaçon cavity with refractive index $n = 3.3$ and deformation parameter $\varepsilon = 0.43$. (a) Far-field intensity patterns are normalized so that the integrated intensity is unity. The solid (dashed) curve is for TE (TM) polarization. (b) Survival probability distribution for an ensemble of 50,000 rays starting uniformly in the phase space with identical intensity for TE polarization. The arclength s is normalized to the cavity's perimeter. The Fresnel weighted unstable manifold in the leaky region ($|\sin\chi| < 1/n$) are concentrated on very few high-intensity spots, giving highly directional output. (b) is from Wiersig and Hentschel (2008).

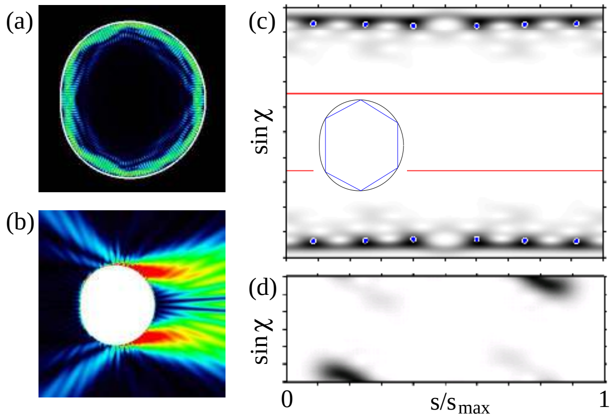

FIG. 35 (Color online) Calculated intensity distribution of an even-parity TE mode inside (a) and outside (b) a limaçon cavity with refractive index $n = 3.3$ and deformation parameter $\varepsilon = 0.43$. The mode has a normalized frequency $\Omega = \omega R/c = 26.0933$, and a Q factor of 185,000. The mode is confined spatially near the cavity boundary and emit predominantly to the direction $\varphi = 0$. (c) Husimi function of the TE mode in (a), exhibiting enhanced mode intensity around an unstable periodic ray trajectory illustrated in the inset. The dots mark the bouncing points of the periodic ray trajectory from the cavity boundary. The red horizontal lines $\sin\chi_c = 1/n$ enclosing the leaky region are indicated. (d) Magnified Husimi function in the leaky region agrees to the unstable manifold in Fig. 34(b), confirming its responsibility for the directional emission. Adapted from Wiersig and Hentschel (2008).

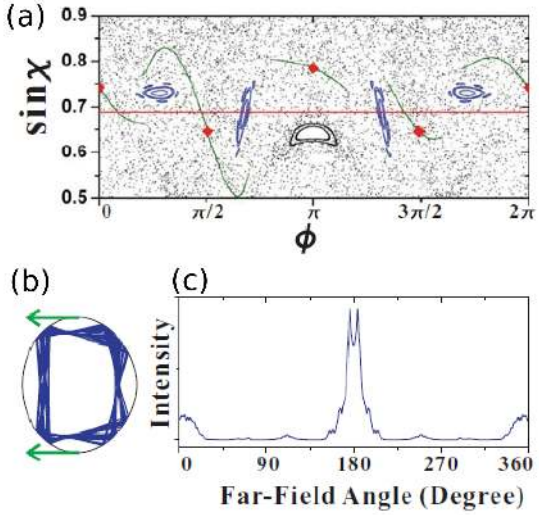

FIG. 36 (Color online) Ray dynamics in the face cavity made of silica. (a) shows the Poincaré SOS. The red diamonds mark the unstable period-4 orbit. Its unstable manifold is shaped by the islands around the stable periodic-4 orbit. The horizontal line is the critical line. Correspondingly, (b) shows the cavity boundary and a ray trajectory close to the stable periodic-4 orbit, while (c) is the far-field pattern obtained by ray simulations with modified Fresnel's law. Adapted from (Zou *et al.*, 2013).

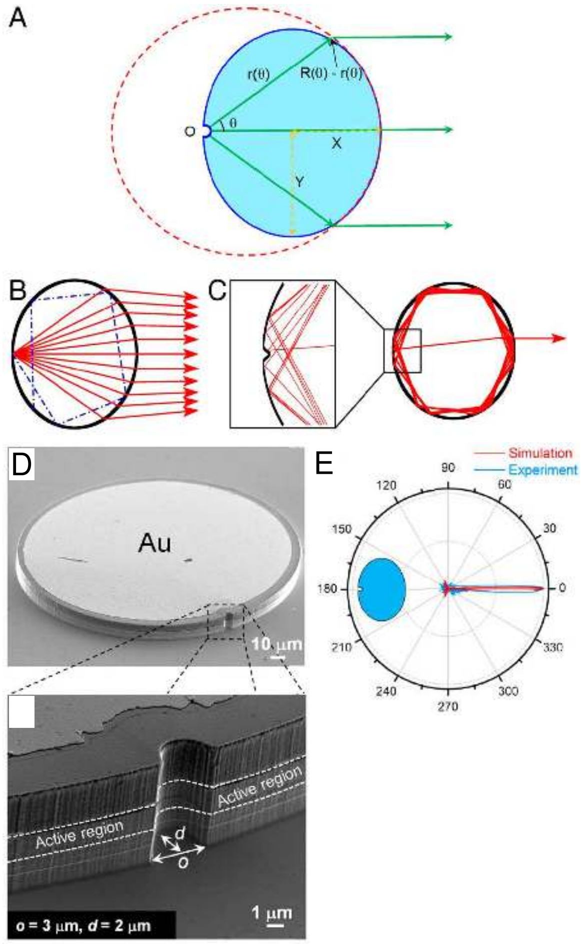

FIG. 37 (Color online) (A) Illustration of the notched-elliptical cavity. The arrows indicate that light is scattered by the notch and collimated as a parallel beam by the right-side boundary of the cavity. The boundary of the cavity (solid curve) is designed to best approximate that of the auxiliary ellipse (dashed curve) within the largest possible range. The notch is located at one of the foci of the auxiliary ellipse. The optimal long-to-short aspect ratio of the elliptical cavity is 1.2 for the refractive index of 3.2. (B) Ray simulation of the collimation effect: a number of rays are started at the position of the notch with different outgoing angles, simulating a scattering process. The solid rays leave the notch under relatively smaller outgoing angles, they hit the right boundary of the cavity and get refracted out. The dash-dotted ray leaves the notch at a high outgoing angle and is relaunched into a whispering-gallery mode. (C) A single ray is started at some position along the cavity boundary with an initial angle of incidence larger than the critical angle. It is then specularly reflected many times until at some point it hits the notch and gets reflected to the opposite boundary, refracted out, and leaves the cavity parallel to the horizontal axis due to the collimation effect. (D) Scanning electron microscope image of the notched-elliptical cavity. (E) Experimental (blue) and simulated (red) far-field intensity profiles. Adapted from (Wang *et al.*, 2010).

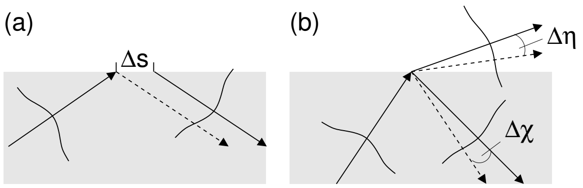

FIG. 38 Goos-Hänchen shift and Fresnel filtering at a dielectric interface. (a) Goos-Hänchen shift near/above the critical angle of incidence: the center of a beam (solid lines) with finite beam waist (curve) reflected at a dielectric interface is spatially shifted by Δs with respect to the geometric-optics prediction (dashed line). (b) Fresnel filtering near/below the critical angle of incidence: deviations from the law of reflection (angular shift $\Delta\chi$ of reflected beam) and Snell's law (angular shift $\Delta\eta$ of transmitted beam).

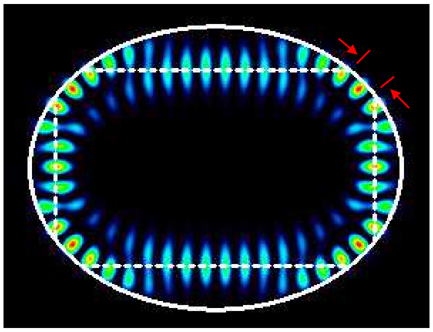

FIG. 39 (Color online) Calculated optical mode in a dielectric ellipse with refractive index $n = 3.3$. The mode pattern is localized along an optical beam (beam center is indicated by the dashed lines) including the spatial Goos-Hänchen shift (highlighted by the red bars); cf. the corresponding geometric-optics ray in Fig. 28(c).

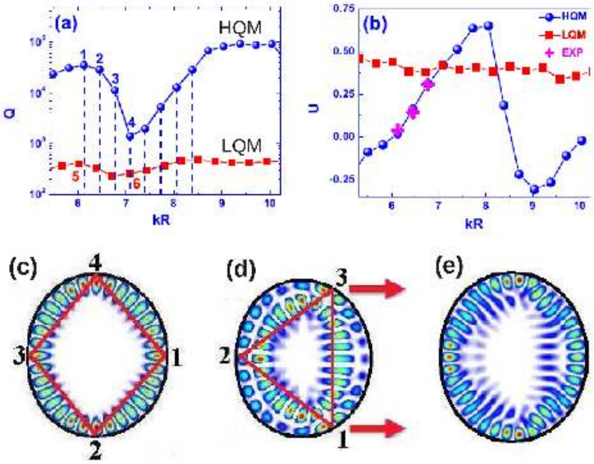

FIG. 40 (Color online) Numerical simulation of a wavelength-scale deformed dielectric cavity of refractive index $n = 3.13$. The cavity boundary is given by $r(\varphi) = R(1 + \varepsilon \cos\varphi)(1 - \varepsilon_1 \cos 2\varphi) + d$ in polar coordinates, where $R = 890\,\mathrm{nm}$, $\varepsilon = 0.28$, $\varepsilon_1 = 0.06$, and $d = 60\,\mathrm{nm}$. Calculated Q factor (a) and directionality U (b) versus kR for the high-Q modes (HQMs) (blue dots) and the low-Q modes (LQMs) (red squares). The coupling of the HQM and LQM at $kR \simeq 7$ leads to a drop of Q for the HQM and an increase of its U. (c-e) Calculated magnetic field intensity for the modes labeled 1, 5, 4 in (a), revealing mode 4 is a hybrid of 1 and 5. Adapted from (Song *et al.*, 2010).

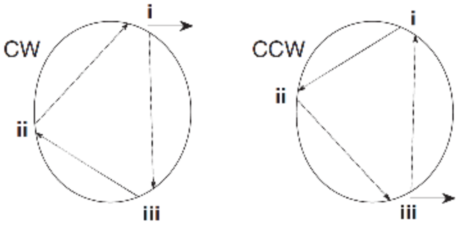

FIG. 41 Spatial separation of the period-3 orbit for clockwise (CW) and counter-clockwise (CCW) propagating rays in a wavelength-scale deformed cavity due to beam shifts. The cavity is the same as that in Fig. 40, and the orbit corresponds to the LQM. The three bounce points are labeled i, ii and iii. The arrow outside the cavity represents the direction of dominant emission from the bounce point where the angle of incidence is the smallest. Both CW and CCW rays emit in the same direction. From (Song *et al.*, 2011).

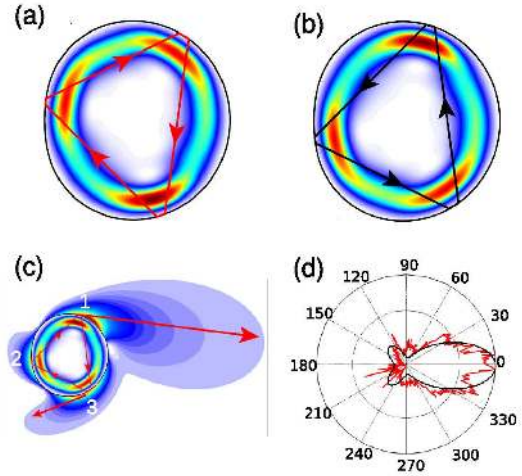

FIG. 42 (Color online) Calculated spatial intensity distribution of the CW (a) and CCW (b) waves that constitute a high-Q mode (HQM) at $kR = 3.2$ in a limaçon cavity. The intensity maxima for the CW and CCW waves are spatially separated. The solid lines depict the path for the CW beam in (a) and CCW beam in (b), reconstructed from the incident and emergent Husimi functions. The split in the CW and CCW orbits is due to beam shifts. (c) The CW wave intensity is enhanced outside the cavity to show that the emission is predominantly from the bounce 1. Similarly, the CCW wave (a mirror image with respect to the horizontal axis) emits from the bounce 3 into the same direction (not shown). (d) A polar plot of the experimentally measured far-field pattern of laser emission (thin red dotted line) which agrees well with the calculated output of the high-Q mode at the same wavelength (thick black solid line). From (Redding *et al.*, 2012b).

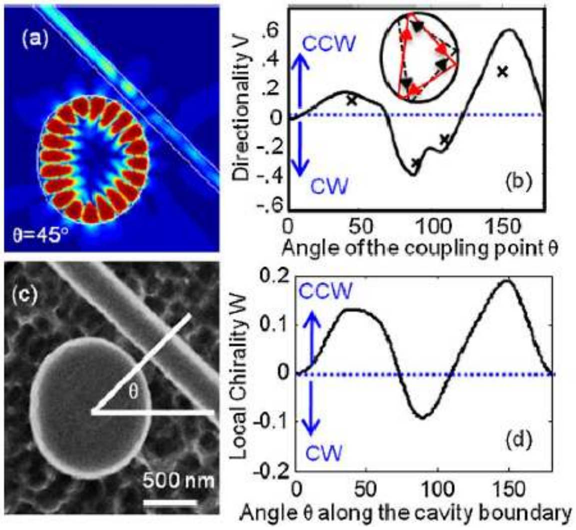

FIG. 43 (Color online) A wavelength-scale deformed microdisk coupled to a waveguide. (a) Calculated intensity distribution in a waveguide coupled deformed microdisk, showing directional coupling to a waveguide positioned at polar angle $\theta = 45°$. (b) Directionality of waveguide coupling V as a function of the coupling position θ on the cavity boundary. $V > 0$ ($V < 0$) corresponds to stronger coupling in the CCW (CW) direction. The crosses represent the experimental data points which agree well with the numerical simulation (solid line). The inset shows the orbits for the CW and CCW beams for this mode. (c) Top-view SEM image of a GaAs disk coupled to a waveguide. The disk is supported on an $Al_{0.7}Ga_{0.3}As$ pedestal at the center, and the GaAs waveguide is free standing in air and supported by two $Al_{0.7}Ga_{0.3}As$ pedestals at the ends. The background shows the residual $Al_{0.7}Ga_{0.3}As$ on the GaAs substrate after selective etching of the $Al_{0.7}Ga_{0.3}As$. (d) Local chirality $W(\theta)$ for the same mode in the absence of waveguide coupling. Locally, the CW and CCW intensities are not equal, leading to directional output to the waveguide shown in (b). Only half of the cavity boundary is plotted in (b,d), the other half can be obtained by mirror symmetry. From (Redding *et al.*, 2012b).

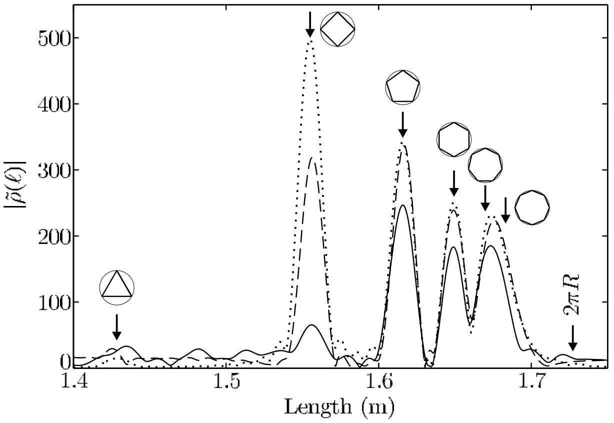

FIG. 44 Length spectrum of a circular microwave resonator. The solid (dashed, dotted) curve shows the measured (numerically calculated, semiclassical) spectrum. The arrows mark the lengths of the depicted periodic ray trajectories and of the circumference of the boundary. Except for the square-shaped ray trajectory a good agreement can be observed. From (Bittner *et al.*, 2010).

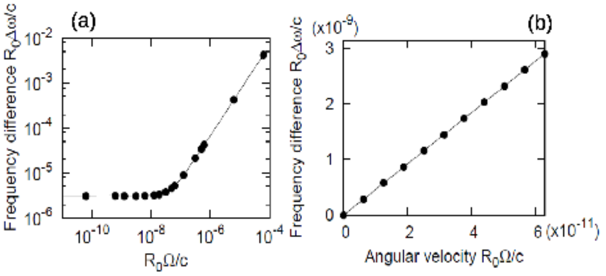

FIG. 45 Sagnac effect in deformed microcavities. The cavity boundary is closed, and the refractive index inside is equal to 1. The cavity modes under consideration are TM polarized. (a) A rotating quadrupole cavity (12) with $\varepsilon = 0.12$, and $R = R_0 = 6.2866$ μm. Calculated frequency difference $R\Delta\omega/c$ of a pair of quasi-degenerate modes at $nkR \simeq 49.338$ as a function of the (dimensionless) angular velocity $R\Omega/c$. The frequency difference does not change when the angular velocity is below the threshold $R\Omega_{th}/c \sim 5 \cdot 10^{-8}$; above the threshold the frequency difference increases linearly with the angular velocity. From (Sunada and Harayama, 2007). (b) A rotating microcavity of symmetry $C_{3\nu}$. The cavity boundary is defined by $r(\varphi) = R(1 + \varepsilon \cos 3\varphi)$, where $\varepsilon = 0.065$. Calculated frequency splitting $R\Delta\omega/c$ of a pair of degenerate modes at $nkR = 50.220$ vs. $R\Omega/c$. The frequency splitting increases linearly with the angular velocity with no threshold. Adapted from (Sunada and Harayama, 2007).

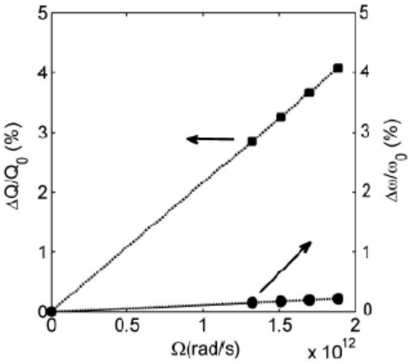

FIG. 46 Comparison of rotation-induced changes in frequency and Q factor of resonant modes in a circular microdisk. The disk radius is $R = 590$ nm and refractive index is $n = 3$. Calculated relative change in Q factor $\Delta Q/Q_0$ (squares) and the normalized frequency splitting $\Delta\omega/\omega_0$ (circles) of a pair of WGMs with $l = 1$ and $m = \pm 7$ as a function of the rotation speed Ω. The lines are linear fits. The slope for $\Delta Q/Q_0$ is 20 times higher than that for $\Delta\omega/\omega_0$, indicating the Q factor is 20 times more sensitive to rotation than the resonant frequency. From (Sarma *et al.*, 2012).

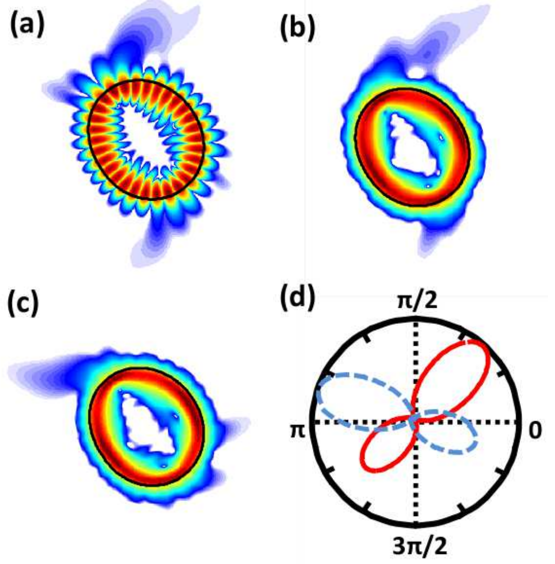

FIG. 47 (Color online) Numerical simulation of rotation-induced change in the far-field emission pattern of an asymmetric limaçon cavity. The cavity boundary is defined in the polar coordinates as $r(\varphi) = R[1 + \varepsilon_1 \cos(\varphi) + \varepsilon_2 \cos(2\varphi + \delta)]$, where $R = 591\,\mathrm{nm}$, $\varepsilon_1 = 0.1$, $\varepsilon_2 = 0.075$, and $\delta = 1.94$ radians. The refractive index inside the cavity is $n = 3.0$, and outside the cavity $n = 1.0$. Without rotation, a pair of quasi-degenerate modes at $\lambda = 598\,\mathrm{nm}$ consists mainly of CW traveling wave. Their near-field patterns are similar, one of them is shown in (a). The intensity outside the cavity is enhanced to illustrate the main emission direction. At the normalized rotation frequency $\Omega R/c = 0.001$, one of the two modes is converted to CCW traveling wave (c), the other remains CW wave (b). Their emission directions are very different. (d) Angular distribution of far-field emission intensity for the two modes in (b,c). The rotation causes a dramatic change in the far-field pattern of the mode in (b). From (Sarma *et al.*, 2014).